Dissertation

Roman Norz

The Loading Direction and its Effects on the Material Behaviour of Sheet Metals

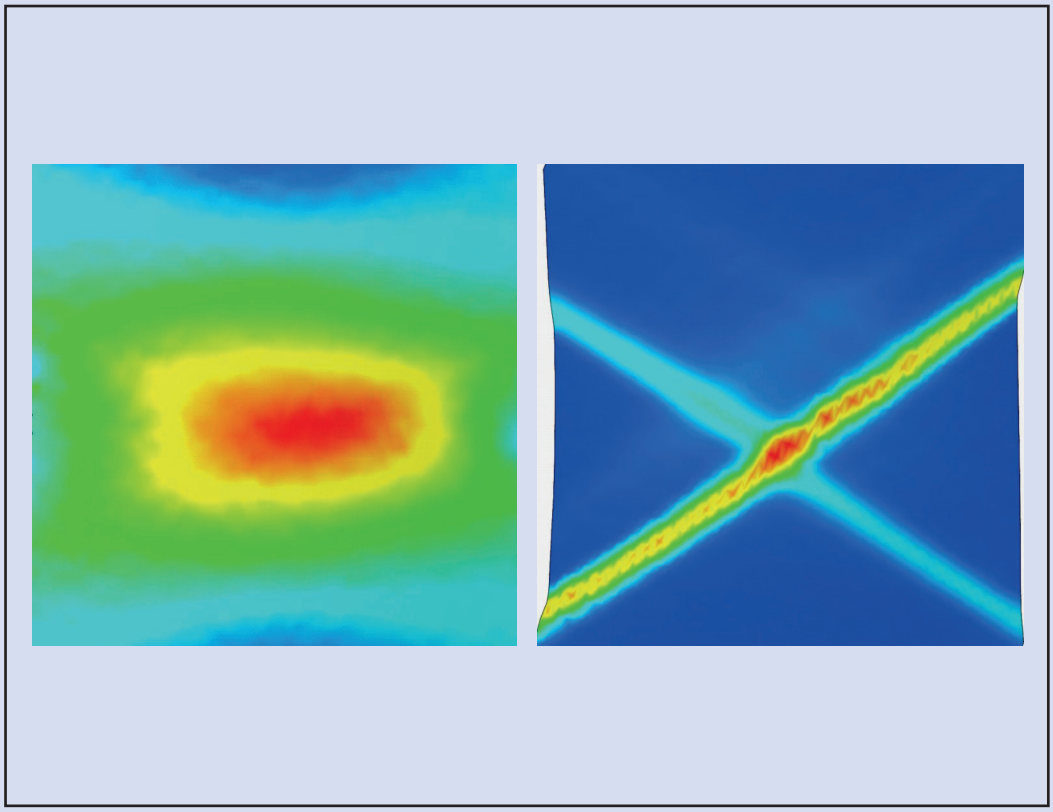

48
Maschinenbau

Lehrstuhl für
Umformtechnik
und Gießereiwesen

KOLLEMOSCH
Verlag & Kommunikation

Technische Universität München
TUM School of Engineering and Design

The Loading Direction and its Effects on the Material Behaviour of Sheet Metals

Roman Norz

Vollständiger Abdruck der von der TUM School of Engineering and Design der Technischen Universität München zur Erlangung eines Doktors der Ingenieurwissenschaften (Dr.-Ing.) genehmigten Dissertation.

Vorsitz:

Prof. Dr. techn. Jan Torgersen

Prüfende der Dissertation:

1. Prof. Dr.-Ing. Wolfram Volk
2. Assoc. Prof. Dr. Mats Sigvant
3. Prof. em. Dr. Pavel Hora

Die Dissertation wurde am 25.10.2023 bei der Technischen Universität München eingereicht und durch die TUM School of Engineering and Design am 02.04.2024 angenommen.

Die Deutsche Nationalbibliothek verzeichnet diese Publikation in der Deutschen Nationalbibliografie; detaillierte bibliografische Daten sind im Internet über https://portal.dnb.de abrufbar.

Impressum:

Herausgeber: Lehrstuhl für Umformtechnik und Gießereiwesen (utg), TUM School of Engineering and Design, Technische Universität München

Layout und Gestaltung: utg
Umschlaggestaltung: Broy New Media.
Umschlagabbildung: Roman Norz
Druck und Bindung: KS Druck, Ebersberg

Verlegerische Betreuung:
Kollemosch Verlag & Kommunikation
Lutz Prauser
Hauptstr. 39
85656 Buch am Buchrain

ISSN: 2364-6942
ISBN: 978-3-911206-03-7
www.tum.de

Danksagung

Die vorliegende Arbeit entstand während meiner Tätigkeit als wissenschaftlicher Mitarbeiter am Lehrstuhl für Umformtechnik und Gießereiwesen der Technischen Universität München.

Zahlreiche Personen haben am Entstehen dieser Arbeit einen Beitrag geleistet. Ohne Sie wäre diese Arbeit nicht möglich gewesen. Zunächst möchte ich meinem Doktorvater Herrn Prof. Dr.-Ing. Wolfram Volk, Ordinarius des Lehrstuhls für Umformtechnik und Gießereiwesen der Technischen Universität München, für Sein Vertrauen und Seine Unterstützung auch in schwierigen Zeiten danken.

Herrn Assoc. Prof. Dr. Mats Sigvant (Blekinge Tekniska Högskola) und Herrn Prof. Dr. Pavel Hora (ETH Zürich) danke ich für die Übernahme des Koreferats. Herrn Prof. Dr. techn. Jan Torgersen (Lehrstuhl für Werkstoffwissenschaften, TUM) möchte ich für die Übernahme des Prüfungsvorsitzes ebenfalls danken.

Ebenso gilt mein Dank allen Mitarbeiterinnen und Mitarbeitern des Lehrstuhls, die durch zahlreiche konstruktive Diskussionen und wertvolle Ratschläge wesentlich zum Gelingen dieser Arbeit beigetragen haben. Hierbei möchte ich mich besonders bei den Kolleginnen und Kollegen aus der Umformerrunde bedanken. Besonderer Dank gilt meinen Kollegen Dr.-Ing. Simon Vitzthum, Dr.-Ing. Matthias Eder, Dr.-Ing. Maximilian Gruber und Lorenz Maier für die zahlreichen Denkanstöße und Möglichkeiten bedanken. Weiter danke ich allen Studentinnen und Studenten für Ihren Beitrag zu dieser Arbeit. Darüber hinaus möchte ich mich bei meinen Bürokollegen, Alexander Kindsmüller, Lorenz Maier und Benedikt Kirchebner für die angenehme Atmosphäre und gemeinsame Zeit danken.

Zuletzt möchte ich mich bei meinen Eltern Karin und Christof sowie meinem Bruder Manuel herzlich danken. Ohne ihre fortwährende Unterstützung und Förderung hätte ich dieses Ziel nicht erreicht.

Roman Norz
Garching, Mai 2024

Kurzbeschreibung

Die Vorhersage des Versagens bei der Herstellung von umgeformten Blechbauteilen kann auch nach jahrzehntelanger Forschung immer noch ein Problem darstellen. Als klassische Methode zur Vorhersage der Herstellbarkeit hat sich das Grenzformänderungdiagramm (GFD) etabliert. Liegen die auftretenden Dehnungen eines Bauteils während des Umformprozessunterhalb der im GFD dargstellen Grenzformänderungskurve (GFK), so ist das Bauteil ohne Defekte herstellbar. Die verlässliche Vorhersage des Versagens beschränkt sich beim GFD jedoch auf lineare Dehnpfade. In der Realität treten jedoch in nahezu jedem Bauteil nicht-lineare Dehnpfade auf. Eine verlässliche Vorhersage der Herstellbarkeit ist somit mittels des GFD nicht mehr möglich.

In dieser Arbeit wird der Einfluss von nicht-linearen Dehnpfaden sowie einer Änderung der Belastungsrichtung auf drei Blechwerkstoffe untersucht. Zunächst wird anhand von bi-linearen Versuchen die Auswirkung nicht-linearer Dehnpfade und einer Belastungsrichtungsänderung auf die Umformbarkeit mittels Nakajimaversuchen bestimmt. Hierbei zeigt sich, dass die untersuchten Stahlwerkstoffe eine hohe Sensitivität bezüglich einer Änderung der Belastungsrichtung besitzen. Für die Aluminiumlegierung AA6016-T4 zeigt sich hingegen, dass die Umformbarkeit nahezu unbeeinflusst bleibt.

Durch die Anwendung von verschiedensten interdisziplinären Messmethoden, von der makroskopischen bis hin zur mikroskopischen Welt, wird die Ursache für die Resultate der Nakajimaversuche beschrieben. Die Ergebnisse der mechanischen, optischen Untersuchungen sowie in-situ Diffraktionsexperimente erlauben einen tiefen Einblick in die Materialien und tragen so wesentlich zu einem vertieften Verständnis der Wirkzusammenhänge bei.

Anhand der Ergebnisse dieser Arbeit wird der Einfluss des Materialgefüges auf die Sensitivität bezüglich nicht-linearer Dehnpfade mit einer Änderung der Belastungsrichtung gezeigt. Die Komplexität der Ursachen für den Einfluss führen dazu, dass zahlreiche Versagensmodelle nicht mehr anwendbar sind. Um das Versagen bei solch komplexen Dehnpfaden dennoch vorhersagen zu können, wird ein phänomenologischer Ansatz, basierend auf dem Generalized Forming Limit Concept (GFLC), entwickelt und anhand eines Realbauteiles validiert.

Abstract

Even after decades of research, predicting failure in the manufacture of deep-drawn sheet metal components can still be a problem. The forming limit diagram (FLD) has established itself as the classic method for predicting manufacturability. If the occurring strains of a component during the forming process are below the forming limit curve (FLC) shown in the FLD, the component can be manufactured without defects. However, the reliable prediction of failure is limited to linear strain paths in the FLD. In reality, however, non-proportional strain paths occur in almost every component. Therefore, a reliable prediction of manufacturability is no longer possible using the FLD.

In this work, the influence of non-proportional strain paths as well as a change in the loading direction on three sheet metal materials is investigated. First, the effect of non-proportional strain paths and a change in loading direction on formability is determined by means of bi-linear tests using Nakajima tests. It is shown that the investigated steel materials have a high sensitivity with regard to a change in the loading direction. For the aluminium alloy AA6016-T4, on the other hand, it is shown that the formability remains almost unaffected.

By applying a wide range of interdisciplinary measuring methods, from the macroscopic to the microscopic world, the reason for the results of the Nakajima tests is described. The results of the mechanical and optical investigations as well as in-situ diffraction experiments, allow a deep insight into the materials and thus contribute significantly to a deeper understanding of the interactions.

Based on the results of this work, the influence of the material structure on the sensitivity to non-proportional strain paths with a change in loading direction is shown. The complexity of the causes for the influence lead to the fact that numerous failure models are no longer applicable. In order to still be able to predict failure in such complex strain paths, a phenomenological approach based on the Generalised Forming Limit Concept (GFLC) is developed and validated using an actual component.

Contents

Nomenclature

Symbol	Unit	Meaning
a	Å	Lattice constant
b	Å	Burgers vector
d_{hkl}	Å	Atomic spacing for the (hkl) lattice plane
d^0_{hkl}	Å	Atomic spacing for the (hkl) lattice plane in the initial state
e	-	Microstrain
h_c	nm	Indentation depth for Nanoindentation
k_f	MPa	True stress
l	mm	Current length
l_0	mm	Initial length
l_{FLC}	-	Load path length of the linear FLC
l_{inc}	-	Load path length of current increment
n	-	Multiple of wavelength
A	-	Fracture elongation
A_c	mm_2	Contact area for Nanoindentation
A_g	-	Uniform elongation
D	nm	Crystallite size
E	GPa	Young's modulus
F	N	Force
G	-	Gauss function
H	GPa	Nanohardness
I	-	Intensity
I_{BG}	-	Background intensity
I_{max}	-	Maximum intensity
K	-	Constant for Williamson-Smallman model
L	-	Lorentz function
P	N	Pressure load for Nanoindentation
R	mm	Punchradius for Nanoindentation
R_{eH}	MPa	Upper yield strength
R_m	MPa	Tensile strength
$YS_{0.2\%}$	MPa	Yield strength at 0.2 % plastic strain

YS_{Tmin}	MPa	Yield strength at temperature minimum
YS_0	MPa	Yield strength at zero plastic strain
β	-	Strain ratio
β_{corr}	-	Corrected integral breadth
β_{exp}	-	Experimentally observed integral breadth
β_{ins}	-	Instrumental integral breadth
β_{size}	-	Integral breadth caused by grain size effects
β_{strain}	-	Integral breadth caused by microstrains
β_{pre}	-	Pre-strain ratio
β_{post}	-	Post-strain ratio
ε	-	True strain
ε_e	-	Engineering strain
ε_{eff}	-	Effective pre-strain
ε_{hkl}	-	Lattice strain for the (hkl) lattice plane
$\langle \epsilon^2 \rangle$	-	Microstrain for Williamson-Smallman model
ε_1	-	Major strain
ε_2	-	Minor strain
Θ	°	Bragg angle
λ	nm	Wavelength
λ_{GFLC}	-	Load path length ratio
λ_{pre}	-	Pre-strain load path length ratio
λ_{post}	-	Post-strain load path length ratio
σ_e	MPa	Engineering stress

Abbreviations

Abbreviation	**Meaning**
AA	Aluminium alloy
Al	Aluminium
bcc	Body centered cubic
BG	Background
CHSP	Cold-rolled high strength
DESY	Deutsches Elektronen-Synchrotron
DIC	Digital image correlation
DIN	Deutsches Institut für Normung
DP	Dual-phase
EBSD	Electron backscatter diffraction
eMMFC	Enhanced modified maximum force criterion
fcc	Face centered cubic
FWHM	Full width at half maximum
FE	Finite element
FLC	Forming limit curve
FLD	Forming limit diagramm
FLSC	Stress-based forming limit diagramm
GFD	Grenzformänderungsdiagramm
GFK	Grenzformänderungskurve
GFLC	Generalized forming limit curve
GISSMO	Generalized incremental stress state dependent damage model
GND	Geometrically necessary dislocation
HAH	Homogeneous anisotropic hardening
hdp	Hexagonal close packed
HY-steel	High yield steel
IB	Integral breadth
IF	Initial forming direction
IF-steel	Interstitial free steel
LaB_6	Lanthanum hexaboride
MMFC	Modified maximum force criterion
MnS	Manganese sulfide

ND	Normal direction
ODF	Orientation distribution function
PF	Post forming direction
PEPS	Polar effective plastic strain
PT	Platinum resistance thermometer
RD	Rolling direction
SEM	Scanning electron microscope
SSD	Statistically stored dislocation
TD	Transverse direction
TDEM	Time dependent evaluation method
TEM	Transmission electron microscope
TUM	Technical University of Munich
utg	Chair of Metal Forming and Casting
WH	Williamson-Hall
XRD	X-Ray diffraction

Supplementary Information

Prior publications

Some of the results presented in this thesis have been published in scientific journals and conference proceedings. These are registered according to the valid doctoral regulations and are not referenced again separately in this thesis. The publications addressed are listed below.

VOLK, W., R. NORZ, M. EDER and H. HOFFMANN (2020). "Influence of non-proportional load paths and change in loading direction on the failure mode of sheet metals". In: *CIRP Annals - Manufacturing Technology* Vol. 69.

NORZ, R., F. R. VALENCIA, S. GERKE, M. BRÜNIG and W. VOLK (2022). "Experiments on forming behaviour of the aluminium alloy AA6016". In: *IOP Conference Series: Materials Science and Engineering* Vol. 1238.

NORZ, R., N. MANOPULO, M. SIGVANT, A. R. CHEZAN and W. VOLK (2022). "Prediction of Necking Initiation in Case of Abrupt Changes in the Loading Direction". In: *NUMISHEET 2022. The Minerals, Metals & Materials Series* pp. 617-625.

NORZ, R. and W. VOLK (2022). "Influence of Loading Direction on the Mechanical Parameters of Pre-formed Materials in Tensile Test". In: *NUMISHEET 2022. The Minerals, Metals & Materials Series* pp. 899-908.

NORZ, R., S. VITZTHUM and W. VOLK (2022). "Failure behaviour of various pre-formed steel sheets with respect to the mechanical grain boundary properties". In: *International Journal of Material Forming* Vol. 15.

NORZ, R., F. R. VALENCIA, S. VITZTHUM, B. UNGUREANU, S. GERKE, M. BRÜNIG and W. VOLK (2023). "Investigation of the influence of loading direction after pre-forming on the formability and mechanical properties of DP600". In: *Materials Research Proceedings* Vol. 28., pp. 747-754.

Note on Citations

If the reference is in the sentence or before the period at the end of the sentence, it refers directly to a word, a group of words, or the statement of that sentence. If the reference is placed at the end of a paragraph after the period, it refers to the content of the complete preceding paragraph.

1 Introduction

Forming technology enables the economical production of components in high volumes. In addition to cost-effectiveness, the ability to produce complex components is essential in many industries. The increasing complexity of components is forcing companies to take advantage of finite element simulation (FE simulation). Modern simulation programmes are able to model even complex manufacturing processes, thereby indicating production feasibility. However, any simulation is only as good as the data and models provided by the user.

There are a number of standardised tests that can be used to determine material properties, such as the tensile test, the hydraulic bulge test, or the Nakajima test. These standardised tests allow the material parameters to be determined, which can be used to calibrate various models to describe the material behaviour. Depending on the complexity of the models, more or fewer tests are required. It is up to the user to decide which model is most appropriate for the task (Volk et al., 2019).

A simple graphical prediction of the manufacturability of deep-drawn parts in FE simulations is provided by the Forming Limit Curve (FLC) introduced by Keeler (1966). The part can be formed if the strains of all elements are below the FLC. If the strains are above the FLC, failure will occur due to localised necking. The ease of evaluation makes this failure criterion one of the most widely used in sheet metal forming. However, the limitation of this method to purely linear and continuous load paths means that it has limited applicability to complex sheet metal components where non-proportional load paths occur. Such non-proportional load paths are known to have a significant effect on the formability of various sheet materials. The non-proportionality of a load path can lead to an increase or decrease in formability depending on the pre-forming condition. Therefore, all elements with an individual load path require their own forming limit strains.

In addition to the deformation history, the loading direction also influences the formability of different materials, even for the initial material. This effect is evident when testing dual-phase steels (Mackensen, 2014). To account for this effect, DIN ISO 12004-2 proposes a parallel groove at 90° to the initial rolling direction (RD) for steels and 0° to the initial RD for aluminium, as these directions are known to have the lowest formability (DIN EN ISO 12004-2, 2021). The combination of the two factors, non-proportional load paths and loading direction, in terms of formability and mechanical properties, still needs to be sufficiently investigated.

This work aims to determine the influence of the loading direction of pre-formed materials on formability and mechanical parameters such as yield strength. In addition to quantifying the influence, different methods are used to assess the causes of these dependencies. The methods used range from macroscopic to microscopic investigations and are intended to provide a basic understanding of the material behaviour that occurs. A phenomenological approach based on the Generalised Forming Limit Concept (GFLC) introduced by Volk et al. (2012) is extended to predict the failure of non-proportional load paths with a change in the loading direction. For this purpose, an experimental database is built. This database serves as a basis for the methodology. The proposed model will be a tool for a more accurate prediction of the manufacturability of complex sheet metal components.

2 Fundamentals and State of the Art

In order to explain the experimental investigations carried out in this thesis in more detail, this chapter deals with the necessary basics. Firstly, the macroscopic experiments for the characterisation of sheet materials are presented in more detail. The resolution is in the millimeter range. As these experiments are based on homogeneous material behaviour, further investigations are necessary to gain a better understanding of the material. Different methods such as nanoindentation or in-situ synchrotron diffraction are used for this purpose. These experiments can reveal effects at the microscopic level, i.e. in the micrometer range. To bring these two worlds together, the microstructure of metals is also discussed.

2.1 Fundamentals of Plasticity

2.1.1 Strains

If a material is subjected to an external load, this will lead to a change in shape if the load is large enough. This change in the shape can be expressed as the engineering strain ε_e, which is the quotient of the change in length Δl and the initial length l_0 and is calculated as follows:

$$\varepsilon_e = \frac{l_1 - l_0}{l_0} = \frac{\Delta l}{l_0} \quad . \tag{2.1}$$

A representation more widely used in forming technology is the true strain ε. In contrast to engineering strain, true strain refers to the current length. The calculation of the true strain ε follows

$$\varepsilon = \int_{l_0}^{l_1} \frac{dl}{l} = ln\frac{l_1}{l_0} = ln(1 + \varepsilon_e) \quad , \tag{2.2}$$

with l being the current length. A significant advantage of the representation in true strains is the possibility to add the strains occurring in successive forming processes. The representation of the true strains can be done by means of a tensor for three-dimensional deformations:

$$\boldsymbol{\varepsilon} = \begin{pmatrix} \varepsilon_{11} & \varepsilon_{12} & \varepsilon_{13} \\ \varepsilon_{12} & \varepsilon_{22} & \varepsilon_{23} \\ \varepsilon_{13} & \varepsilon_{23} & \varepsilon_{33} \end{pmatrix} \quad . \tag{2.3}$$

For a plane stress condition such as occurs in sheet metal forming (Marciniak et al., 2002, p.16), the tensor can be transformed into a principal strain space (Eder, 2023). This results in

$$\boldsymbol{\varepsilon} = \begin{pmatrix} \varepsilon_1 & 0 & 0 \\ 0 & \varepsilon_2 & 0 \\ 0 & 0 & \varepsilon_3 \end{pmatrix} \quad . \tag{2.4}$$

The mentioned strains ε consist of an elastic ε_{el} and a plastic ε_{pl} part:

$$\varepsilon = \varepsilon_{el} + \varepsilon_{pl} \quad . \tag{2.5}$$

During deformation, the volume of the material remains constant in the plastic regime. In the elastic regime strains lead to a change in the volume of the material. In forming technology, the plastic portion is much larger than the elastic portion (Traphöner, 2020). Therefore, the elastic portion can be neglected and the volume constancy for true strains applies:

$$tr(\boldsymbol{\varepsilon}) = \varepsilon_1 + \varepsilon_2 + \varepsilon_3 = 0 \quad . \tag{2.6}$$

2.1.2 Stresses

The deformation of a body requires a certain force. Due to these forces, stresses become effective inside the body (Hoffmann et al., 2012). These stresses are related to the initial cross-section of the body in the case of engineering stress,

$$\sigma_e = \frac{F}{A_0} \quad , \tag{2.7}$$

where F is the current applied force and A_0 is the initial cross section of the specimen. In contrast, the true stress is related to the current cross section of the body. The calculation of the true stress σ, also called the instantaneous stress or yield stress, is carried out according to,

$$\sigma = \frac{F}{A} \quad , \tag{2.8}$$

where F is the current force and A is the current cross section of the specimen. (Doege and Behrens, 2018, p. 15-17)

Since forces do not only act in one direction, the three-dimensional stresses are represented in a stress tensor:

$$\boldsymbol{\sigma} = \begin{pmatrix} \sigma_{11} & \sigma_{12} & \sigma_{13} \\ \sigma_{12} & \sigma_{22} & \sigma_{23} \\ \sigma_{13} & \sigma_{23} & \sigma_{33} \end{pmatrix} \quad . \tag{2.9}$$

With respect to the stresses, assuming a plane stress state as occurs in sheet metal forming, in combination with a principal axis transformation, the stress tensor can be given the following form, according to Eder (2023):

$$\boldsymbol{\sigma} = \begin{pmatrix} \sigma_1 & 0 & 0 \\ 0 & \sigma_2 & 0 \\ 0 & 0 & 0 \end{pmatrix} \quad . \tag{2.10}$$

2.2 Macroscopic Material Characterisation in Sheet Metal Forming

Material characterisation is the basis of all material models. Various tests can be used to determine the behaviour of a material under certain stress conditions. However, these tests can only cover a few specific stress states. In order to make the characteristic values from the tests usable for any arbitrary stress state, different models are used (Rösler, 2012, p. 82). These models must correctly represent the material behaviour, especially in the plastic range. To do this, the model must be able to describe the onset of yielding, the strain hardening, the resulting deformation and the change in material properties after the deformation has occurred (Birkert et al., 2013, p. 123). Thus, material characterisation plays a fundamental role in FE simulations of sheet metal forming components. Otherwise wrong conclusions might be drawn from the obtained simulation results.

2.2.1 Uniaxial Tensile Test

According to DIN EN ISO 6892-1 (2020), the tensile test is the most commonly used test for determining the stress-strain or yield curve of sheet materials. Due to the simplicity of the test procedure and evaluation, and the large number of material parameters obtained, it can be used to calibrate simple material models. However, the parameters obtained are limited to low strains as there is no longer a homogeneous uniaxial stress state after the onset of necking.

In the tensile test, a standardised flat tensile specimen is deformed at a constant strain rate until it fails. A load cell measures the force required to deform the specimen. The longitudinal deformation of the specimen is measured by a strain gauge. This strain gauge can be tactile or optical. From this a force-deformation curve can be determined. This curve is used to compute the stress-strain curve. The engineering strain is calculated by equation 2.1, while the engineering stress is caluclated by equation 2.7.

The use of the engineering stress-strain curve is useful in the elastic region, where there is a reversible change in shape. This means that after the load has been removed from the specimen, the cross-section of the specimen again corresponds to the initial cross-section. In contrast, the plastic regime is characterised by an irreversible change in shape. The cross section of the specimen is reduced compared to the initial cross section even after the specimen is unloaded. To account for this effect, the stress and strain are related to the current cross-section and length in sheet metal forming, according to equation 2.2 and equation 2.8. An example of a engineering stress-strain curve and a flow curve and the most important characteristic parameters obtained from the tensile test are shown in Figure 2.1.

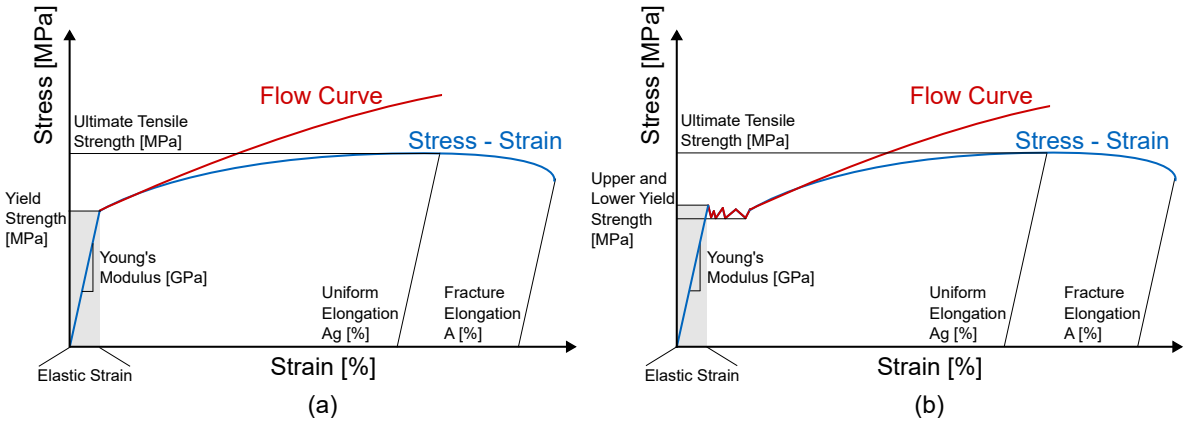

Figure 2.1: Stress - strain curve and flow curve for a material without (a) and with (b) a pronounced yield strength.

The Young's modulus E determines the slope of the stress-strain curve at the beginning of the test. At the end of the elastic range, the material begins to deform plastically, therefore permanently. The transition from elastic to plastic is difficult to determine for most materials. Therefore in most cases the 0.2 % plastic yield strength is used. The straight elastic line is shifted by 0.2 % plastic strain and the intersection with the stress-strain curve corresponds to the yield strength $Y_{S0.2\%}$, see Figure 2.2 (a). For materials with a pronounced yield strenght, see Figure 2.1 (b), the transition is clearly visible. The stress at which plastic deformation begins for such materials is called the upper yield strength R_{eH}. The flow curve begins after the onset of plastic deformation, at the end of the linear elastic region where the stress is proportional to the strain, and continues up to the uniform elongation.

After the onset of the plastic regime a strengthening of the material takes place. When the maximum force is reached, diffuse necking begins. Diffuse necking begins when the material can no longer compensate for the reduction in cross section due to deformation by material hardening and the criterium of Considère (1885),

$$\frac{d\sigma}{d\varepsilon} = \sigma \quad , \tag{2.11}$$

is fulfilled. The strain reached at the onset of necking is called the uniform strain A_g and the prevailing stress is called the tensile strength R_m. Up to this point the material is in a homogeneous uniaxial stress state. With the onset of necking, a multiaxial stress state occurs in the necking zone (Banabic et al., 2000, p. 64). The material now requires less force to be deformed and eventually fails. The strain at the time of failure is called the fracture elongation.

Determination of the Onset of Yielding

Determining the physical onset of yielding is challenging for most materials. Since the yield strength is currently determined without a physical background and there are even two different methods standardised in the DIN EN ISO 6892-1 (2020), new methods have been developed to determine the yield strength more precisely. Sallat (1988) investigated different methods to determine the onset of yielding. The use of an infrared camera led to promising results. Due to the thermoelastic effect, the sample cools in the elastic regime. With the onset of plastic deformation, the sample heats up since most of the work input is converted into heat. This procedure has been adopted by Müller (1996, p. 120-121) for AlMgSi1. The onset of flow is determined using the temperature minimum and is further represented as YS_{Tmin}. The combination of the temperature based determination methods with a cruciform tensile test allows

the onset of yielding to be determined for different stress states. For AA5182-O, Banabic and Huetink (2006) were able to show that the yield stresses obtained by the temperature method are lower than those obtained by the classical $YS_{0.2\%}$ method. The use of an infrared camera to measure temperature leads to problems if the ambient temperature is not constant during the experiment. To overcome this problem, Vitzthum et al. (2019) developed a clip-on device that positions the temperature sensor directly on the surface of the specimen. At the time of the temperature minimum, plastic work has already taken place to compensate for the cooling of the specimen. Therefore, the temperature minimum does not describe the physical onset of yielding of the material. Using a new methodology, the onset of yielding was defined at the time of deviation of the temperature signal from the linear temperature decrease and is denoted as YS_0, see Vitzthum et al. (2022a). By determining the yield stress based on the measurable variable of temperature, the two temperature-based methods are physically based in contrast to the $YS_{0.2\%}$-method. The $YS_{0.2\%}$-method (a) and the two temperature-based methods (b) are depicted in Figure 2.2.

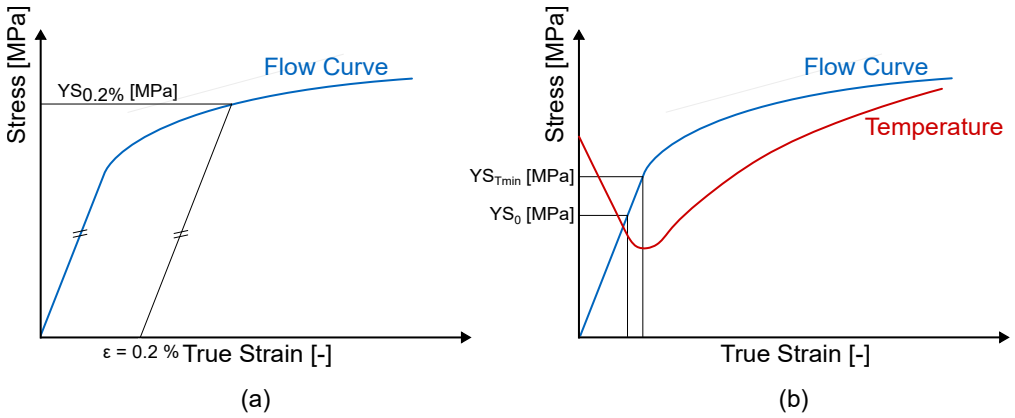

Figure 2.2: Determination of the onset of yielding by the standardised $YS_{0.2\%}$ - method (a) and the temperature-based methods (b).

To verify this thesis, Vitzthum et al. (2022a) conducted in-situ synchrotron diffraction tensile test experiments. Based on these experiments, it could be shown that the developed methodology and the resulting yield strenght YS_0 depicts the physical onset of yielding much more accurately than the temperature minimum method YS_{Tmin} or the $YS_{0.2\%}$ - method according to DIN EN ISO 6892-1 (2020) for a HC260Y steel as well as an DP1000 steel. Even for cyclic experiment and tension-compression experiments the results obtained by the temperature based methology lead to more accurate results compared to the other methods (Vitzthum, 2023, p.111-117).

2.2.2 Determination of the Formability of Sheet Metals

In addition to strength, the degree of deformation that can be achieved with the material prior to failure also plays a role in materials processed by forming. To represent the formability of different materials simply and understandably in the simulation, the FLC was introduced.

Forming Limit Curve

The FLC was first created by Keeler (1961) for the right side, hence positive major and minor strain changes, while the left side of the FLC was studied in more detail by Goodwin (1968). The minor strain is negative in these stress states, and hence there is a reduction in the width of the specimen. The major and minor strain changes in the material due to plastic deformation are plotted in a diagram to determine the FLC. The strains reached at the onset of local necking result in the FLC. Areas below the FLC mean that a component can be finished without local necking, represented by the green area in Figure 2.3. Strains above the FLC result in local necking of the specimen (red area in Figure 2.3) and failure. After localised necking, the material is not fractured yet but any further deformation will only take place in the area where localised necking occured. The fracture curve is, therefore, above the FLC. The difference between the FLC and the fracture curve is dependent on the material. For some brittle materials the FLC and the fracture curve can intersect, meaning that no localised necking takes place prior to fracture. Strains were measured using circles etched into the specimen. The strains were determined from the deformation of the circles and their distance from each other. It was already evident that the size of the circles and the distance in between the circles had an effect on the achieved strains. Keeler (1966) found that the smaller the grid spacing, the higher the strains measured.

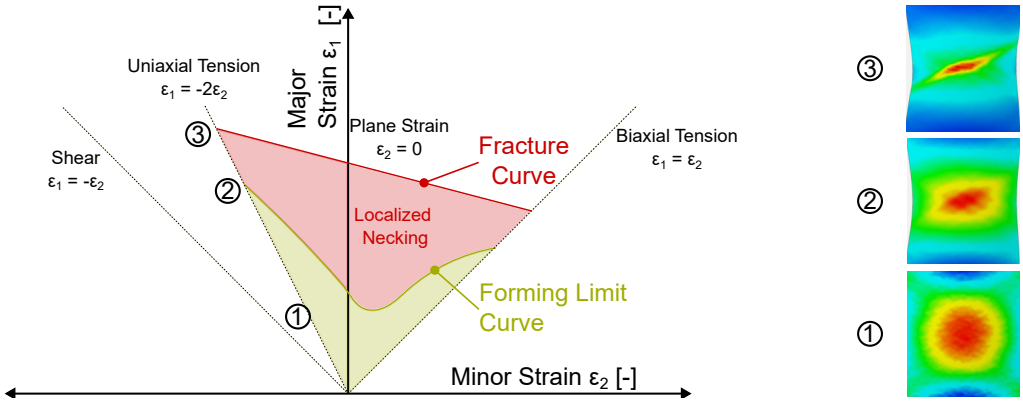

Figure 2.3: Schematic representation of a FLC with characterisitc areas and their corresponding strain distribution for the uniaxial case, the green area represents the safe area without necking while the red area represents necking.

Determination of the Forming Limit Curve

Several tests have been developed to determine FLC. Currently, the most commonly used methods are the Nakajima test according to Nakajima et al. (1968) and the Marciniak test according to Marciniak and Kuczyński (1967). These two tests are standardised procedures in the DIN EN ISO 12004-2 (2021). The two tests differ in the geometry of the punch and the specimens. The Nakajima test uses a round punch (Figure 2.4 (a)), whereas the Marciniak test uses a cylindrical punch with a radius at the top and an additional carrier blank between the punch and the specimen (Figure 2.4 (b)). The carrier blank has a hole in the middle. Due to the hole, no contact occurs between the punch and the evaluation area. This reduces the influence of friction on the result. Nevertheless, friction can occur at the outer radius of the punch. Different specimen geometries are used to adjust the different strain ratios. These differ in the width of the specimen bridge. As friction can occur between the punch and the sheet metal in both tests, care must be taken to ensure sufficient lubrication to achieve a friction-free test procedure. This is necessary because friction can influence the achievable strains. Likewise, the location of the crack is influenced. According to the standard, the crack must occur at the pole of the specimen.

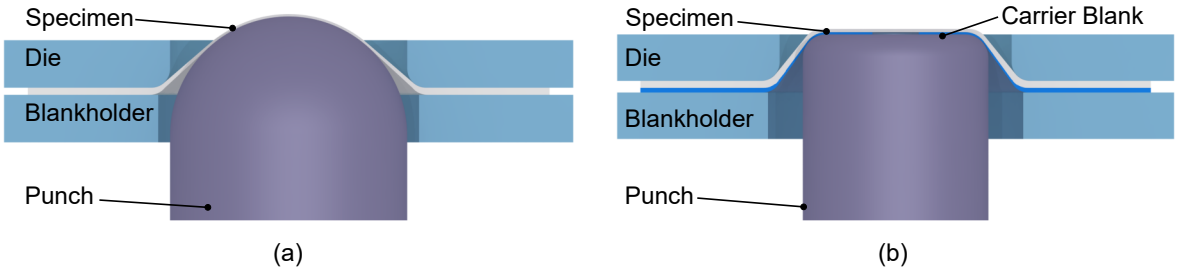

Figure 2.4: Schematic representation of the experimental Nakajima setup (a) and the experimental Marciniak setup (b).

Next to these standardised methods, numerous other tests can be used to determine the FLC. Banabic et al. (2013) developed a method in which a carrier blank and the test blank are deformed by hydraulic pressure until failure. The use of holes of different sizes makes it possible to adjust the stress state in the test area of the blank. This method is designed to overcome the friction problems of the Nakajima and Marciniak tests.

In addition to the methods already mentioned, cruciform specimens have also been used to determine the FLC. These allow the entire FLC to be recorded with a single specimen geometry. The desired stress states are set by clamping forces, see Jocham et al. (2017) or tensile forces in the specimen arms, see Leotoing et al. (2013). Both methods require an area of reduced

thickness in the center of the specimen to ensure failure in the pole. Norz and Volk (2019) circumvented this problem by using welded cruciform specimens. Here a specimen consists of three individual blanks welded together. The upper and lower blanks each have a recess in the center of the specimen to ensure that failure occurs in the pole. However, cruciform specimens are more costly than Nakajima or Marciniak specimens.

In all of the experimental setups presented for determining the FLC, measuring the strains that occur is necessary. The development of Digital Image Correlation (DIC) has greatly improved the accuracy. By continuously recording the strain throughout the experiment, the onset of local necking can be more accurately determined. To achieve a sufficient resolution of the strain development, a frame rate of at least 10 Hz is suggested by the DIN EN ISO 12004-2 (2021).

These information about the strains can be used to determine the onset of localised necking. To do so, various methods have also been published. The DIN EN ISO 12004-2 (2021) only lists the cross-section method. Three cross-sections are taken at the time of the last image before the crack occurs. The major and minor strains are determined along these sections. A parabola is then fitted to these sections. The highest point of the two parabolas gives the point in the FLC. Figure 2.5 shows a determination process for a single section. The strain development during the deformation of the specimen is not taken into account.

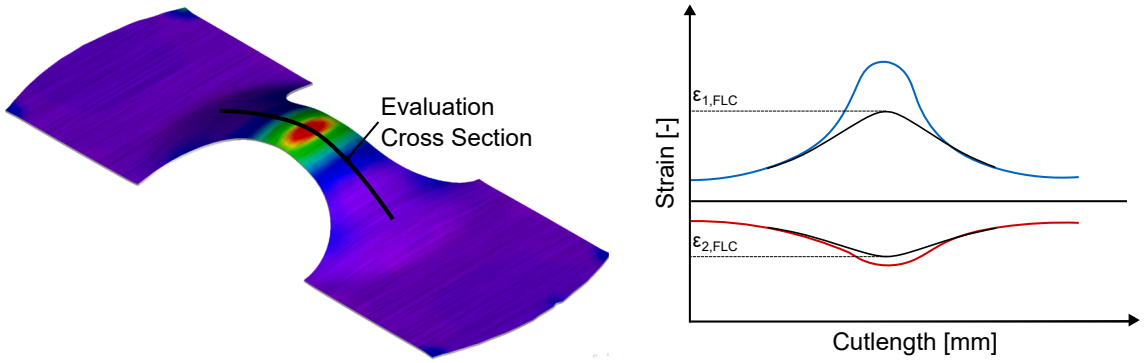

Figure 2.5: Exemplary determination of the major- and minor strain at the onset of necking using the cross section method.

This method is useful for materials that have a single necking zone, therefore only one area witch shows localisation (Merklein et al., 2010a). Materials with multiple necking zones cannot be evaluated using this method. Multiple necking zones can, for example, occur in dual-phase steels or aluminium alloys (Jocham, 2018, p. 100). Another aspect of this method is that it underestimates the formability of materials. Merklein et al. (2010b) showed for a selected part of a B-pillar made of SBZ800 steel that the formability obtained by the cross-section method is lower than the strains obtained during deep drawing of the part without any defects.

Multiple evaluation methods have been published to exploit the information available from DIC and overcome the problem of multiple necking zones and the underestimation of formability. Most of these methods plot and evaluate the evolution of the strain or the strain rate over time. The time-dependent evaluation methods include the evaluation methods according to Volk and Hora (2011), Merklein et al. (2010a), Hotz et al. (2013) and Sigvant et al. (2008).

The Time-Dependent Evaluation Method by Volk (TDEM) will be discussed in more detail here. In contrast to the cross-sectional method, which considers strain along a straight line, the evaluation area of the TDEM uses an area where the highest rate of thickness reduction $\dot{\varepsilon_3}$ occurs. The TDEM is based on the fact that an increase in strain rate in the thickness direction $\dot{\varepsilon_3}$ occurs at the onset of local necking. When looking at the strain rate history over the entire test period, two distinct areas become apparent. At first, the strain rate is almost constant or slightly increases. In the further course of the experiment, it increases rapidly just before failure. Two straight lines are fitted to these two distinct regions. The intersection of the two lines represents the onset of localised necking and is plotted on the FLC. The process is shown in Figure 2.6. In most cases, the TDEM leads to FLC which are above those obtained by the cross-section method.

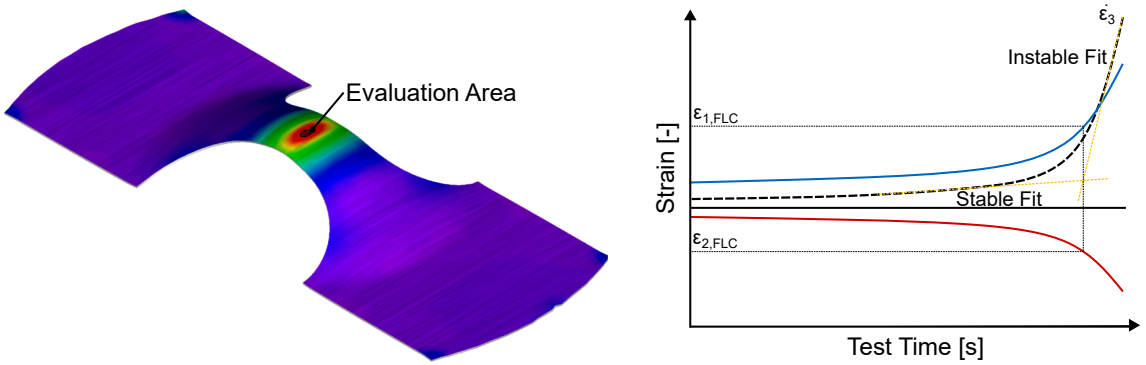

Figure 2.6: Exemplary determination of the major- and minor strain at the onset of necking using the TDEM.

The FLCs determined using the experimental set-ups and evaluation methods presented are influenced by numerous parameters. For example, an increase in thickness leads to an increase in FLC to a certain extent. Dilmec et al. (2013) has investigated this influence for AA2024-T4. Here, a thickness of 2 mm compared to a 0.8 mm material of the same material leads to an increase in the limit strains. In addition to the material thickness, the material properties, the punch radius, the temperature, and the forming speed also play a role. Besides the parameters mentioned, several other factors also have an impact on the FLC (Banabic et al., 2013, p.165-175).

2.3 Microscopic Material Characterisation in Sheet Metal Forming

2.3.1 Synchrotron Diffraction Experiments

Methods such as synchrotron diffraction are suitable to investigate microstructural processes during the tensile test in more detail. Synchrotron diffraction allows the continuous analysis of individual lattice planes and calculating dislocation densities during the tensile test. To better understand the measurement procedure of synchrotron diffraction, the structure of metallic materials will first be discussed in more detail.

Microstructure of Metals

Metallic materials consist of individual grains that form during the solidification of the melt. They are called crystallites because of their structure and are separated from each other by grain boundaries. Within a crystal, the individual atoms are arranged in a regular structure. This regular structure is called a crystal lattice. The arrangement of the atoms can be seen in the unit cell, see Figure 2.7. The three most important structures for metals are cubic body-centred (bcc), cubic face-centred (fcc) and hexagonal closest packing (hcp). These structures and their orientation with respect to the specimen's global coordinate system depend on the material manufacturing process. In general, for sheet materials, the rolling of the sheets creates a preferred orientation in the material. For illustration purposes, only the center of the atoms is shown. In a real structure, the atoms are in contact with each other. (Banabic et al., 2000, p. 5-7)

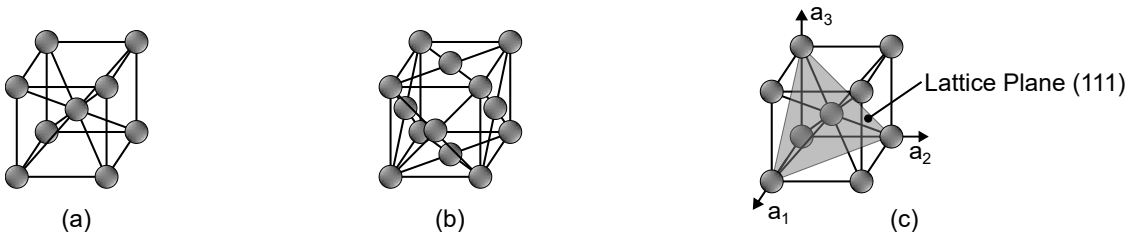

Figure 2.7: Schematic atom arrangement for the body-centered cubic (a), the face-centered cubic (b) material and the (111) lattice place for the bcc structure (c).

The planes and directions within a crystal structure are defined by the Miller indices *hkl* according to Miller (1839). Based on an initial coordinate system, a direction or plane is described as the intersection with the corresponding axis, see Figure 2.7 (c). The values of h, k and l must be integers. The different brackets indicate wheater a specific lattice plane is addressed, e.g. (111).

All symmetrically equivalent planes are addressed by using { } - brackets, while ⟨ ⟩ - brackets are used to describe symmetrically equivalent directions. (Spieß et al., 2019, p. 46-48)

As mentioned before, the common appearance of metals is a polycrystalline microstructure with its individual grains. The size of the grains is influenced by the alloying elements or the heat treatment process, for example. The microstructure of such a polycrystalline material is shown in Figure 2.8, where (a) shows a fine-grain structure while (b) shows a coarse-grain structure. The different angles of the structures indicate the different crystal lattice orientations.

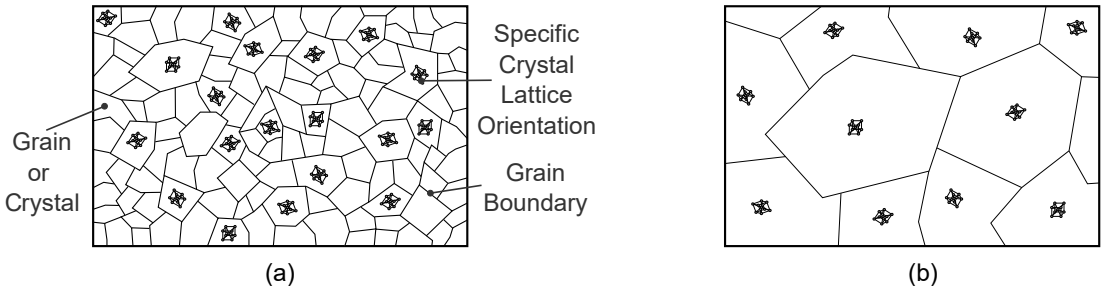

Figure 2.8: Schematic illustration of a polycrystalline material with a fine grain structure (a) and a coarse grain structure (b) according to Weißbach et al. (2015, p. 42).

Usually, metals have a microstructure in which the grains have a preferred orientation caused by the manufacturing process of the material, as most sheet metals undergo a rolling process to set the right sheet thickness. This means that the distribution of the crystallites is not random. The preferred orientation is referred to as texture. This texture can be caused by plastic deformation, the load path and the thermal treatment of the material. A strong texture, therefore, indicates that many grains have the same orientation, while a weak texture is a microstructure with more or less randomly distributed crystal orientations. (Morawiec, 2004, p. 135)

The texture can be determined by electron backscatter diffraction (EBSD) or X-ray diffraction (XRD). EBSD can be used to assess the orientation of single grains and small areas, while XRD determines the texture by a larger volume (Aydogan et al., 2016). An advantage of EBSD is that the results can be used as input for crystal plasticity simulation models, as they require information about the grain size and the crystal orientation of individual grains. It also requires a less complex experimental setup. On the downside, the sample preparation is time-consuming, as the surface to be investigated must be polished and etched. The most common representation of the texture, or orientation distribution function (ODF), is done by pole figures or Euler space sections with respect to a given sample coordinate system, see Figure 2.9 (b) and (c).

Although such pole figures are often used, they cause significant difficulties in the quantitative interpretation of textures caused by the superposition of the considered pole types, which leads

to high ambiguity. The ODF must be calculated and plotted in an Euler space section to obtain a less ambiguous description. (Hölscher et al., 1991)

The pole figure is a polar coordinate system, while the Euler space section is a cartesian coordinate system, but they both can be used to determine the texture. For sheet metals produced by rolling, the directions are chosen with regards to RD, ND (normal direction) and TD (transverse direction) for the pole figure. (Suh, 2015, p. 14-15)

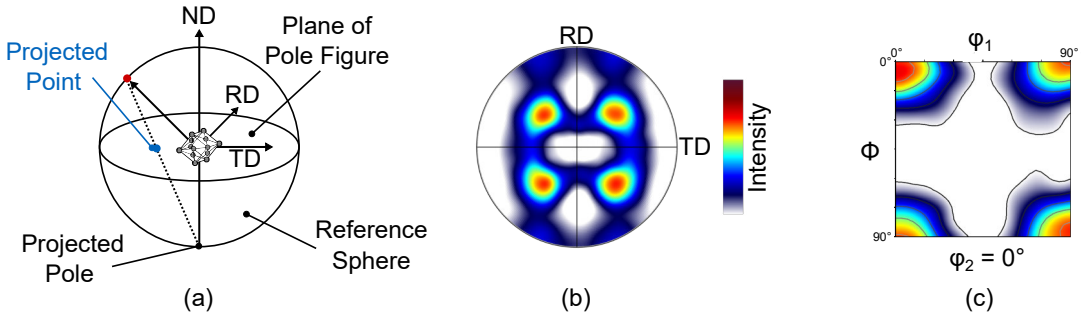

Figure 2.9: Schematic illustration of the basic concept for a pole figure (a) contour plot of a pole figure for a specific lattice plane (b) and a Euler space section for $\varphi_2 = 0°$ (c).

With the ODF, the individual intensities can be assigned to crystal components and their orientation. The most common components and their ideal appearance in the Euler angle sections is shown in Figure 2.10. For *bcc* - materials, such as steels, the section at $\varphi_2 = 45°$ is the standard, while *fcc* - materials, such as aluminium alloys, are usually analised by the sections at $\varphi_2 = 0°$, 45° and 65°. The individual components are described by the Miller indices for all symmetrically equivalent planes depicted by *{hkl}* and all symmetrically equivalent directions depicted by <*uvw*> (Spieß et al., 2019, p. 46-48). The α-fiber and the γ-fiber are common axis of orientations. For the in Figure 2.10 presented components, the Miller indices are presented in the appendix in Table D.1.

The texture also influences the mechnical properties of a material. Yoshida et al. (2007) have shown this for aluminium alloy sheets with different texture components in a virtual study. It was found, that the Cube - component has the highest formability while the Goss - component showed the lowest formability. This means, that materials with a strong Goss - component have a reduced formability compared to materials with a strong Cube - component.

Perfect crystal structures have a theoretical yield strength well above the measured values for real materials. Real materials differ from perfect crystals in that they have lattice defects. One kind of lattice defects are the one-dimensional lattice defects. The most common one-dimensional defects are called dislocations and are the main reason why plastic deformation can occur.

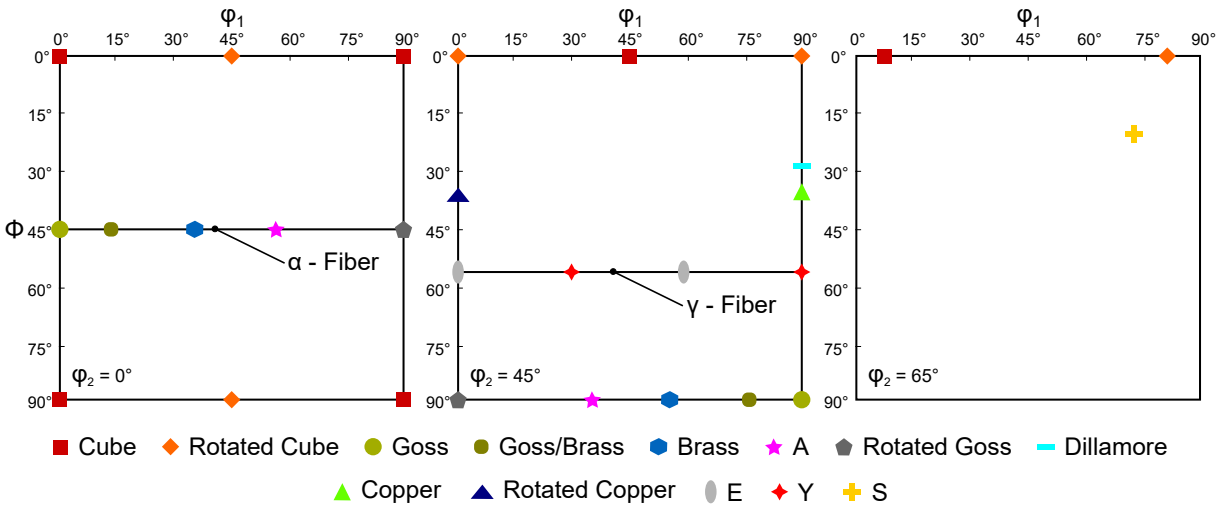

Figure 2.10: Euler angle section at $\varphi_2 = 0°$, 45° and 65° of the common texture components for fcc- and bcc-materials according to Fu et al. (2021) and Jamaati and Toroghinejad (2014).

There are two types of dislocations. On the one hand, there are edge dislocations, see Figure 2.11 (a). These are caused by the presence of a half-plane of atoms. On the other hand, there are screw dislocations, see Figure 2.11 (b). Here an atomic plane is sheared parallel to the dislocation line. The Burgers vector is used to quantify the distortion of a crystal lattice. This vector is calculated using the Burgers circuit. In an ideal crystal, the Burgers circuit would be closed. Due to the presence of dislocations, the circuit is not closed. Therefore the starting point is different from the endpoint. The Burgers vector is needed to close this gap. It is the distance between the starting point and the endpoint. (Rösler, 2012, p. 165-168)

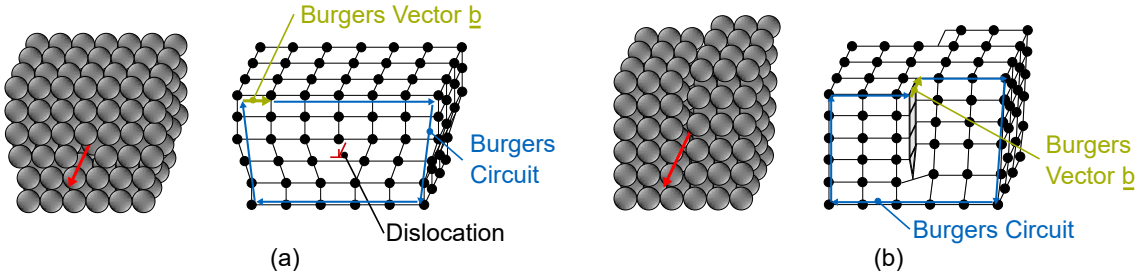

Figure 2.11: Schematic representation of an edge dislocation (a) and a screw dislocation (b) according to Rösler (2012).

If a sufficiently large shear stress now acts on a dislocation, it migrates through the crystal, see Figure 2.12. This results in a change in the bonding partner between the atoms. These processes are repeated until the dislocation has migrated to the surface of the crystal. (Rösler, 2012, p. 165-168)

The movement of dislocations in *fcc*-materials is well studied. Here, the sliding takes place on the most densely packed {111} plane in the ⟨110⟩ - direction. There are 12 possible slip systems for *fcc*-crystals. Materials with a *bcc* - lattice structure have several similarly densely packed planes on which sliding can occur. These are the {110}, {112} and {123} planes. The sliding direction is the ⟨111⟩ - direction. (Baiker, 2016, p. 41) Due to the different number of slip systems, *fcc*-materials tend to have lower formability than *bcc*-materials (Inal et al., 2005).

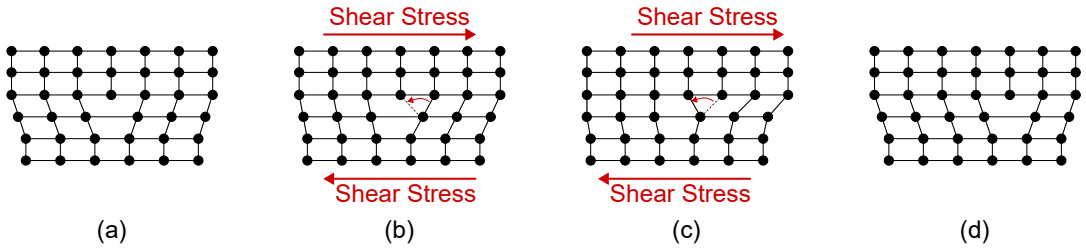

Figure 2.12: Schematic crystal structure of an edge dislocation movement with the initial dislocation (a), during elastic deformation (b), after plastic deformation with folder over bonding (c) and after unloading (d) according to Rösler (2012, p. 172).

The number of dislocations in a material is not constant during plastic deformation. Dislocations can develop at grain boundaries but also within individual grains. Within a grain, a Frank-Read source (Frank and Read, 1950) leads to dislocation multiplication and is a mechanism that allows slip to occur. A straight dislocation has two pinned ends, represented as A and B in Figure 2.13, when there is a shear stress applied, the dislocation curves into an arc. New dislocations are generated from a Frank-Read source if the critical shear stress is reached. A further increase leads to a spiralling around the pinning points until they collide and cancel themselves out. This results in a dislocation loop.

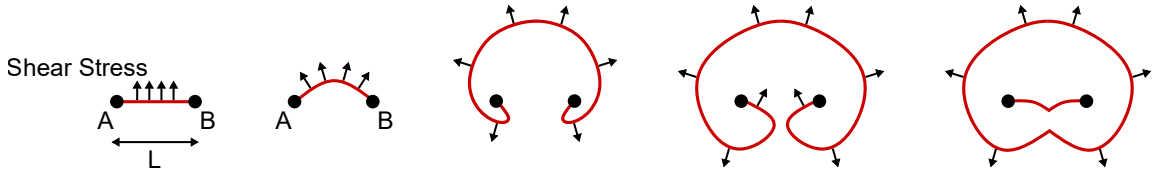

Figure 2.13: Schematic illustration of a Frank-Read source according to Hsueh et al. (2019).

The minimum stress which is required for this multiplication is called Orowan stress and is given by equation 2.12 where G denotes the elastic shear modulus, b the Burgers vector and L the distance between the two pinning points A and B in Figure 2.13. (Hsueh et al., 2019)

$$\tau = \frac{Gb}{L} \tag{2.12}$$

The increase in dislocations also leads to an increase in the flow curve, whereby the stress increases with increasing strain. This increase in stress is caused by the formation of zones of higher dislocation density. Within these zones, immobile dislocations contribute to the strengthening of grains, while mobile dislocations account for the ductility of the grain. (Zhuang et al., 2019)

In addition to the increase in dislocation density, some mechanisms lead to a decrease in dislocations. Dislocations can be annihilated. The prerequisites, accoring to Rösler (2012, p. 186), for this are:

- Equal line vector ($\underline{t}_1 = \underline{t}_2$) - opposite Burgers vectors ($\underline{b}_1 = -\underline{b}_2$)
- Opposite line vector ($\underline{t}_1 = -\underline{t}_2$) - same Burgers vectors ($\underline{b}_1 = \underline{b}_2$)

Meaning that dislocations can be annihilated when two dislocations with opposite signs meet each other, see Figure 2.14. At the beginning of plastic deformation, fulfilling these conditions is rare. Therefore, there is an increase in dislocations at the beginning of plastic deformation. In the further course, the number of annihilation processes increases due to the presence of more dislocations in the deformed material. Hence, the dislocation density tends towards a stationary value. Figure 2.14 shows an exemplary annihilation of two edge dislocations, green symbols, under shear stress. (Rösler, 2012, p. 186)

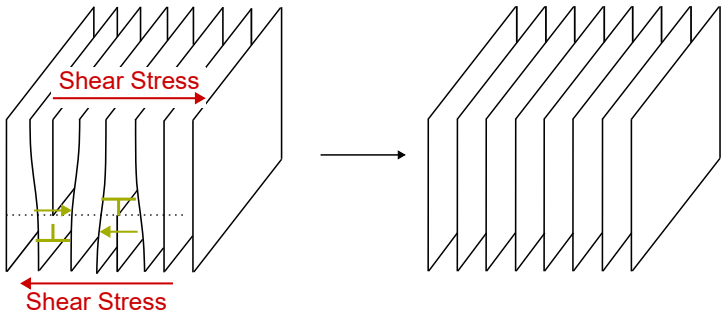

Figure 2.14: Schematic annihilation process of two edge dislocations with opposite signs according to Banabic et al. (2000, p. 12).

All the plastic mechanisms activated by local strains are then considered to result from the emergence or annihilation of mobile and immobile dislocation densities in their respective slip systems and their interaction between the slip systems. The status of a single dislocation of being mobile or immobile is not fixed during the deformation process. Mobile dislocations can be immobilised during deformation, and immobile dislocations can be released and turned into mobile dislocations. (Zhuang et al., 2019)

To measure dislocation densities, different procedures can be applied. These procedures differ in the size of the investigated area and the type of dislocations which can be measured. In-situ diffraction experiments allows the evaluation of the dislocation density by models over an area of for example 0.7 x 0.7 mm^2 as done by Vitzthum et al. (2022a). This method does not allow conclusions about individual structures but a more global observation of the dislocations inside the grains (Connolly et al., 2019). The dislocations measured by synchrotron diffraction are the sum of statistically stored dislocations (SSDs) and the geometrically necessary dislocations (GNDs) and, therefore the total dislocation density (Muránsky et al., 2019). The difference between the GNDs and the SSDs is shown in Figure 2.15.

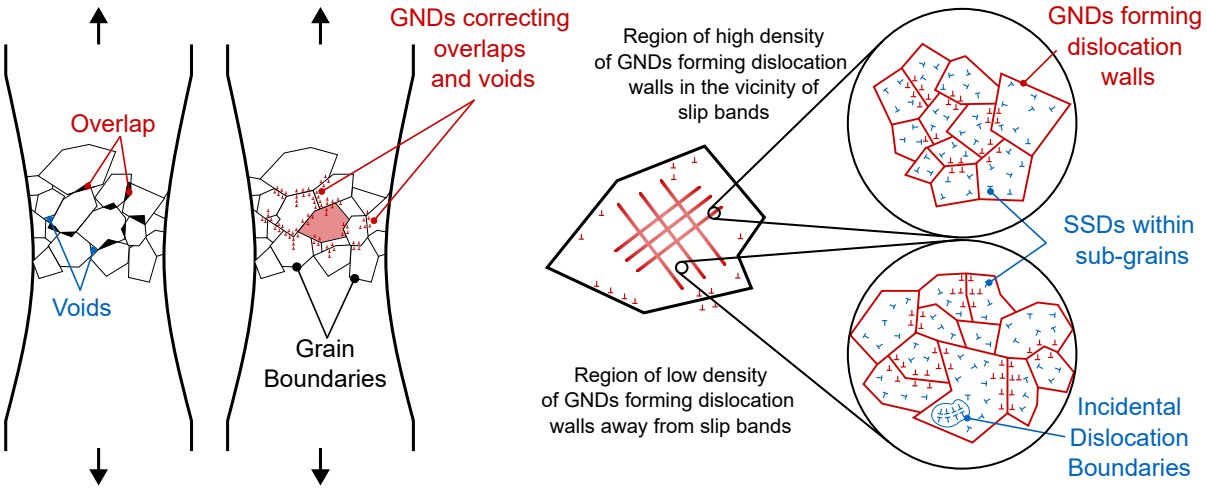

Figure 2.15: Schematic representation of GNDs and SSDs according to Ashby (1970) and Muránsky et al. (2019).

Classical EBSD can be used to determine the texture of a material but also allows the evaluation of the dislocation density over multiple grains. The determination of the dislocations is done by the lattice curvature. As only GNDs lead to a lattice curvature, SSDs can not be measured (Muránsky et al., 2019). GNDs and SSDs increase with increasing strain, but the mechanisms leading to that increase are different. The density of the GNDs is controlled by the microstructure of the material, therefore the grain size, particle size and their distribution, texture and others. The density of the SSDs is independent of the microstructure, see Ashby (1970). These GNDs are necessary to provide displacement compatibility by accommodating each other's crystal strain gradient in order to maintain continuity in the crystal (Arsenlis and Parks, 1999). In contrast to the GNDs, the SSDs have no geometrical consequence on the material and are randomly distributed (Rezvanian et al., 2007). The GNDs can subdivide individual grains and can lead to the separation of multiple grains into cell blocks. They start to form near the beginning of deformation and have a parallel structure (Hughes, 2001).

The use of a classical transmission electron microscopy (TEM) allows the visualisation of dislocations and dislocation structures. With the help of this methodology, the dislocation density can be determined without the aid of models. However, this requires a complex sample preparation. The sample must have a small thickness so that the electrons can penetrate the material. For 100 keV electrons the thickness should be in the order of 5 - 100 nanometers. The area which can be investigated is in the range of a few micrometers. (Reimer and Kohl, 2008)

Basics of Synchrotron Diffraction

Synchrotron diffraction can be used to measure the deformation of individual lattice planes during the experiment and can be used to calculate the dislocation density via models in the post-processing of the acquired data. Synchrotron diffraction is a non-destructive testing method based on diffraction. If periodic waves meet a periodic structure, such as a crystal lattice in which the atoms and lattice planes, respectively, have the same distance from each other, the interaction between these two leads to diffraction effects if the atomic distance is of a similar order of magnitude to the wavelength. The electromagnetic waves of synchrotron radiation react with the charge of the electrons of an atom and are dispersed. (Stanjek and Häusler, 2004)

The diffracted beam is composed of numerous waves that have been scattered. The beam's diffraction only occurs at certain angles, the so-called Bragg angles. At this angle, constructive interference takes place and Bragg's law (Bragg, 1913),

$$n\lambda = 2d_{hkl}sin(\Theta) \quad , \tag{2.13}$$

is fulfilled. Here n is an integer number, λ is the wavelength, Θ is the angle between the lattice planes and the incident beam and d_{hkl} is the atomic lattice spacing. If the distance s is not an integer multiple of the wavelength λ, only weak constructive interference occurs or the radiation is annihilated. The atomic lattice spacing d_{hkl} is calculated using the Miller indices of the lattice plane and the lattice parameter a:

$$d_{hkl} = \frac{a}{\sqrt{h^2 + k^2 + l^2}} \quad . \tag{2.14}$$

The geometric derivation of Bragg's law can be seen in Figure 2.16.

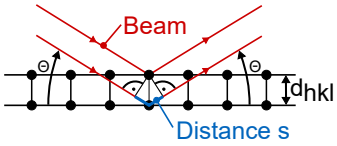

Figure 2.16: Schematic illustration of Bragg's Law according to Spieß et al. (2019).

The intensity of the diffracted beam is many times smaller than the incident beam. For some structures, no reflections occur as Bragg's law is not fulfilled. The occurrence of reflections is dependent on the crystal structure of the investigated material. For the *bcc* - and the *fcc* - crystal structures, the selection rules are listed in table 2.1, where unmixed means all numbers are even or odd, while mixed means that there are even and odd numbers. (Suryanarayana, 1998, p. 50-59)

Table 2.1: Selection rules for the bcc- and fcc-crystal structures.

Crystal type	Reflections present	Reflections absent	Resulting lattice planes
Body-centered bcc	h + k + l = even	h + k + l = odd	(110), (200), (211), (220), (310)
Face-centered fcc	h, k and l unmixed	h, k and l mixed	(111), (200), (220), (311), (331)

A beam source and a detector are required to generate the beam needed for the reflections and to measure the reflections after the diffraction of the beam. The beam used for diffraction can be generated in several ways. The two most common methods or sources are the X-ray tube and a synchrotron, see Figure 2.17. X-ray tubes have the advantage of being very compact and can therefore be used in smaller laboratories. They also require little maintenance. However, since the overall efficiency is very low (about 1-2 %) and the brightness of the beam is low, another, much more advanced radiation source has been developed. The synchrotron consists of a circular orbit, the storage ring, in which high-energy particles are accelerated. These particles emit electromagnetic radiation triggered by the acceleration through magnetic fields. The brilliance, which is used to measure the quality of the beam, is 4 to 12 times higher in synchrotrons than in X-ray tubes. This is particularly advantageous in materials science. Another advantage of synchrotron radiation is its polychromatic spectrum of the beam. This allows the wavelength of the radiation to be matched to the material being studied using monochromators. A monochromator can isolate specific wavelengths which are required to study a certain material. (Pecharsky and Zavalij, 2005, p.102-113)

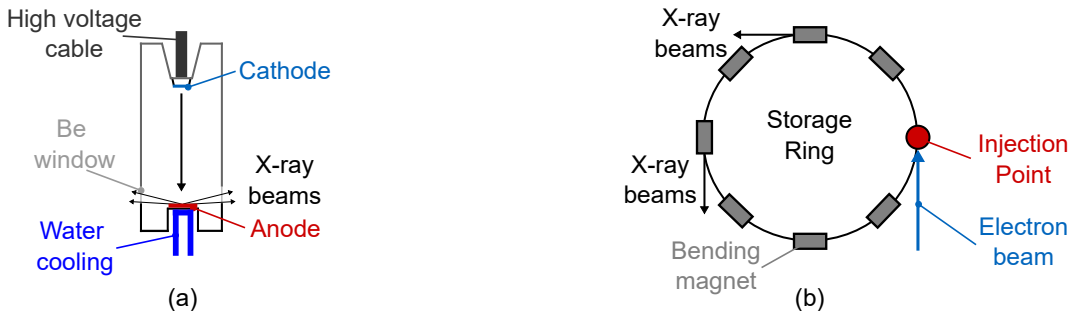

Figure 2.17: Schematic illustration of a X-ray tube (a) and a synchrotron (b) according to Pecharsky and Zavalij (2005).

The detector is there to detect and acquire the diffraction pattern. The detector must be able to detect the incident photons and convert them into a processable signal. In order to detect the entire diffraction pattern, area detectors are usually used. These can simultaneously measure the intensity of the incident radiation at several points and record the entire diffraction pattern in one shot. The number of rings recorded depends on the distance between the sample and the detector and the investigated material and its reflections. Due to the resolution being constant if the same detector is used, a lower number of rings lead to a higher density of data points. This higher density can be beneficial for a more accurate fitting of the analysis functions. (Pecharsky and Zavalij, 2005, p.128-132)

Debye and Scherrer (1916) developed a method to analyse the obtained diffraction patterns. Information about the lattice structure and lattice defects can be determined from the appearance of the rings. Within the chosen evaluation segment, see red area in Figure 2.18 (a), the intensity of the profile is summed up and plotted against the scattering angle 2θ. The resulting diffraction profiles can be further analysed. The profile peaks each represent a specific lattice plane, see Figure 2.18 (b).

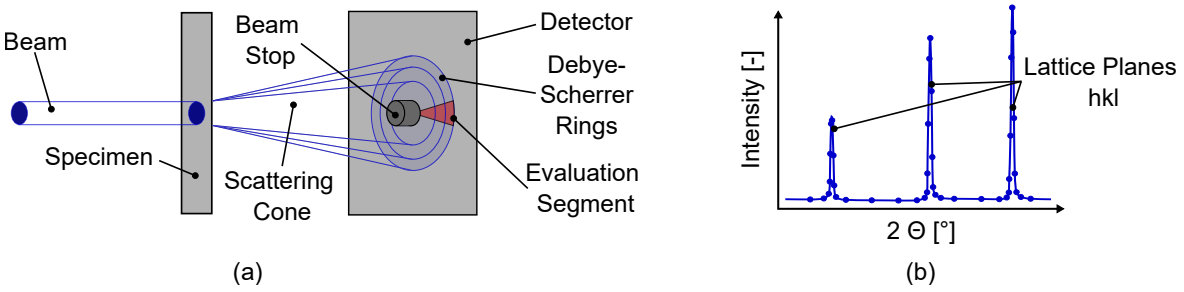

Figure 2.18: Illustration of an diffraction experiment with the resulting Debye-Scherrer rings (a) and the resulting peak profile (b).

The appearance and position of the individual peaks provide information about lattice defects or strains in the crystal lattice. To be able to describe and analyze the peaks, various parameters have to be determined. According to Spieß et al. (2019, p.273), each peak has the following mathematically determinable quantities, which are shown in Figure 2.19:

- **Background (BG)**
  The background occurs in all synchrotron diffraction experiments. Causes can be the detector noise, the sample holder or other sources of interference. The background is therefore subtracted from the peak profile. For this purpose, an analytical function is usually fitted into the background. In most cases, a linear function is sufficient to describe the background. (Pecharsky and Zavalij, 2005, p.348-352)

- **Width**
  The peak width can be specified by various parameters. Often the full width at half maximum (FWHM) is selected. Here, the width is determined at half the peak height, see Suryanarayana (1998, p.84). Another possibility is the integral width (IB). IB corresponds to the width of a rectangle whose area is equal to the area of the peak without background and whose height corresponds to the peak height.

- **Peak position**
  The peak position corresponds to the 2Θ angle at which the maximum intensity of the peak occurs.

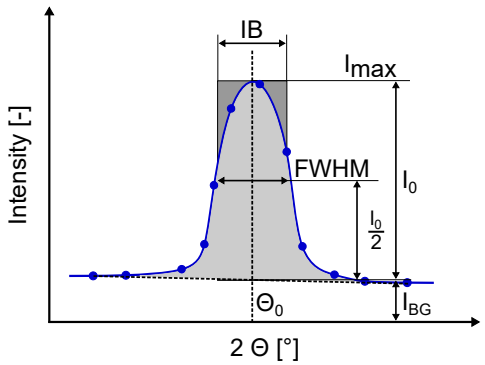

Figure 2.19: Peak profile parameters according to Spieß et al. (2019).

To determine the parameters mentioned more precisely, the peak profile is approximated through mathematical functions. The two most commonly used functions are the Lorentz and Gaussian functions, see equation (2.8) and equation (2.9). The two functions differ mainly in the rate of decrease at the base of the peak (Suryanarayana, 1998, p.212). In addition to these two

functions, other functions represent a combination of the Lorentz and Gaussian functions, such as the Pseudo-Voigt function, se equation. 2.10. (Spieß et al., 2019, p.291-292).

$$L(x) = \frac{1}{IB} \cdot \left(1 + 4 \cdot \frac{(2 \cdot IB)^2}{(x \cdot \pi)^2}\right) \tag{2.15}$$

$$G(x) = \frac{1}{IB \cdot \sqrt{\pi}} \cdot exp\left(-\frac{x^2}{IB^2}\right) \tag{2.16}$$

$$PV(x) = (1 - m_G) \cdot G(x) + m_G \cdot L(x) \tag{2.17}$$

The mathematical description of the peaks allows a more precise determination of the geometric quantities than the purely experimental data. This allows statements about the strains within a lattice, the so-called lattice strains, based on the displacement of the peak position. The change in peak width, which can be measured using the FWHM or the IB, allows conclusions to be drawn about the lattice defects in the material.

The most appropriate mathematical description depends on the material, grain size and peak profile. The Gaussian function describes a change in peak width mainly due to distortions, while the Lorentz function describes the broadening due to grain size effects. (Spieß et al. (2019, p.297))

In-situ diffraction, therefore, offers numerous possibilities for investigating materials more closely. Numerous studies have therefore been published on this topic. Results relevant to this thesis are briefly presented below.

Tomota et al. (2003) used in-situ neutron diffraction to investigate an interstitial free steel (IF-steel) and an ultra-low carbon steel in tensile tests. It was shown that the investigated lattice planes exhibit different properties. The lattice plane (200), for example, requires higher forces to be plastically deformed than the planes (211) or (110). An increase in dislocation density with increasing plastic deformation was also observed. The ultra-low carbon steel showed a higher increase in dislocations than the IF steel. The different behaviour of the individual lattice planes could also be shown for cast iron in cyclic tension and compression tests by Harjo et al. (2020). It was also possible to examine individual phases in the material, such as cementite, ferrite and graphite in more detail. Cementite exhibits the highest strength of the three phases examined.

In addition to neutron diffraction, synchrotron diffraction is also used in several publications. For example, Zhang et al. (2021) investigated the properties of an additively produced AlSi10Mg alloy using synchrotron diffraction. They observed a decrease in dislocation density early in the tensile test, which they attributed to dislocation annihilation.

Vitzthum et al. (2022b) investigated the elastic-plastic material behaviour of a CR590Y980T-DP (DP1000) steel. The diffraction profiles of the martensite and ferrite phases for three lattice planes were examined in detail. It was shown that high interphase stresses occur between the hard martensite phase and the soft ferrite phase during cyclic tensile compression tests.

The different dislocations densities obtained by X-ray diffraction and EBSD were studied by Muránsky et al. (2019) for an solution-annealed Ni201 in tensile test They found, that the dislocation density obtained by X-ray diffraction is above that of EBSD. This is mainly due to the fact, that EBSD can only detect GNDs while X-ray diffraction captures all present dislocations. For this material the SSD density is above the GND density regardless of the applied deformation.

2.3.2 Nanoindentation Experiments

The methods presented so far in this thesis for material characterisation on the macro or micro level do not allow any statement about the strengths of individual grains. To determine the hardness and, therefore, strength of individual grains, nanoindentation can be used. Here, analogous to the classic hardness measurement, an indenter tip is pressed into a polished and etched surface. The prior treatment of the sample surface allows the indenter tip to be placed on a specific grain. Due to the size of the indenter tip of a few micrometers, the hardness of individual grains can be determined (Torgal-Pacheco et al., 2019, p.141). In order to obtain the most accurate measurement of the hardness of the test surface, the surface quality is essential and must be as smooth as possible (Sabu et al., 2017, p.165-170). An exemplary representation of nanoindentation with a spherical indenter and a Berkovich indenter is shown in Figure 2.20. Using a spherical indenter has advantages concerning the independence of the hardness from the penetration depth. Swadener et al. (2002) was able to show this with iridium and oxygen-free copper samples. However, hardness is dependent on the radius of the indenter. A smaller radius will give a higher measured hardness, see Seok et al. (2014).

The nanoindentation results are not limited to the hardness of the area studied. It is also possible to directly determine the elastic modulus, the fracture strength, the creep behaviour and the yield strength (Torgal-Pacheco et al., 2019, p.142).

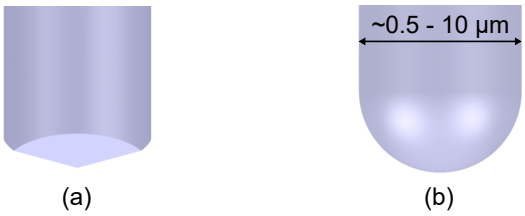

Figure 2.20: Different indenters for nanoindentation, Berkovich tip (a) and the spherical tip (b).

Other characteristic values of individual grains or phases can be determined inversely using FE simulation. For example, Casals and Alcalá (2005) identified the yield strength, Young's modulus and the hardening parameters through an FE simulation of the nanoindenter tests with a Berkovich tip. If a sufficiently small diameter of the indenter tip is selected, very small grains, such as the martensite grains of a DP - steel, can also be investigated. Choi et al. (2009) determined the flow curves for the martensite and ferrite phases inversely using a spherical indenter. The indenter radii were 550 nm and 3.3 µm, respectively. A similar approach was taken by Seok et al. (2014) to determine material parameters for ferrite and pearlite.

Nanoindentation is also able to determine different strengths within a grain. Ohmura et al. (2005) showed that areas near a grain boundary have a higher hardness than areas in the centre of the grain. It is crucial to ensure that the grain size is significantly larger than the indenter tip to avoid any effects of the grain boundaries on the force-displacement curve when determining the characteristic values of a single grain (Miyahara et al., 2001).

2.4 Failure of Metallic Materials

The presented methods to characterise sheet metals often end with the fracture of the specimens. This fracture can be divided into two main groups for sheet metals. On the one hand, the cleavage fracture and, on the other hand, the ductile fracture. The fracture type is described by the shape of the fracture surface and the underlying fracture or failure mechanism, see Figure 2.21.

Firstly, the cleavage fracture. The fracture surface of a cleavage fracture shows a brittle failure mode with a smooth surface with the cleavage faces tending to be normal to the maximum principal stress. The crack is often initiated by the fracture of a brittle inclusion in the material, most often carbides. The crack direction can be changed when the crack crosses a grain boundary. Grain boundaries are also an essential factor in the resistance of the material against the propagation of cleavage cracks. The crystal lattice orientation influences the occurrence of a

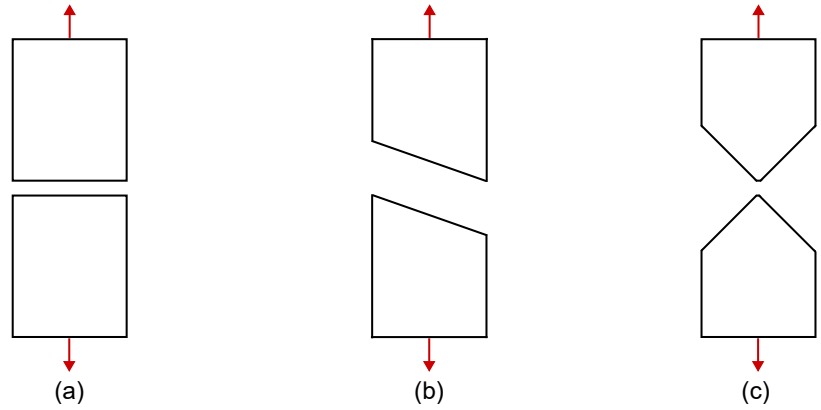

Figure 2.21: Fracture types where (a) represents cleavage fracture, (b) ductile shear fracture and (c) ductile fracture.

cleavage fracture. The fracture occurs over dense atomic planes, meaning for the *bcc*-materials the (100) plane and for *fcc*-materials the (111) plane. The fracture surface is characterised by flat areas with no dimples and sharp edges, see Figure 2.23 (c). (Pineau et al., 2016)

The ductile fracture can be divided into two types. Failure by instability and failure by void coalescence, see Figure 2.22.

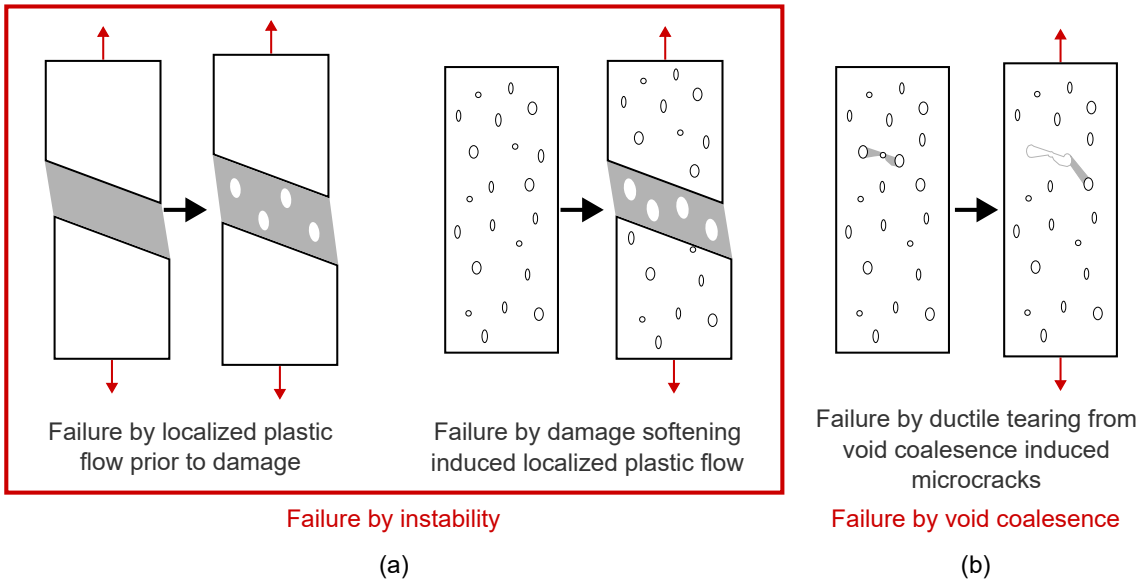

Figure 2.22: Ductile failure types with (a) failure by instability and (b) failure by void coalescence according to Pineau et al. (2016).

The mechanisms behind ductile failure by void coalescence are void nucleation, void growth, void distortion and void coalescence. Void nucleation can happen at second-phase particles or grain boundaries, for example. Also, hard inclusions can lead to a decohesion between the particle and the matrix, or the hard inclusion itself can crack, causing new voids.

After nucleation, the void grows with increasing deformation. Void growth depends on the applied stress state. Further deformation of the material also causes the shape of the void to change, which can later influence fracture. The volume of a void is almost constant within a triaxiality range of 0.33 - 0.5 (uniaxial to plane strain), but they are elongated along the loading direction. It is noted that void nucleation is still occurring while other voids are already growing. With sufficiently large voids, the voids start to interact with each other. This interaction eventually leads to the joining of two voids to form one large void. The continued deformation of the material leads to fracture. The fracture surface of such a ductile failure is characterised by many small pits, mainly caused by the presence of voids during deformation, see Figure 2.23 (a). (Pineau et al., 2016)

Looking at ductile shear failure, the process is different. Failure by instability usually has one or more shear bands occurring, often arising at a lengthscale of a single grain (Tekoğlu et al., 2015). Microscopic inhomogeneities may also trigger the development of shear bands, but microstructural factors are crucial for the localization of plastic deformation. Inside the shear band, the voids can still nucleate, grow, and coalesce. The presence of voids is not necessary, but they can promote this kind of fracture. During ductile failure by instability, the fracture surface can exhibit slanting, often called shear failure. This shear failure can occur even without the presence of a shear component in the loading. Under tensile stress, a load maximum is observed, related to cross-sectional area reduction and geometric softening. Compared to the fracture surface of a ductile failure, the shear failure shows sheared dimples with a parabolic shape in the direction of the deformation, see Figure 2.23 (b). (Pineau et al., 2016)

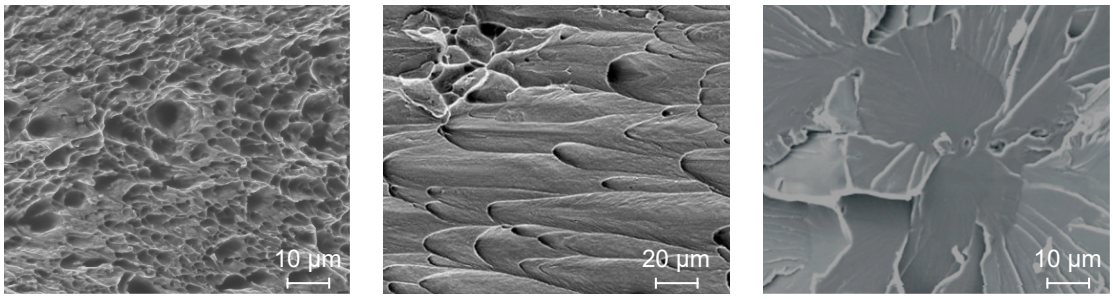

Figure 2.23: Ductile fracture surface (a), a ductile shear failure according to Zhang et al. (2022) and a cleavage fracture surface according to Chen and Cao (2015).

The presence of voids and their interactions is often linked to the term "Damage". Tekkaya et al. (2015) defined damage as a summary of all effects that weaken the material, such as voids, cavities, micro cracks and shear bands.

Dual-phase steels, with their two phases, have been the research focus for a long time. The two phases present lead to multiple damage mechanisms. Maire et al. (2008) used X-ray microtomography to determine the void sizes during tensile tests of a dual-phase steel DP600. It was shown that the higher the strain, the bigger the number of cavities and the diameter of the voids grows. The most significant increase was observed after the onset of necking.

The effect of the martensite content was investigated by Sun et al. (2009). The martensite content influences the failure mode. They also stated that ductile failure of dual-phase steels is a local phenomenon where the region of interest influences the observed failure mode.

The strain where damage accumulates and void nucleation occurs depends on the material. For a micro-alloyed steel HY-100, a nucleation strain of $\varepsilon = 0.03$ is suggested for a notched tensile test specimen (Chae et al., 2000). For dual-phase steel DP600 martensite cracking starts at $\varepsilon = 0.03$ and at $\varepsilon = 0.09$ martensite/ferrite decohesion occurs in tensile tests. (Avramovic-Cingara et al., 2009)

The primary mechanism leading to the final failure of a DP600 in tensile test experiments was the coalescence of voids caused by martensite cracking. Due to the banded structure of the martensite within the ferrite matrix, the presence of voids depends on the loading direction. A uniaxial loading under RD leads to an increased number of voids. (Aşık et al., 2019)

For the aluminium alloys AA6005 and AA6060 Lassance et al. (2007) has found two main damage initiation mechanisms: Particle fragmentation and interface decohesion between the matrix and the particle. As for the dual-phase steel, these two materials also have a softer matrix and hard, brittle particles which are dispersed in the matrix. After the voids nucleate, the initially flat voids open up by plastic deformation and start to coalesce.

Tasan et al. (2009) investigated the damage mechanics in Nakajima experiments. The void area fraction was found to be dependent on the strain path. No voids were found below the FLC for IF-steel, and damage plays a role only beyond localisation. On the other hand, the DP-steel showed significant damage behaviour, even below the FLC.

2.5 Non-proportional Load Paths

Non-proportional load paths are characterised by the fact that the stress state, and consequently the strain state, changes during the experiment or the deep-drawing process of a sheet metal part, see the schematic illustration in Figure 2.24. This non-proportionality can influence the mechanical behaviour, the formability of a material and the failure mode.

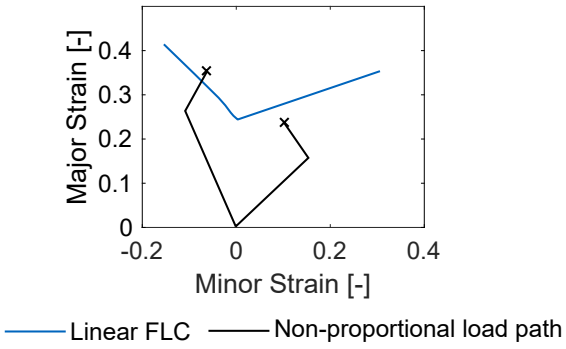

Figure 2.24: Schematic illustration of two non-proportional load paths.

2.5.1 Experimental Creation of Non-proportional Load Paths

The generation of non-proportional load paths on a laboratory scale can be achieved using different experimental approaches. On the one hand, non-proportional load paths can be generated using cruciform specimens. The clamping force or the tensile force in the arms must be adjusted for this. This procedure also allows the generation of non-proportional load paths without unloading the specimens between the different loads, as done by Song et al. (2017) for a dual-phase steel DP600 or an X5CRNi18-10 stainless steel by Zistl et al. (2022).

On the other hand, various tools have been developed to produce homogeneously pre-formed specimens from which different specimen geometries can be produced in the further course. If only uniaxial pre-forming conditions are investigated, using oversized tensile specimens may be sufficient to set the strain conditions. This procedure requires that sufficiently large specimen holders are available to clamp the specimen across its entire width. Manopulo et al. (2015) has done this for DC05 and AA6016. This method can also be used to uniaxially pre-form high-strength materials such as DP1200, see Larsson et al. (2011).

The use of a Marciniak experimental setup allows the pre-forming for different stress conditions, see Lian et al. (2022). However, as the Marciniak punch has a diameter of only 100 mm, the specimen sizes for the consecutive tests with pre-formed specimens are limited. This problem

can be avoided by using oversized Marciniak tools. Werber et al. (2012) used a scaled cylindrical Marciniak punch to introduce pre-forming into the material. Its diameter was 200 mm for plane-strain pre-forming and 340 mm for biaxial pre-forming. The uniaxial pre-strains were generated using a specially developed setup based on a tensile test setup.

A deep-drawing tool was developed by Weinschenk and Volk (2017) to enable pre-forming from uniaxial to biaxial stress states using a single tool. The stress states are generated by different specimen geometries, analogous to the Nakajima test. A circumferential draw bead is provided to avoid slipping between the sample and the blank holder. The tool is shown in Figure 2.25 and allows a homogeneously pre-formed area of approximately 100 mm in diameter, regardless of the pre-forming height. This area is large enough to cut out various specimen geometries. To determine the strains after pre-forming, a grid is etched onto the surface of the specimens prior to the pre-forming process. The distance of the grid is measured after the pre-forming process by an optical measurement system.

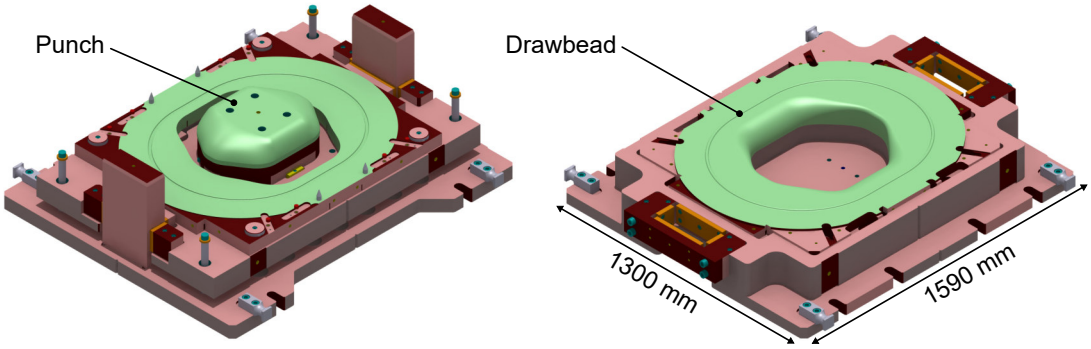

Figure 2.25: Modified Marciniak tool used to pre-form specimens by Weinschenk and Volk (2017).

2.5.2 Influence of Non-proportional Load Paths on the Material Behaviour

Formability

Müschenborn and Sonne (1975) investigated the influence of the forming history on the FLC of two different steel grades. In general, a pre-strain on the left side of the FLC ($\varepsilon_2 < 0$) leads to an FLC above that of the initial material. If, on the other hand, the material is pre-strained in areas with a positive secondary deformation ($\varepsilon_2 > 0$), the plane-strain point of the FLC is below that of the initial material. These results could be confirmed by Graf and Hosford (1993)

for AA2008-T4 and AA6111-T4, see Figure 2.26 where the linear FLC is shown in green. Also, the aluminium alloy AA6016-T4 is sensitive to non-proportional load paths, as shown by Ofenheimer et al. (2005). A uniaxial pre-forming also leads to higher forming limit strains under a biaxial post-loading observed for the AA6111-T4 alloy.

But the effects are not limited to aluminium alloys. Arrieux et al. (1987) investigated pure titanium with a thickness of 0.44 mm and Da Barata Rocha et al. (1985) an armco iron sheet metal. For those materials, the same effects were observed, a uniaxial tension pre-forming leads to an increase in the formability, while a biaxial pre-forming leads to a reduction of the formability in the plane-strain state.

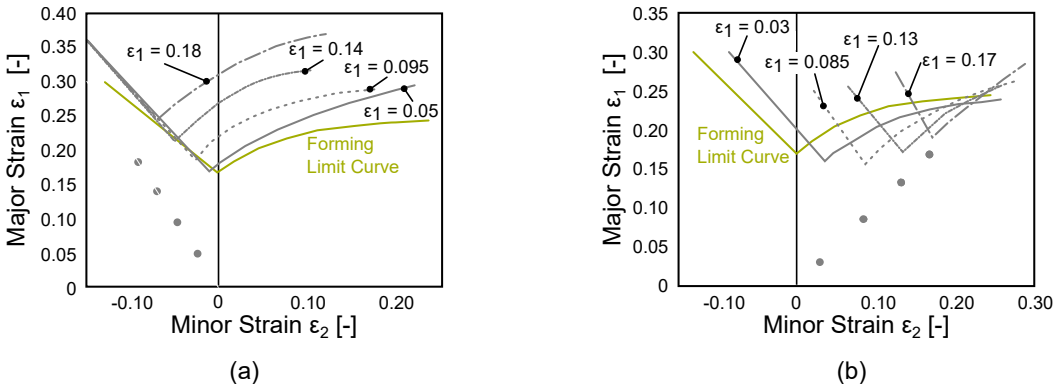

Figure 2.26: Influence of a uniaxial pre-forming (a) and a biaxial pre-forming (b) on the FLC of an AA6111-T4 according to Graf and Hosford (1994).

Mechanical properties

Non-proportional load paths do not only affect the formability of sheet metals. Also, the mechanical parameters are different when a non-proportional load path occurs. Barlat et al. (2003) investigated a commercially pure aluminium AA1050-O after various uniaxial pre-forming levels and different post-forming stress states. The higher the pre-forming state, the more the stress-strain curves differ from the initial one. A softening behaviour could be observed, leading to a lower yield stress. The reason for this behaviour was explained by the presence of dislocation structures after pre-forming. The structures of the second strain path increment superimpose these structures. Many studies have been conducted to investigate the behaviour during tension-compression experiments, so-called reverse loading. For example, Kim et al. (2018) conducted tension-compression experiments for two steel grades (DP780 and CHSP45R). Both steels showed a significantly lower yield strength after a uniaxial tension pre-forming of 5 %.

Next to the presence of a change in the stress state after pre-forming, a change in loading direction also influences the material behaviour. Tarigopula et al. examined the influence of uniaxial pre-forming on tensile test specimens (Tarigopula et al., 2008) as well as plane-strain and shear specimens (Tarigopula et al., 2009) with a change in the loading direction. The dual-phase steel showed that a change in loading direction also influences the onset of yielding towards lower values, so-called softening. The higher the change in loading direction, the more significant the influence is, with the biggest impact occurring at a change in loading direction by 90°. These findings were confirmed by Sun et al. (2009) for a DP980 steel. For the shear and plane-strain experiments, a change in the loading direction only marginally affects the material behaviour. Larsson et al. (2011) showed that the uniaxial pre-forming also influences the yield locus of the material. A mixed isotropic and kinematic hardening model is required to predict the material behaviour.

For the aluminium alloy AA5754 Lian et al. (2022) have analysed the influence of different pre-forming states. The AA5754 alloy showed a lower yield strength but an increased strain hardening behaviour after pre-forming under various stress states. This behaviour may be due to dislocation interactions and activating different slip systems. Nevertheless, texture plays only a marginal role in the material behaviour.

Figure 2.27 represents the occurring changes in the flow curve. It has to be noted that from a plasticity point of view, *cross-loading* refers to a change in the loading direction of around 45-60°. At those changes, the deviatoric stress tensor prior to and after a change in the load path is vertically aligned. A change in the loading direction by 90° is referred to the term *orthogonal loading*. (Ha et al., 2013)

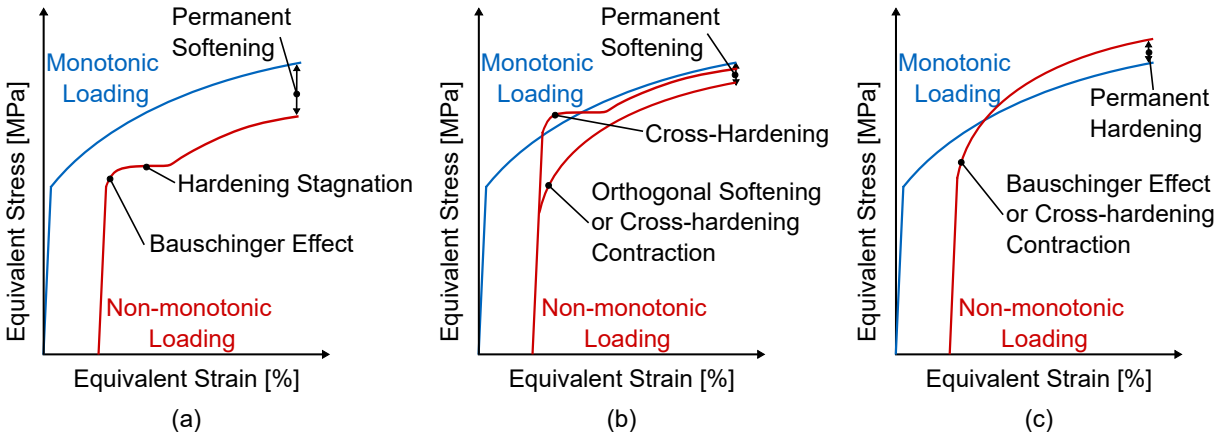

Figure 2.27: Schematic representation of the transient and permanent behaviour of reverse loading (a), cross loading (b) and a combination of both (c) according to Lian et al. (2022) and Qin et al. (2018).

Next to the onset of yielding also, the fracture elongation can be influenced. Toyoda et al. (2004) showed this for a ferritic single-phase steel. Here, a uniaxial pre-forming up to 11 % significantly reduced the fracture elongation of the specimen after a change in loading direction by 90°. These findings were confirmed by Vincze et al. (2019) for an aluminium alloy AA1050-H24. In that study, the material showed almost instant necking after a uniaxial pre-forming of 13.3 % and a change in loading direction by more than 45°. Nevertheless, the texture is not the primary source of the material response at those pre-forming levels. At higher pre-forming levels, Barlat et al. (2003) found that the texture can play a significant role. But for this, the pre-forming level must be around $\varepsilon = 0.3$.

Dislocations

Many researchers have explained their findings by the presence of dislocation structures after pre-forming. Teodosiu and Hu (1998) observed the presence of dislocations in a mild steel. In the investigated steel, dislocation structures gradually form during deformation. When the plastic slip is carried out by one slip system, these structures are more or less parallel to the slip plane. In the case of a second deformation step orthogonal to the first one, a work-softening can occur. For the work-softening to occur, a sufficient pre-forming level is necessary. This also leads to a localized deformation at the intergranular scale.

For an IF-steel, Wilson and Bate (1994) have found that orthogonal loading significantly reduces the formability and cross-hardening after a certain pre-forming level. The loss of formability goes hand in hand with the presence of shear bands. Using transmission electron microscopy (TEM) it was found that dislocation structures have formed inside the grains. The orientation of the structures varied with the orientation of the grain. After orthogonal loading, the existing cell structures were disrupted and dissoluted, and new structures began to form. This process is accompanied by a reduction of the hardening rate leading to premature macroscopic instability.

The dissolution and rearrangement of dislocation structures was also observed by Clausmeyer et al. (2013) for a DC06 steel. After a uniaxial tension pre-forming, the structures had a quadrilateral shape. If the second loading direction is perpendicular to the first one, so-called orthogonal loading, dislocation structure elements characteristic for both load paths are visible. Nevertheless, the old structures are weakened.

Vrettou et al. (2022) investigated an mild DX54 steel at different pre-forming levels using EBSD. Subsequent loading of the specimens in the orthogonal direction leads to a significant increase in the GND density compared to the proportional load case. The GND structures were only

visible after a certain pre-forming level. Prior to this level, the GND density is only increased at the grain boundaries. The pre-forming level required to see the GND structures significantly reduced the formability in the orthogonal load case. The authors contributed this behaviour also to the texture evolution of the material, where an increase of the {200} texture was observed.

Wejdemann et al. (2013) showed that when the direction of loading in the tensile test with copper is changed by 90° after pre-forming, a change in material behaviour occurs. Thus, a reorganisation of the internal stresses is visible at the beginning of the test. After the development of the stress state that corresponds to the applied load, individual sub-grains deform plastically. With increasing deformation, a reorganisation of the dislocation structures occurs, which were developed during the pre-forming process.

This behaviour could also be shown by van Petegem et al. (2016) for an austenitic 316L stainless steel employing an orthogonal loaded tensile test specimen. If there is a change in the loading direction by 90° after a preliminary pre-forming, a decrease in the dislocation density occurs at the beginning of the experiment. This is caused by the formation of new dislocations with the opposite sign. These new dislocations meet old dislocation structures and annihilate each other. With increasing deformation, this effect weakens, and there is a renewed increase in dislocation density due to plastic deformation.

The texture of a material is also dependent on the applied load. This can also be observed using in-situ diffraction. For example, Collins et al. (2017) investigated non-proportional load paths in-situ using a cruciform specimen. This showed that the texture changes almost instantaneously after a load-path change, and the developed fibers are not shown to be strongly influenced by the pre-strain. Likewise, dislocations introduced into the material by pre-deformation play a role in the further loading of the material, as shown by crystal plasticity modelling.

Modelling of the Mechanical Behaviour

Different models have been proposed to accurately simulate the material behaviour, focusing on the flow curve and yield locus. A commonly used one is the homogeneous anisotropic hardening model (*HAH* - model) by Barlat et al. (2011). This model has been extended several times (see Barlat et al., 2014 and Barlat et al., 2020) and has been used to simulate the effects of strain path changes on DP600 by Hérault et al. (2021) and by Ha et al. (2013) for a deep drawing steel as well as a DP780 steel. Two parameters thereby represent the effect of dislocations and the microstructure. For the deep drawing steel, the transient hardening behaviour is captured well, regardless of the change in the loading direction. The results for the DP780 steel showed that

the change in loading directions needs to be above a certain level so that the onset of yielding is accurately captured when using the HAH_{13} - model. This problems were overcome by the proposed HAH_{20} - model.

Another possible way of simulating such complex strain paths is crystal plasticity. Juan et al. (2022) used a phenomenological and dislocation-based model to simulate non-proportional load paths for an AA5754-H111 aluminium alloy. For such models, the parameter calibration process is challenging. The dislocation-based models require additional information about the microstructure and have more parameters affecting the results, like the dislocation density. The prediction accuracy of the two models strongly depends on the correct parameters. Using a machine-learning-based approach coupled with a genetic algorithm can help to find the correct parameters as done by Juan et al. (2023).

Failure

The presence of non-proportional load paths affects the failure mode, and hence the fracture surfaces as well. For HY-100, different plane-strain pre-forming levels have been investigated by Chae et al. (2000). The level of pre-forming as well as the pre-forming state (e.g. uniaxial or biaxial) have a direct impact on the reached failure strains and fracture surfaces. The fracture surfaces are dependent on the pre-forming stress state. The specimens which experienced a pre-forming under high triaxiality have a different fracture surface. The elongated voids which are initiated in the pre-forming process influence the following failure mechanisms.

Tension-torsion experiments can be conducted using tubular specimens as done by Papasidero et al. (2015) for an aluminium alloy AA2024-T351. A pre-compression and pre-torsion of the specimens lead to an overall increase in the fracture strain, while a pre-tension leads to a decrease in the fracture strain. Also, the place of the crack occurrence is changed with different pre-forming states. Different mechanisms occur within the fracture surface, from a ductile fracture surface with dimples to shear dimples and abrasive marks.

For sheet metals, the use of cruciform specimens allows the creation of non-proportional load paths not only to determine the FLC but also to take a closer look at the fracture surface after non-proportional load paths. Brünig et al. (2019) and Gerke et al. (2019) have assessed the influence of non-proportional load paths on an aluminium alloy AA6082-T6 with a thickness of 4 mm. By using two different cruciform specimen geometries, the so-called H-specimen and the X0-specimen, respectively, non-proportional load paths were applied. After a shear pre-loading followed by a superimposed tension, the fracture surface had smaller voids, and a more

predominant shear failure mode was observed. When the loading steps are switched, therefore pre-loading under tension, followed by shear, voids are larger and more predominant. The X0-specimens allowed different stress states to be applied. Using the X0-specimens, tension-tension loading leads to major void growth, while tension compression leads to shear mechanisms. For a stainless steel X5CrNi18-10, these findings were confirmed using the X0-specimens by Zistl et al. (2022). The experimental setup, a biaxial test machine with four independent cylinders, allows a continuous change in the load path without unloading between the two load cases, and pressure loads are also possible.

2.5.3 Methods to predict Failure after Non-proportional Load Paths in Deep-drawing

The linear FLC can only correctly predict failure when a linear load path occurs, namely a load path without change in the stress state. In real sheet metal components, however, this is hardly the case. Various models have been developed to predict failure after complex, non-proportional load paths. The models are based on different approaches.

Arrieux et al. (1987) have introduced a stress-based FLC (FLSC) as an alternative to the strain-based FLC. Based on this work, Stoughton (2000) extended this method for non-proportional load paths. The assumption here is that the material failure in stress-based FLC is independent of the load path, and therefore the failure is correctly predicted for any load path. A disadvantage of the stress-based FLC is that at the time of failure, the slope of the flow curve is very small. If minor deviations occur due to the test procedure, the material or the extrapolation approach of the flow curve, these have a significant effect on the achievable strains. Another point is that it is often difficult to visually determine the onset of necking from the diagram. To solve this problem, Stoughton and Yoon (2012) developed the Polar Effective Plastic Strain diagram (PEPS). This method is based on the effective plastic strain. This is directly coupled with the stress tensor via the yield locus and flow curve. Since the PEPS diagram has a similar appearance to the strain-based FLC, failure can be easily determined. This method has already been verified for various sheet metal components, see Dick et al. (2016). But still, any deviation of the extrapolated flow curve or the hardening behaviour and the actual material behaviour leads to wrong predictions.

The stress-based methods listed here all have the disadvantage that the material behaviour must be determined very precisely. Deviations in the yield locus or the flow curve most likely lead lead to incorrect results. Investigations with the aluminium alloy AA6014 have also shown that

the assumption that stress-based FLCs are independent of the strain path does not hold true for all materials. This means that a major advantage of the stress-based methods is lost for this material. (Werber et al., 2013)

Another stress-based method is the Modified Maximum Force Criterion (MMFC) published by Hora et al. (1996) . Here, the assumption is made that a plane strain state prevails during the localization of the specimen, as after the occurrence of the maximum force. The model has been extended to take the strain rate sensitivity, the radius of the punch, the sheet thickness or distortional hardening models into account, see Manopulo et al. (2015) and Hippke et al. (2018). Nevertheless, this method also requires an accurate description of the material. The yield locus for high strains must be determined to correctly represent the high strains that occur at the time of failure. The prerequisite that the material is a homogeneous medium must also be fulfilled, see Hora et al. (2013). This means that the material has to have a sufficient number of grains over the thickness and in the case of more than one present phase, the two phases have to be more or less homogeneously dispersed.

In addition to the previously mentioned methods, other models have been developed to circumvent the disadvantages of the stress-based methods. These are mostly based on experimental data. Here, different linear and bi-linear load paths are investigated experimentally and used as a data basis for the models.

Drotleff and Liewald (2018) used such a database to establish a mathematical relationship between parameters from the tensile test and the formability. For this purpose, materials were uniaxially pre-formed, and subsequent tensile tests were carried out. To fully calibrate the model, 36 tensile tests are necessary, and no optical measurement system is required for the evaluation. Based on the fracture elongation, the strain hardening exponent, and the r-values, the FLCs for bi-linear strain paths can be calculated. The calculation is based on mathematical formulas, which differ depending on which point of the FLC is to be calculated. These formulas have been validated for the aluminium alloy AA6014, the dual-phase steel DP600 and the mild steel DX54D by Drotleff (2021).

Another strain-based method was developed by Werber et al. (2014). The approach is based on Nakajima experiments with pre-formed samples in order to create bi-linear load paths. Here, the remaining major strain is determined as a function of the effective pre-forming ε_{eff} and the ratio β of the minor strain ε_2 to the major strain ε_1. Failure can be determined visually with this method. If the strains of a component are below the three-dimensional surface, no failure occurs. This possibility of visualisation makes the method easily applicable.

A similar approach is taken with the Generalised Forming Limit Concept (GFLC) by Volk et al. (2012). Here, the failure is calculated using the strain ratio β of the minor and major strain and the true load path length $l(\beta)$, which is dependent on β . The experimental data basis consists of the linear FLC and six different bi-linear FLCs with different pre-forming states. The pre-forming states cover the uniaxial, plane-strain and biaxial strain state. For these three pre-forming states, two different pre-forming levels are required. Those pre-forming levels should be around 25 % and 50 % of the linear FLC. Nakajima specimens are then taken from the pre-formed specimens and deformed until failure. From this, six bi-linear FLCs are obtained, serving as the data basis for the GFLC. The pre-forming states for a HC300X steel and the resulting FLCs are shown in Figure 2.28 (a).

The linear FLC serves as a reference variable for the GFLC. Each load path has a unique strain ratio β and a unique load path length $l_{FLC}(\beta)$. For bi-linear load paths, each strain increment can now be determined into a corresponding strain ratio β_{pre} and β_{post} as well as a load path ratio λ_{pre} and λ_{post} from which the strain path length of the increment l_{inc} can be calculated.

This parameterisation of the load paths allows meta-modelling to predict failure according to bi-linear load paths. Here, the isoparametric approximation of a 4-node Lagrange element from the FE simulation is applied. The pre-forming points are plotted in a diagram, similar to the example shown in Figure 2.28 (b).

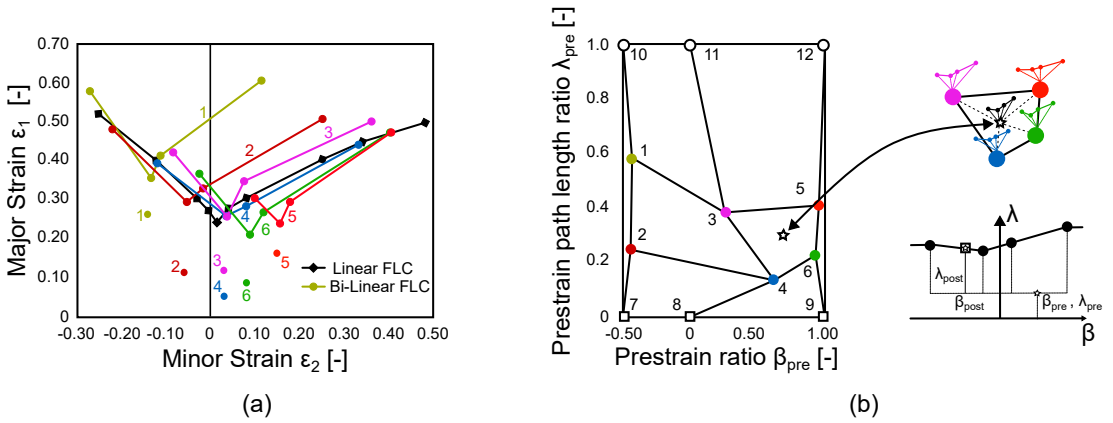

Figure 2.28: Database for the GFLC-model of a HC300X steel (a) and the parametrisation and interpolation process (b) taken from Volk et al. (2012).

With a bi-linear load path, any given pre-forming now lies within one of the regions in the diagram. Using Lagrange interpolation, the maximum possible post-strain and thus the maximum length of λ_{post} can now be determined depending on the strain ratio β_{post} of the post-strain. If the sum of λ_{pre} and λ_{post} are below 1, no failure occurs. To determine failure the failure variable λ_{GFLC} is calculated as follows:

$$\lambda_{GFLC} = \lambda_{pre} + \lambda_{post} = \frac{l_{inc}(\beta_{pre})}{l_{FLC}(\beta_{pre})} + \frac{l_{inc}(\beta_{post})}{l_{FLC}(\beta_{post})} \tag{2.18}$$

One advantage of the GFLC is that for individual material classes, e.g. Al6xxx series or dual-phase steels, the experimental effort of creating the data basis only has to be made for one material of this class. It is sufficient to adapt the linear FLC for the other materials within the same class of materials. Volk et al. (2012) were able to show this procedure for the two steel grades HC450X and HC300X. Nevertheless, a total of 72 experiments must be carried out in order to create the experimental database for a material or a class of materials. This results from the six pre-forming states, the four post-forming states and a minimum number of three valid samples per configuration.

To enable the evaluation of arbitrary strain paths, the principle of equivalent pre-forming was implemented by Volk and Suh (2014). Here it is assumed that all points with an equivalent pre-forming have the same remaining formability. Any load path can be divided into several bi-linear load path increments. These bi-linear increments can be converted into a linear load path using the GFLC. By iteratively applying this procedure, any arbitrary load path can be analysed and converted into a linear load path. This makes it easier for the user to visually determine if failure occurs or not, as the linear FLC can be used to visualize the onset of necking. Figure 2.29 shows a schematic procedure for the evaluation process.

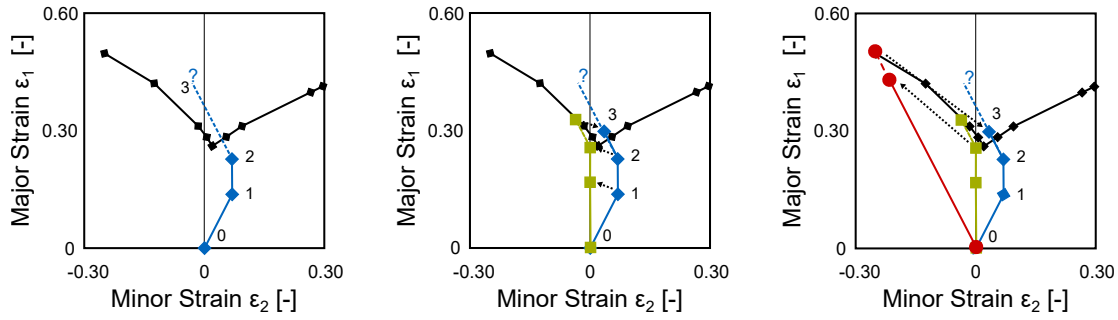

Figure 2.29: Procedure for the evaulation of the remaining formability of an arbitrary load path

A brief conclusion about the advantages and disadvanteges of the presented models can be found in Table 2.2. All of the presented models have the limitation that only load path chanegs are taken into account. Any further changes influencing the formability, such as the loading direction or temperature, are not taken into account.

Table 2.2: Advantages and disadvantages of the presented stress- and strain-based methods to predict failure after non-proportional load paths.

Model	Advantages	Disadvantages
Stress-based methods	Hardly affected by load path Models can easily be extended	Precise description of the yield locus Material hardening has great influence on the failure strains Difficult evaluation of failure
Strain-based methods	Simple visual evaluation of failure Models can easily be extended Scaling within material class possible	Comprehensive experimental database Complex experimental setup Failure strains are affected by load path

2.6 Conclusions

Non-proportional load paths significantly influence the material behaviour. Numerous studies have already shown the influence on the flow curve, formability, dislocations and damage behaviour. How strongly non-proportional load paths influence the material behaviour depends on the lattice structure, the microstructure and other parameters. Numerous models have been published which are able to reproduce the material behaviour in FE-simulations.

Another major influencing factor is a change in the direction of loading after pre-forming. A change in the loading direction can lead to a significant reduction in formability, see Wilson and Bate (1994). Current models that can predict failure after non-proportional load paths have yet to demonstrate their suitability for predicting formability after non-proportional strain paths in combination with a change in the loading direction. Likewise, different approaches explain the cause of the material behaviour. While some researchers found the texture development as the main reason (see Vrettou et al. (2022)) others found dislocation structures to be the main reason (see Wilson and Bate (1994) or Wejdemann et al. (2013)). The main reasons still need to be conclusively clarified. In-situ diffraction experiments can gain further knowledge about the microstructural processes during deformation, which can be linked to the observed macroscopic material behaviour.

3 Aims and Scope

3.1 Challenge and Approach

The results presented by various researchers show that non-proportional load paths have a significant influence on material behaviour. However, in most cases, the tests to determine the formability in multi-stage tests are limited to a change in the stress state. Changing the direction of loading, however, can significantly influence the formability. For example, an industrial part of a car wheelhouse, made of a mild CR4-steel, shows that a change in loading direction by 90° after plane-strain pre-forming can lead to failure well below the linear FLC with safety margin (yellow line), see Figure 3.1. The strain path is determined by an FE-simulation of the deep drawing process. The pre-forming in this part is created by the passing of a draw bead. Such a draw bead is used in many forming tools to control the material flow during the deep drawing process.

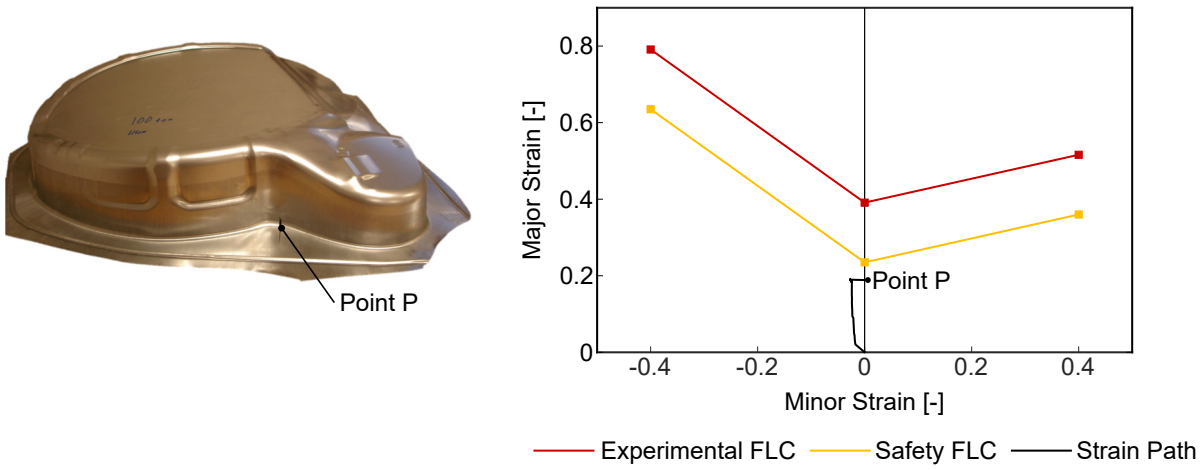

Figure 3.1: Car wheelhouse and corresponding load path of point P obtained by FE-simulation.

The validity of the failure predictions of current methodologies such as the enhanced Modified Maximum Force Criterion (eMMFC) by Hora and Tong (2008), the PEPS by Stoughton and Yoon (2012), the GFLC by Volk et al. (2012) or even damage models such as the Generalized Incremental Stress State Dependent Damage Model (GISSMO) (Neukamm et al., 2009, Andrade et al., 2016) or the Bao-Wierzbicki model (Bao and Wierzbicki, 2004) is not yet proven. Hence, there is a gap in research for a valid failure prediction for such complex load paths.

In addition to predicting failure at the macro level, an in-depth understanding of materials at the micro level is also needed. A deeper understanding of the micro-level processes involved in a change of loading direction is necessary to explain the measurable macro-level effects. The following points are addressed within the framework of this thesis:

- Determination of the influence of non-proportional load paths with a change of the loading direction on three different sheet materials
- Investigation of the processes at the microstructural level in order to generate a deeper understanding of the material behaviour
- Development of a methodology to predict failure after non-proportional load paths with a change of loading direction
- Implementation and validation of this methodology in a commercial FE software

In the context of this work, three different industrially relevant materials are examined in more detail. First, the effects that occur on a macro level are investigated through Nakajima and tensile tests with the pre-formed materials. The Nakajima tests allow conclusions about the formability, whereas the tensile tests allow conclusions to be drawn about the material characteristics, such as the onset of yielding or fracture elongation. In addition to the standardised method using Young's modulus, temperature-based methods are also used to determine the onset of yielding.

A time-synchronous recording of macroscopic and in-situ diffraction data allows a deeper insight into the behaviour of individual lattice planes and the dislocation densities when the loading direction is changed. Due to the time-synchronous recording, a correlation between the macroscopic and microscopic processes can be drawn. Further analysis of the microstructure is carried out employing nanoindentation. Here, individual grains and grain boundaries are indented, and their strength is determined by means of nanohardness. With the two methods mentioned, the microstructure is analysed down to the scale of individual grains, and thus, the cause of the material behaviour is investigated more closely. To visually depict any changes in the microstructure, the materials are examined using scanning electron microscopy (SEM). This should provide information on whether the pre-forming introduced has already led to visible changes or even damage in the microstructure. SEM is also used to analyse the fracture surfaces of the Nakajima tests. The fracture surfaces can provide a further indication of the mechanisms that ultimately led to the sample rupture. The analyses carried out should thus provide an understanding of the processes in the material, from the behaviour of individual grains to the final component.

3.2 Structure of the Work

After the basics and the state of the art have been explained in the previous chapters, the further structure of the work will be briefly discussed in this section and is also shown graphically in Figure 3.2.

Chapter 4 deals with the materials used and the sample geometries used in the further chapters for material characterisation. Here, the chemical composition, the microstructure, as well as existing phases and their distribution, are dealt with in more detail.

The experimental setups for the conducted experiments and the procedure for evaluating the data are discussed in Chapter 5. A further developed methodology is introduced to determine the forming limit for shear failure, where the classical approaches fail to determine the onset of necking. The focus of the microscopic experiments is on the evaluation of the synchrotron diffraction experiments and the application of temperature-based methods to determine the onset of yielding. For this purpose, the analysis of the peak profiles is explained in order to understand the development of the lattice strains and the determination of the dislocation density.

Chapter 6 describes the experimental results on a microscopic and macroscopic scale. Section 6.1 deals with the results of the initial material characterisation for the three examined materials. The influence of pre-forming on the macroscopic material behaviour in the tensile and Nakajima tests is presented in Section 6.2. The effects on the microscopic material behaviour are shown in Section 6.3, focusing on the synchrotron diffraction experiments. Also the results of the ex-situ nanoindentation experiments and the SEM images are shown.

The results obtained and presented are used to create a meta-model for predicting failure in deep-drawing operations where a change in loading direction occurs, see Chapter 7. Section 7.1 discusses and interprets the experimental results presented in Chapter 6. The development of the meta-model, its implementation into commercial FE software and its validation on an actual component are shown in Section 7.2.

At the end of the thesis, Chapter 8 briefly summarises the work and addresses further open research questions.

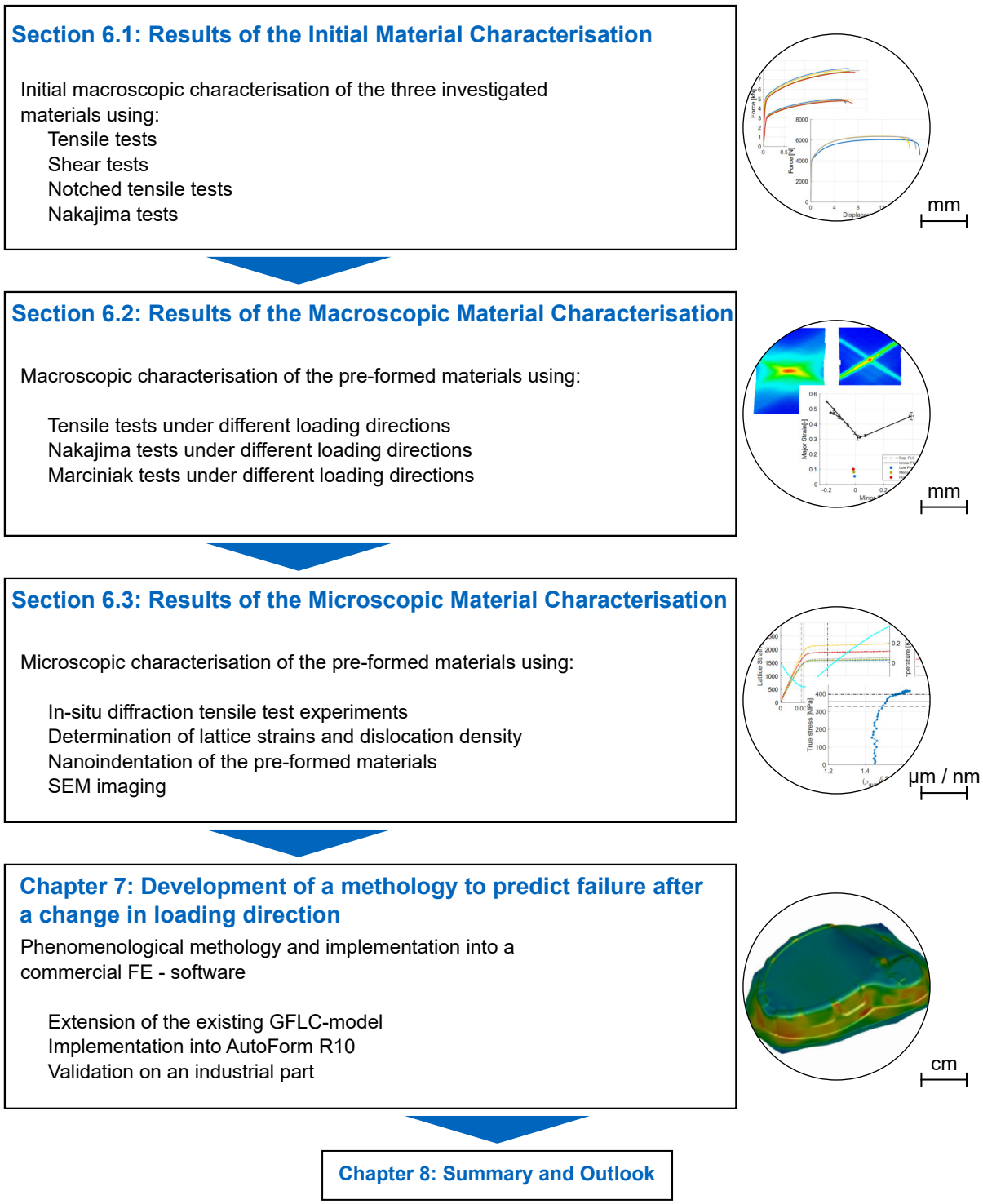

Figure 3.2: Structure of the thesis with the corresponding length scale of the investigations.

4 Materials and Specimen Geometry

This chapter describes the three sheet materials investigated and the specimen geometries used for the tests conducted in this study. The steel materials investigated are a micro-alloyed steel HC340LA and a dual-phase steel HCT590X according to DIN EN 10346 (2015) or CR330Y590-DP according to VDA 239-100. For the sake of simplicity, the material is further referred to as DP600. Next to the two steel grades, an aluminium alloy AA6016-T4 is also investigated. The materials differ significantly in their microstructure, strength and formability. All three materials are used in industry for different components and, therefore, also have industrial relevance. The initial thickness of the aluminium alloy AA6016-T4 and the HC340LA is 1 mm, while the dual-phase steel DP600 has an initial thickness of 0.8 mm.

4.1 Micro-alloyed Steel

Micro-alloyed steels have already been used in the automotive industry for some time (Pischinger and Seiffert, 2016, p.1169). The advantages of these steels are their high strength combined with good workability. The high strengths are achieved by adding titanium and/or niobium. The alloying elements lead to precipitation hardening and grain refinement (Birkert et al., 2013, p.33). Classic components made of micro-alloyed steels are crash-relevant structural parts such as pillars (thyssenkrupp Steel Europe AG, 2022).

HC340LA, which is investigated in this work, is characterised by a yield strength in the range of 340-420 MPa and a tensile strength of 410-510 MPa with a minimum fracture elongation of 21 % according to the DIN EN 10268 (2013). Due to grain refinement to increase strength, the steel has a fine structure with a grain size of approx. 5-10 µm. This small grain size is advantageous for the synchrotron experiments carried out. The microstructure of this steel grade consists of a purely ferritic matrix with small, round cementite inclusions (black dots), see Figure 4.1. In Figure 4.1 (c), the big black dots are non-metallic inclusions like manganese sulfide (MnS). MnS is known to reduce the formability as the inclusions are elongated in RD. A tensile test in TD shows a reduced fracture elongation compared to the results from RD (Wu et al., 2019).

The chemical composition of the material and the specifications according to the standard are listed in Table 4.1.

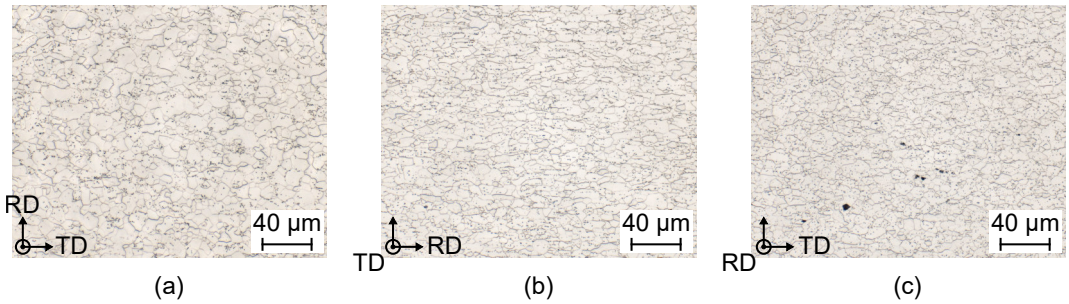

Figure 4.1: Microstructure of the micro-alloyed HC340LA steel from top view (a), side view (b) and cross-section (c).

Table 4.1: Chemical composition in percent of the HC340LA steel according to DIN EN 10268 and measured values.

-	C	Si	Mn	P	S	Al	Ti	Nb
DIN EN 10268	max. 0.12	max. 0.5	max. 1.5	max. 0.03	max. 0.025	min. 0.015	max. 0.15	max. 0.09
Measured	0.05	0.01	0.43	0.009	0.006	0.057	0.001	0.02

4.2 Dual-phase Steel

Dual-phase steels, also known as DP steels, are a type of steel developed to improve the performance of traditional steel materials. Such steels get their strength from the presence of two distinct phases in their microstructure. A soft ferrite matrix and hard martensite islands. This makes them highly formable and exhibit excellent strength and toughness properties. Tensile strengths range from 600 MPa to 1200 MPa, depending on the martensite content. However, a higher martensite content also means lower formability (Birkert et al., 2013, p. 34). A special heat treatment adjusts the microstructure. The steel is cooled quickly after annealing, and martensite is formed (Pischinger and Seiffert, 2016, p.1170-1172). Dual-phase steels are used for pillar reinforcements, crash structures and seat structures (Tata Steel Europe Limited, 2016).

The chemical composition is summarised and compared to DIN EN 10346 (2015) in Table 4.2, and the microstructure is shown in Figure 4.2. Here, the investigated steel CR330Y590-DP or DP600 has a fine microstructure in which the martensite islands are homogeneously distributed from the top view. Still, they show a banded appearance in RD, which is common for dual-phase steels, see Figure 4.2 (b). These banded structures also lead to an increased strength and reduced formability when the material is tested in the TD.

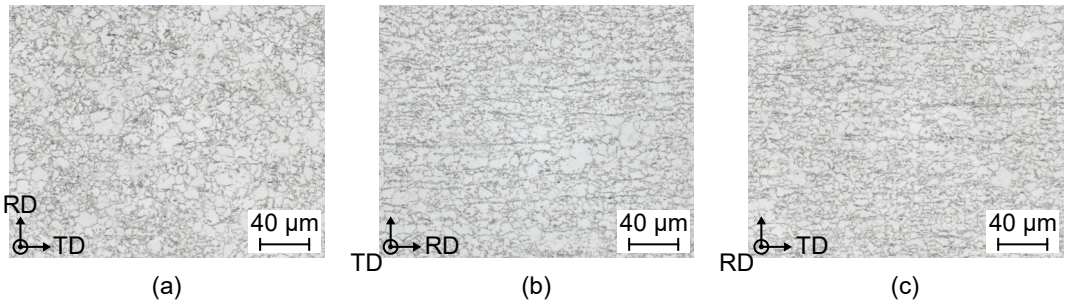

Figure 4.2: Microstructure of the dual-phase steel CR330Y590-DP (DP600) from top view (a), side view (b) and cross-section (c).

The strength class of the investigated dual-phase steel is at the lower end of the strength scale for such steels in order to have sufficient ductility. It is required to allow different pre-forming levels with a sufficiently large difference between the pre-forming levels which are set based on the linear FLC. According to DIN EN 10346 (2015), the DP600 has a yield strength of 330-430 MPa and a tensile strength of at least 590 MPa. The fracture elongation must be higher than 20 %.

Table 4.2: Chemical composition in percent of the DP600 steel according to DIN EN 10346 and measured values.

-	C	Si	Mn	P	S	Al	Cr + Mo	Nb + Ti
DIN EN 10346	max. 0.15	max. 0.75	max. 2.5	max. 0.04	max. 0.015	0.015-1.5	max. 1.4	max. 0.15
Measured	0.16	0.59	1.39	0.013	0.001	0.388	0.025	0.006

4.3 Aluminium Alloy

In addition to the two types of steel, an aluminium alloy is also being investigated. Compared to steels, aluminium has the advantage of being significantly less dense and therefore allows for weight savings (Ostermann, 2014, p.10-12). The alloy investigated in this thesis is an age-hardenable AlSi1.2Mg0.4 alloy. It is further designated as AA6016-T4. The heat treatment condition is T4, which means that the material is solution annealed and cold aged. this condition is the most commonly used heat treatment state in industrial applications (Birkert et al., 2013, p.39). Due to the heat treatment process, the properties of the material can change over time. According to Cuniberti et al. (2010), the strength and formability change rapidly after heat treatment. The strength increases while the formability decreases. Only minor changes occur after 45 days when stored at room temperature. The change in the material behaviour is due

to alloying elements, which are in a solid solution after quenching. This state is not a stable thermodynamic equilibrium state. The solute atoms, therefore, tend to form clusters. These clusters form so-called Guinier-Preston zones or nano-sized precipitates, thus strengthening the alloy (Kuwabara et al., 2017). To avoid any influence of the ageing process, the heat treatment of the material happened two years ago. Therefore, no changes in the properties occurred during the experiments with this material caused by ageing.

In contrast to the two steels examined, the aluminium alloy has an *fcc*-lattice structure. On the other hand, the steels have a *bcc*-lattice structure. Typical applications are as outer and inner body panels in vehicle construction (Ostermann, 2014, p.524). The AA6016-T4 alloy is preferred for outer body panels due to its good surface properties (Poznak et al., 2018).

This alloy has a yield strength between 80-140 MPa, a tensile strength in the 170-250 MPa range, and a minimum elongation at fracture of 24 %.

This material has the largest grains of the three examined. These are in the range of approx. 40 µm, see Figure 4.3. The material has numerous precipitates, e.g. Mg_2Si, which are clearly visible in the micrograph. The homogenous microstructure and the precipitates are caused by a heat-treatment after rolling. The chemical composition in comparison to the DIN EN 573-3 (2022) can be found in Table 4.3.

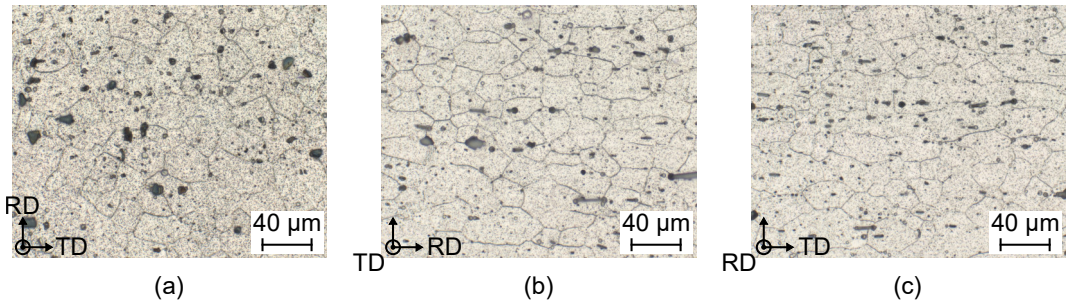

Figure 4.3: Microstructure of the aluminium alloy AA6016-T4 from top view (a), side view (b) and cross-section (c).

Table 4.3: Chemical composition in percent of the AA6016-T4 according to DIN EN 573-3 and measured values.

-	Si	Fe	Cu	Mn	Mg	Cr	Zn	Ti
DIN EN 573-3	1.0-1.5	max. 0.5	max. 0.2	max. 0.2	0.25-0.6	max. 0.1	max. 0.2	max. 0.15
Measured	1.32	0.24	0.085	0.13	0.38	0.019	0.016	0.022

4.4 Specimen Geometries

Tensile tests, shear tensile tests, notched tensile tests and bulge tests are carried out for the initial material characterisation. These tests cover a wide range of stress states, thus enabling an accurate description of the yield locus. Figure 4.4 shows the used samples. The geometry of the tensile specimens for the initial material characterisation and those for the pre-formed material tests are identical and standardised in DIN 50125 (2022).

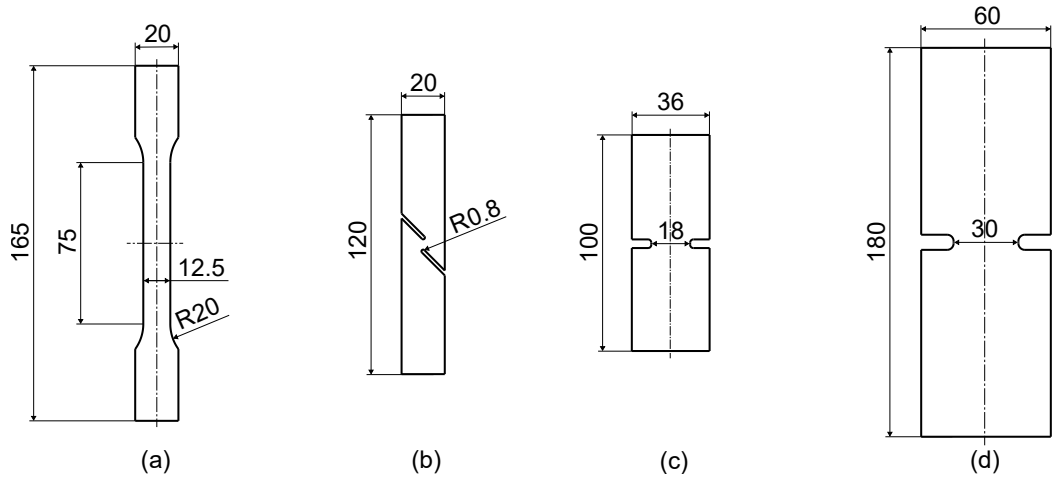

Figure 4.4: Used specimen geometries for the tensile tests (a), the shear tests (b) and notched specimens with different notch widths of 18 mm (c) and 30 mm (d).

The two different notched specimen geometries and the shear specimens are used for an inverse calibration of the yield locus in the plane-strain area. The stress-strain curves are obtained for five different directions, 0°, 22.5°, 45°, 67.5° and 90° with respect to RD. The yield locus is optimized to match the resulting engineering stress-strain curve from the FE-simulation and the experiments.

To determine the formability, nine different sample geometries are used for the initial Nakajima tests. These differ from each other in their bridge width. The bridge width is varied from 30 mm to the full sample, some selected geometries can be seen in Figure 4.5. The amount of different geometries is based on the requirements for the GFLC-model where nine different points of the linear FLC are used.

For the non-proportional load paths, four different bridge widths (30 mm, 100 mm, 130 mm and the full sample) are investigated for the post-forming. These four different geometries cover a wide range of strain states and are a good compromise between the need of a sufficient analyse of the formability after pre-forming and the experimental effort.

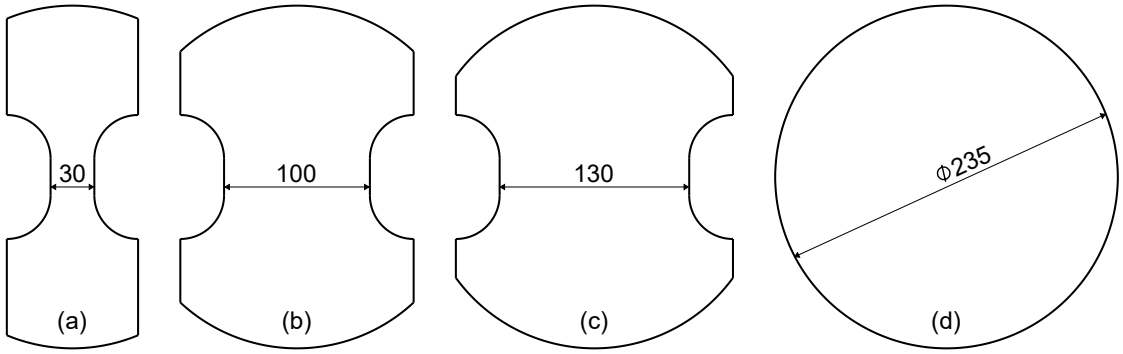

Figure 4.5: Used Nakajima specimen geometries with different bridge widths of 30 mm (a), 100 mm (b), 130 mm (c) and the full specimen (d).

The samples for the pre-forming are shown in Figure 4.6 (a). The specimen geometry is optimised depending on the material to obtain a homogeneous strain distribution in the center of the specimen. The homogeneously pre-formed area has a diameter of approximately 100 mm, see red circle in Figure 4.6 (b). To achieve a change in loading direction, the geometry is rotated and cut from the pre-formed specimens, see Figure 4.6 (b). The cutting process for the Nakajima specimens was done by laser cutting. For the tensile tests, the specimen blanks were cut out and further processed into tensile specimens by milling to avoid any influence of the manufacturing process on the mechanical parameters. Due to the size of the Nakajima specimen, only one sample can be cut from one pre-formed specimen, while for the tensile tests, up to five specimens can be cut out from a single pre-formed specimen.

The specimens are designated according to the direction of initial pre-forming (IF) as well as the direction of post-forming (PF). For example, specimens without a change in the loading direction are designated IF0-PF0 and specimens with a change in the loading direction of 90° are designated IF0-PF90, see also Figure 4.6 (b).

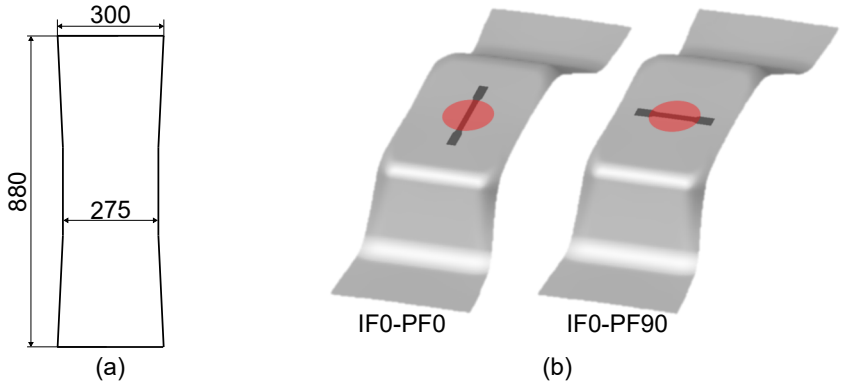

Figure 4.6: Used specimen for the uniaxial pre-forming (a) and the rotation process of the specimens (b).

5 Experimental Setup and Evaluation

Chapter 5 will give an overview of the equipment used for the experiments and the evaluation methods. The focus is hereby on the microscopic experiments using synchrotron diffraction, but also a novel evaluation method for the determination of FLCs with shear failure is presented.

5.1 Macroscopic Experiments

5.1.1 Testing Equipment for the Macroscopic Experiments

The conduction of the macroscopic experiments is done on a uniaxial tension testing machine ZwickRoell Z150. An optical laserextensometer with a gauge length of 50 mm is used for the strain measurement in the tensile test. The load cell allows a maximum force of 150 kN. A constant strain rate of 0.004 1/s is applied for the macroscopic tensile test experiments.

All Nakajima and Marciniak experiments are conducted on a sheet metal testing machine BUP1000 from ZwickRoell. This machine has a maximum blank holder force and punch force of 1000 kN and allows punch speeds between 0.05 and 50 mm/s. The clamping force in the experiments is set to 400 kN, sufficient for all materials to prevent any movement of the investigated sheet materials. The punch speed is set to 1 mm/s which is in accordance with DIN EN ISO 12004-2 (2021). A DIC-system Aramis4M by GOM mbH is used to measure the occurring strains with a frame rate of 10 Hz.

The pre-forming operations are performed on a double-acting hydraulic press DXU 320 B from Dieffenbacher GmbH & Co. This press has a maximum punch force of 3500 kN and a maximum die cushion force of 1250 kN. The die cushion force is needed to clamp the material and suppress any movement of the blank. A mounting plate size of 1600 mm x 1300 mm allows the use of the modified Marciniak tool presented in Figure 2.25, which is used in this work for the pre-forming of the specimens.

5.1.2 Nakajima Experiments

Evaluation of the Forming Limit Curve

The determination of the formability is done by the TDEM, as described in Section 2.1.2. A PVC pad with applied lubricant is used to reduce the friction between the punch and the specimen. To be able to use this method, there must be a failure due to localized necking. A thickness reduction characterizes localized necking. The thickness reduction rate $\dot{\varepsilon_3}$ increases after the onset of necking. This methodology cannot evaluate a brittle fracture or a shear fracture with no or only a small increase in thickness reduction rate. They lead to values that over- or underestimate formability. For example, during shear failure no constant increase in thickness reduction is detectable, see Section 2.3. Nevertheless, a strong increase in the major strain is observed during the shear deformation. For the modified TDEM, the major strain ε_1 is applied instead of the thickness reduction rate $\dot{\varepsilon_3}$. The localized necking is not determined by the intersection point but by the angle bisector of the two straight lines, see Figure 5.1.

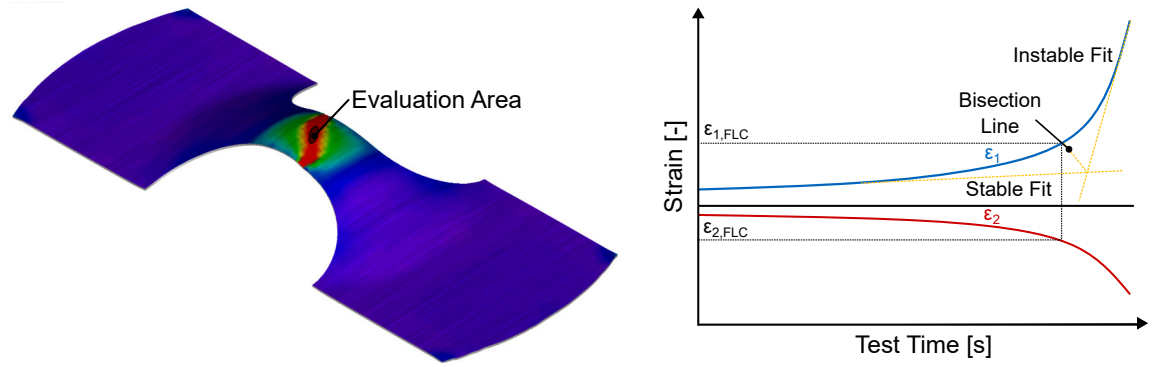

Figure 5.1: Exemplary determination of the major- and minor strain at the onset of necking using the modified TDEM.

Using the major strain, the forambility of samples showing shear failure can also be evaluated. Therefore, for the determination of specimens showing a localised necking behaviour, the classical TDEM is applied. To detect specimens with a shear failure, the thickness reduction rate $\dot{\varepsilon_3}$ is examined closer. When $\dot{\varepsilon_3}$ shows no constant increase or even a decrease in $\dot{\varepsilon_3}$, shear failure occurs.

5.2 Microscopic Experiments

5.2.1 Setup of the In-situ Synchrotron Diffraction Experiments

The synchrotron experiments in this thesis were carried out at the Deutsche Elektronen Synchrotron (DESY) in Hamburg. Using a single bounce monochromator, the synchrotron radiation was adjusted to a wavelength of 0.14235 Å. In order to radiate a sufficient number of grains, the beam cross-section is set to 0.7 x 0.7 mm^2. The diffracted beam is measured using a Perkin Elmer XRD 1621 flat panel detector. This detector has 2048 x 2048 pixels with a pixel size of 200 x 200 μm^2. The detector is operated with a recording frequency of 1 Hz. A tensile testing machine was mounted between the radiation source and the detector in which the tensile tests were carried out. For this purpose, the sample is firmly clamped and deformed at a constant strain rate of 0.00015 1/s. The test rig is moved downwards at half the testing speed to measure the same area throughout the experiment. The occurring strains are measured by means of a strain gauge on the sample. In addition, the temperature of the sample is measured by using a PT1000 temperature sensor and the force is recorded by a permanently installed load cell with a maximum force of 50 kN. These data are recorded synchronised with 10 Hz and are triggered to the diffraction measurements. Figure 5.2 shows a schematic illustration of the experimental setup. This setup has already been used in prior studies of Vitzthum et al. (2022a) and Vitzthum et al. (2022b).

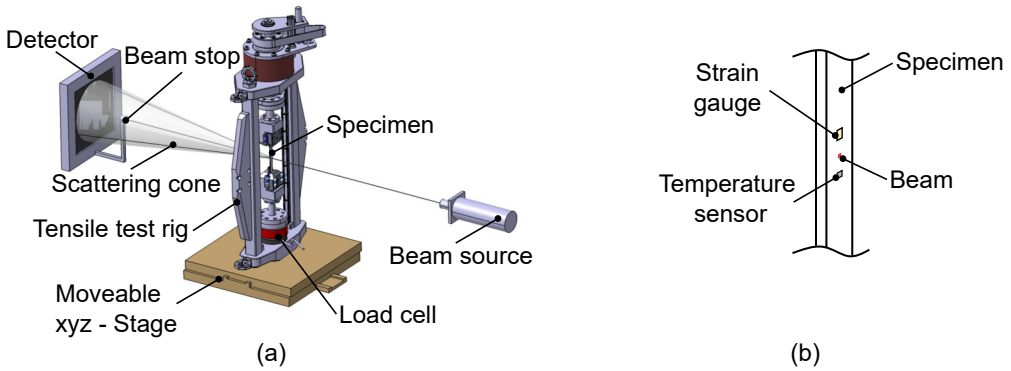

Figure 5.2: The used experimental setup for the synchrotron diffraction experiments (a) and a closer look at the placement of the strain gauge, temperature sensor and beam (b).

The detector distance and the instrumental resolution are determined by using LaB_6 with a thickness of 1 mm.

5.2.2 Evaluation Methods of the In-situ Synchrotron Diffraction Experiments

Determination of the Onset of Yielding

Microscopic synchrotron results and macroscopic results are correlated for the evaluation of the synchrotron experiments. First, the evaluation of the macroscopic experiments is discussed in more detail. The evaluation of the macroscopic tests focuses on determining the yield strength through the temperature signal. For this purpose, the temperature signal is examined more closely. External influences are minimised by keeping the ambient temperature constant. In the elastic range, a cooling of the sample can be observed, as described in the literature. With the onset of plastification, the sample heats up, and an increase in temperature is detected.

The temperature minimum as the onset of yielding is also evaluated and is delivers the parameter YS_{Tmin}. Another methodology is the determination of the onset of yield according to Vitzthum et al. (2022a). The onset of yielding is now determined as the deviation of the temperature signal from the linear decrease. For this purpose, the first derivative of the temperature signal is assessed. The zero crossing of the derivative represents the temperature minimum. Two straight line fits are performed, one in the area of the linear temperature decrease (green area in Figure 5.3 (b)), where the first derivative is almost straight and around the zero crossing of the first derivative (blue area in Figure 5.3 (b)). An angle bisector determines the beginning of the plastic deformation through the intersection of the two linear curves. This procedure provides the parameter YS_0. The temperature-based methods are compared with the classical $YS_{0.2\%}$ method according to DIN EN ISO 6892-1 (2020). Figure 5.3 shows a visual description of the two temperature-based evaluation methods for the example of the HC340LA steel.

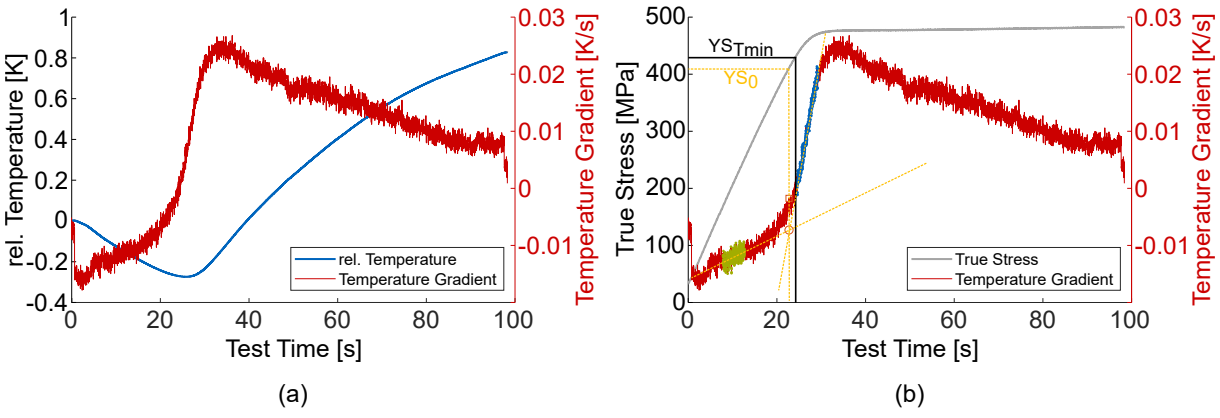

Figure 5.3: Temperature signal and the first derivative (a) and the evaluation process of YS_0 (b).

Peak Profile Analysis

The results of the macroscopic investigations concerning the yield strength are combined with the microscopic results of the diffraction experiments. The diffraction patterns are evaluated using the Fit2D software developed by Hammersley (2016). In order to obtain results in the longitudinal direction, parallel to the tensile direction, and the transversal direction, two sectors with a width of ± 10° are chosen. The intensities occurring in these areas are summed to give a 2-D peak profile. The obtained peak profiles were transferred to the AFit software developed by Staron (2009) for further evaluation. An exemplary diffraction pattern for a ferritic steel and the corresponding peak profile for a *bcc*- and *fcc*-material are shown in Figure 5.4.

For the *bcc*-materials such as the HC340LA steel and the DP600 steel, the peaks corresponding to the (110), (200), (211), (220), and (310) lattice planes are evaluated, see Figure 5.4 (b). While for the *fcc*-material such as the AA6016-T4, the peaks corresponding to the (111), (200), (220), (311), (222), and (400) lattice planes are evaluated, see Figure 5.4 (c).

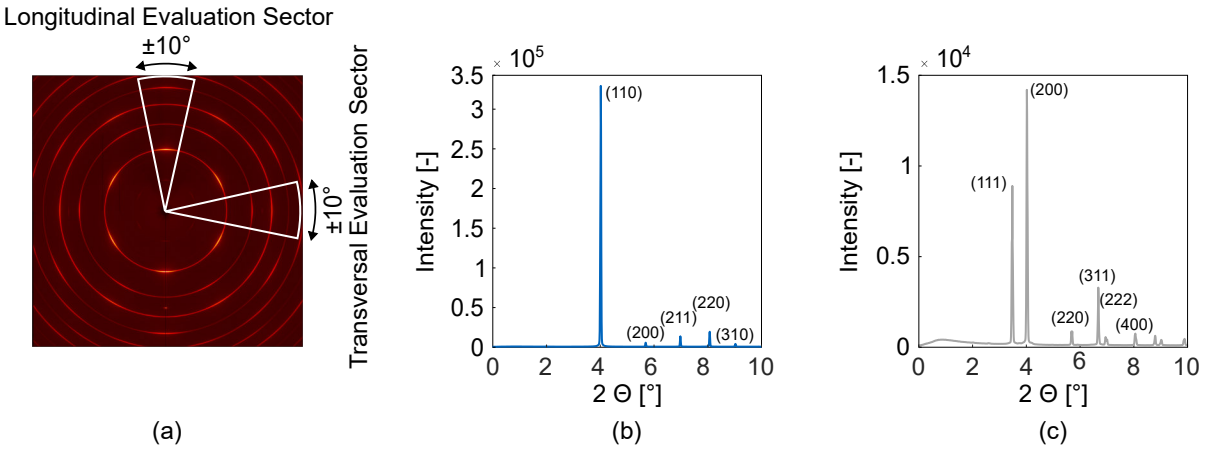

Figure 5.4: Debye-Scherrer rings of a steel and the two evaluation cones (a), resulting 2D peak profile for a bcc-material and the evaluated lattice planes (b) and the resulting peak profile for a fcc-material and the evaluated lattice planes (c).

A Gaussian function is used to mathematically describe the peaks and the change of the position of the maximal intensity, see Figure 5.5 (a). This simple function is sufficient because in these experiments, there is no change in the microstructure due to grain refinement or phase transformation (Strunz et al. (2001)).

Determination of Lattice Strains

During the experiment, the peak profiles of the material change, see Figure 5.5 (b). On the one hand, the position of the maximum of the individual peaks changes due to the load on the sample and the resulting change in lattice spacing. On the other hand, the shape of the peaks changes, which results in a broadening of the peaks. For the longitudinal direction the peak is shifted towards higher peak positions as the atomic distance is increased, while for the transverse direction the peak is shifted towards lower peak positions as the atomic distance is reduced in the tensile test, see Figure 5.5 (b).

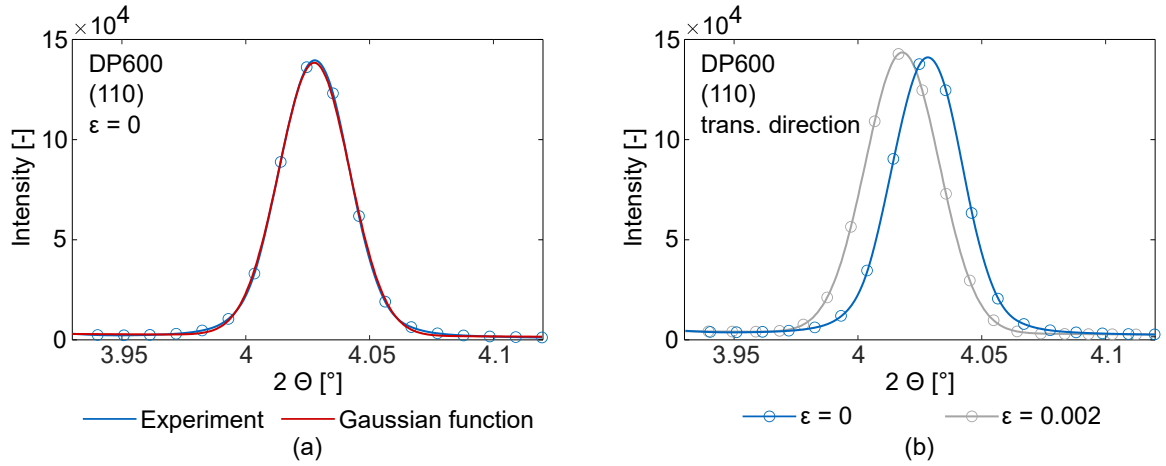

Figure 5.5: Comparison of the experimental peak shape and the Gaussian function (a), peak shift and peak broadening for an DP600 in transversal direction at an elongation of $\varepsilon = 0.002$ (b).

The lattice strains are calculated using the atomic spacing d_{hkl}, which is calculated using the Bragg equation or the radial maximum peak position Θ (Schuren and Miller, 2011). Changes in the atomic spacing that occur during the tensile test make it possible to calculate the specific lattice strain ε_{hkl}, see equation (5.1). However, the strains determined based on the atomic spacing or the radial position only allow the elastic strains to be considered. As soon as the plastification of the lattice plane takes place, no further increase in the lattice strain is observed (Wang et al., 2012).

$$\varepsilon_{hkl} = \frac{d_{hkl} - d^0_{hkl}}{d^0_{hkl}} = \frac{sin(\Theta^0_{hkl})}{sin(\Theta_{hkl})} - 1 \quad , \tag{5.1}$$

where d^0_{hkl} and Θ^0_{hkl} is the initial, stress-free plane spacing and radial maximum peak position, respectively.

Determination of Dislocation Densities

The change of the peak shape, particularly the broadening of the peak, allows the determination of dislocation densities in the material. To determine the dislocation density, the Williamson-Hall plot (Williamson and Hall, 1953) and the Williamson-Smallman dislocation model (Williamson and Smallman, 1956) is used. Peak broadening can be evaluated using the FWHM or IB (Ungár et al., 1998). The total peak broadening β_{exp} can be written as the sum of the contributions of the crystallite size β_{size}, the strain β_{strain} and the instrumental setup β_{ins}, see equation (5.2) (Madhavi, 2019).

$$\beta_{exp}^2 = \beta_{size}^2 + \beta_{strain}^2 + \beta_{ins}^2 \tag{5.2}$$

The influence of the setup is determined using lanthanum hexaboride (LaB_6) as a reference material. Because LaB_6 in powder form theoretically has an ideal peak profile, the influence of the instrumental setup can be removed by subtracting the peak profile of the material and the peak profile of LaB_6 according to equation (5.3) (Biju et al., 2008).

$$\beta_{corr} = \sqrt{\beta_{exp}^2 - \beta_{ins}^2} \quad , \tag{5.3}$$

where β_{corr} is the corrected width. According to this model, the peak broadening is due to the crystallite size D and the occurring strain (Bindu and Thomas, 2014). The expression of the Williamson-Hall method is the following in the reciprocal space

$$\beta_{corr}(d^*) = 2 \cdot e \cdot d^* + \frac{1}{D} \quad . \tag{5.4}$$

To transfer this equation in real space, the following equations must be applied according to Mittemeijer and Welzel (2008): $\beta_{corr}^* = \beta \cdot cos(\theta) \cdot \lambda^{-1}$ and $d^* = 2 \cdot sin(\theta) \cdot \lambda^{-1}$. With the relationship between the root mean square strain $\langle \epsilon^2 \rangle$ (RMS) and the microstrain e according to equation (5.5), the RMS can be calculated, see Delhez et al. (1982):

$$\langle \epsilon^2 \rangle^{1/2} = \left(\frac{2}{\pi} \right)^{1/2} * e \quad . \tag{5.5}$$

Substituting equation 5.4 leads to the following equation for the Williamson-Hall model in real space,

$$(\beta \cdot cos(\theta))^2 = 8\pi \cdot \langle \epsilon^2 \rangle \cdot sin(\theta))^2 + \frac{\lambda^2}{D^2} \quad , \tag{5.6}$$

where θ is the Bragg angle, λ the wave length and D the crystallite size. The Williamson-Hall method, according to Williamson and Hall (1953), is used to separate the change in shape from other material-specific influencing factors. This method is able to separate effects caused by size effects from those caused by lattice strain. For this purpose, $\beta \cos(\theta)^2$ versus $\sin(\theta)^2$ is plotted, see Figure 5.6. The crystallite size determines the zero crossing, while RMS corresponds to the slope of the fitted straight line. When the intercept is close to zero for each diffraction image, peak broadening is caused by lattice strain, and crystallite effects can be neglected (Christien et al., 2015). Figure 5.6 also shows that the line broadening does not increase monotonously for all lattice planes and that the deviation increases with increasing strain. The offset from linearity is called strain anisotropy. Strain anisotropy is caused mainly by dislocations and lattice defects similar to dislocations (Ungár, 2008). Summarised, the fitted linear curve passes approximately through the origin, and the offset from linearity is neglectable. Therefore, no size effects occur in the investigated material.

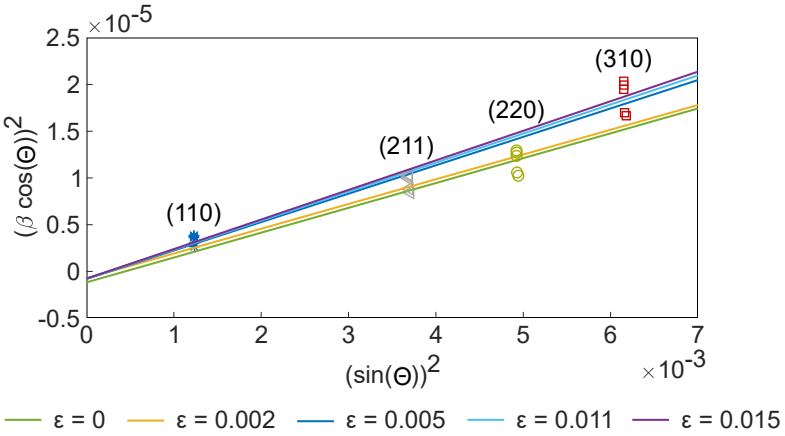

Figure 5.6: Williamson-Hall plot of a HC340LA steel at different stages of the experiment.

Using equation 5.7, where K has a constant value of $K = 14.4$ for *bcc*-materials (Wilson, 1949) and $K = 16.1$ for *fcc*-materials (Miyajima et al., 2014), b is the Burgers vector and D is the coherent domain size, the dislocation density ρ is calculated. Since it is assumed that there are no size effects in the material, the value of D is set to 1 (Williamson and Smallman, 1956).

$$\rho = \frac{K^2 * \langle \epsilon^2 \rangle}{D * b^2} \tag{5.7}$$

The Burgers vector is dependent on the lattice structure of the investigated material. For *bcc*-materials, the burgers vector is calculated using the lattice constant and the slip direction $\langle 111 \rangle$ while the *fcc*-materials the slip direction $\langle 110 \rangle$ is used. The Williamson-Smallman model is quite a simple model. Nevertheless, it allows a first estimation of the dislocation density. Since in this work, mainly the qualitative comparisons are shown, this model is sufficient.

Determination of the Texture

Synchrotron diffraction is also used to determine the texture. For this purpose, a sample consisting of three layers of the material is glued together, see Figure 5.7. The adhesive does not cause any diffraction of the beam and is invisible in the diffraction pattern. The measurement is made in 5° steps from -180° to 180°.

The lattice planes (110), (200) and (211) are examined for the *bcc*-materials and the lattice planes (111), (200), and (220) for the *fcc*-materials. The ODF can be calculated from the three mentioned grid planes using the ATEX software by Beausir and Fundenberger (2016).

The materials are examined at different strain states to measure the influence of plastic deformation. In addition to the initial material, the deformed state is also examined. On the one hand, at ε = 10 % uniaxial pre-forming, on the other hand, at the uniform elongation in the tensile test after a uniaxial pre-forming of ε = 10 % for specimens without a change in the direction (IF0-PF0) and for specimens with a change in the loading direction of 90° (IF0-PF90). The specimens were therefore re-loaded on a Zwick Z150 tensile test machine which was also used for the macroscopic experiments. After reaching the uniform elongation, the specimens were unloaded and prepared according to Figure 5.7.

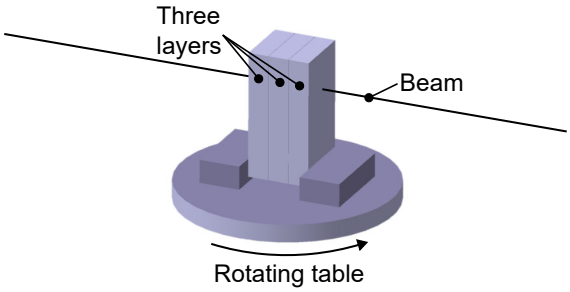

Figure 5.7: Texture measurement specimen and rotating table.

5.2.3 EBSD Experiments

The dislocation density for the HC340LA is also examined by EBSD. The microstructure of the material is scanned using a JEOL JSM-7600 SEM. A acceleration voltage of 20 kV, a working distance of 20 mm and a step size of 0.12 μm is applied. A magnification factor of 2000 is used. This magnification factor allows the examination of a sufficient number of grains in one image. The evaluation of the dislocation density is done by the software ATEX. This software is also used for the texture analysis. A maximal misorientation angle of 5° and a burgers vector of 2.8665 Å is set.

The different strain states examined and the experimental setup are the same as for the texture analysis. Therefore, the initial state, the ε = 10 % uniaxial pre-formed state and at the time of the maximum force in the tensile tests for the IF0-PF0 and IF0-PF90 specimens.

As mentioned in section 2.3.1, only the GNDs can be visualised by EBSD. But, in comparison to the synchrotron experiments, a smaller area in the size of approximately 50 x 50 μm^2. This allows a more precise evaulation of dislocation structures and the distribution of the dislocations. Such an evaluation is not possible by synchrotron diffraction.

5.2.4 Nanoindentation Experiments

The nanoindentation experiments are carried out on a NanoTest vantage machine by Micro Materials. A spherical diamond indenter with a radius of 5.8 μm is used. The use of a spherical indenter instead of a Berkovich intender is done due to the fact, that the strains and stresses increase with increasing depth of the indentation. This is not the case for the Berkovich indenter, see Seok et al. (2014). A maximum force of 25 mN at a constant rate of 0.5 mN/s is applied. The nano hardness is calculated by equation 5.8,

$$H = \frac{P}{A_c} \quad , \tag{5.8}$$

where P is the load and A_c the contact area. A_c is calculated by equation 5.9, with R being the indenter radius and h_c the indentation depth:

$$A_c = 2 \cdot \pi \cdot R \cdot h_c \quad . \tag{5.9}$$

To ensure a smooth surface to be tested and to enable the evaluation of the indentation area, the material is polished and etched. For the steel samples, Nital is used for etching, and for the aluminium samples NaOH with a concentration of 1 %.

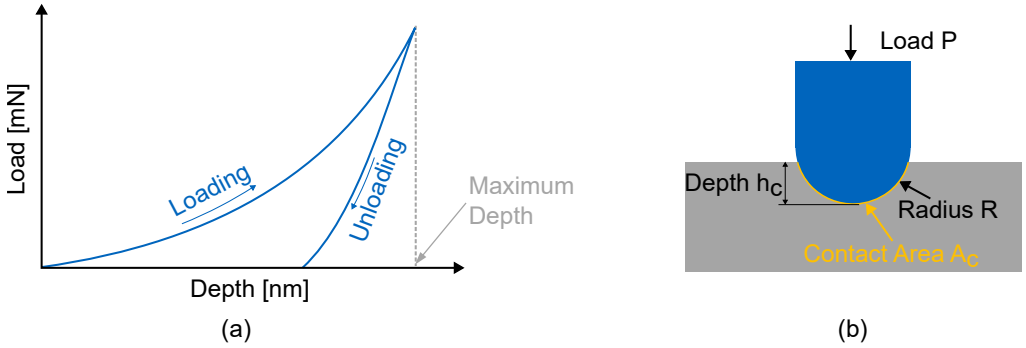

Figure 5.8: Force-Displacement curve for a nanoindentation experiment during loading and unloading (a) and parameters for the evaluation process (b).

6 Results

Chapter 6 presents the results of the work. First, the differences between the three investigated materials in the initial state are discussed. Then the results of the macroscopic tests with non-proportional load paths are presented. The focus of the macroscopic results here is on the results of the tensile and Nakajima tests. The microscopic investigations using synchrotron diffraction, nanoindentation and SEM images are considered in the final section of Chapter 6.

6.1 Initial Material Characterisation

In the context of this thesis, three different materials are examined, see chapter 4. These three materials differ very clearly in their microstructure. In order to determine the different properties of the materials in the initial state, the flow curve in RD, the Lankford coefficients (r-Values) for the determination of the anisotropy and the yield locus. The corresponding results are presented in Figure 6.1.

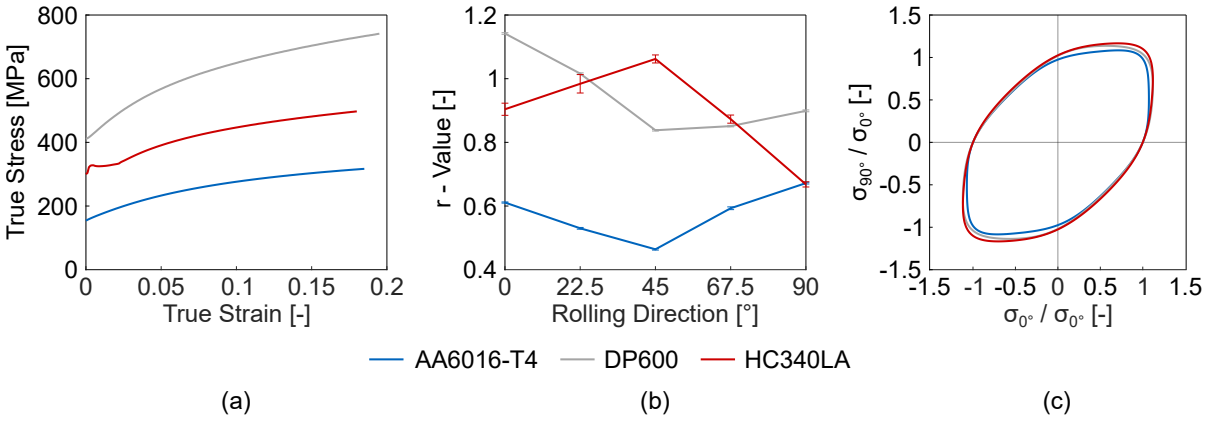

Figure 6.1: Flow curves in RD (a), Lankford coefficients (b) and yield loci (c) for the three examined materials in the as-received state.

The three materials have different strength levels in their initial state. In contrast to the aluminium A6016-T4 and the DP600 steel, the HC340LA steel has a pronounced yield strength. The flow curves are cropped at the time of the uniform elongation. The uniform elongation is almost identical for the three materials. Concerning anisotropy, the materials show only a low degree of anisotropy. The low anisotropy is also reflected in the yield locus. The area of the yield locus curve in the plane-strain region was determined by inverse optimisation. For this purpose, the

notched tensile specimens are taken into account. The yield loci curves were adjusted so that the force-displacement curves of the FEM simulations and the force-displacement curves of the experiments overlap as well as possible.

To determine the formability, Nakajima tests are carried out. Since the influence of a change in the loading direction is analysed in the further course, the FLCs are recorded at 0°, 45° and 90° to the RD. This allows conclusions to be drawn as to whether the material already has a dependence of the loading direction in the as-received state. The FLCs determined by the TDEM are shown in Figure 6.2.

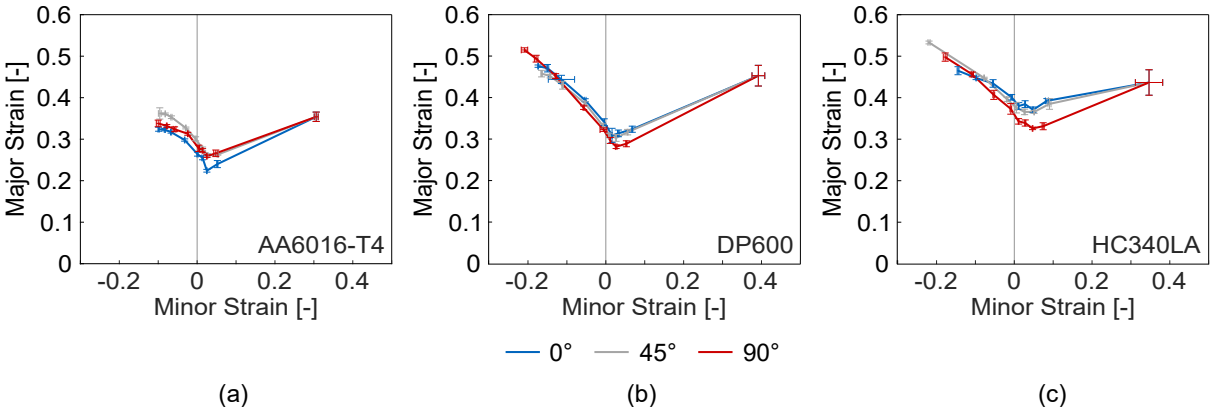

Figure 6.2: FLCs for AA6016-T4 (a), DP600 (b) and HC340LA (c) in the as-received state.

Of the three investigated materials, the aluminium alloy AA6016-T4 shows the lowest formability. While the steels show the lowest formability under 90° to RD, the aluminium has the lowest formability under 0° to RD. This effect is known and is also taken into account in the standard DIN EN ISO 12004-2 (2021) where aluminium alloys have to be tested under 0° to RD and steels under 90° to RD. In general, the three materials are only marginally influenced by the loading direction. Based on the FLCs of the initial material, the pre-forming levels for the subsequent non-proportional experiments are selected. Three different pre-forming levels are chosen for each material used in the consecutive Nakajima experiments. For the consecutive tensile tests, six different pre-forming levels are chosen.

6.2 Macroscopic Experiments

6.2.1 Pre-forming States

Previous studies by Volk et al. (2020b) have shown that the influence of the loading direction is also dependent on the pre-forming stress state. The influence is particularly large, especially on the left side of the FLC. The pre-formings in the context of this work refer to uniaxial pre-forming states.

The pre-forming levels are set to be approximately 25 %, 35 % and 50 % of the linear FLC under 0° to the RD for the Nakajima experiments. The three pre-forming levels allow a detailed consideration of the pre-forming level from which changes in the direction of loading influence the formability. The pre-forming level is measured using a GOM Argus optical measuring system. A grid size of 2 mm is sufficient to determine the plastic strains. The homogeneity of the pre-forming is shown for three different levels of uniaxial pre-forming in Figure 6.3. Even for pre-forming levels above the uniform elongation, the experimental setup can achieve a homogeneously pre-formed area, see Figure 6.3.

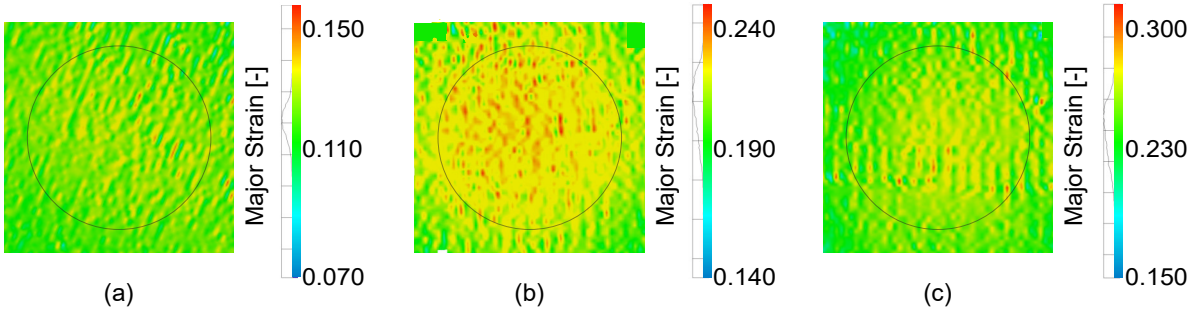

Figure 6.3: Major strain distribution after uniaxial pre-forming for the pre-forming levels 25 % (a), 35 % (b) and 50 % (c) of the DP600 steel.

The circle represents the area of homogeneous pre-forming and has a diameter of 100 mm. All uniaxial pre-forming levels for the three investigated materials can be seen in Figure 6.4. The pre-forming states are compared to the initial FLC in RD as all pre-formings are done under 0° with respect to RD.

As the experimental FLC obtained by Nakajima experiments show a non-proportional load path, the FLCs are corrected by using the method of Volk and Gaber (2017). The non-proportionality is caused by a biaxial pre-forming due to the use of a hemispherical punch at the beginning of the experiment and a shift towards the plane-strain state during necking. Therefore, the effect on the FLCs is more pronounced on the left-hand side of the FLCs where the occuring strain

path influences the remaining formability the most. The resulting linearised FLCs are depicted as *Linear FLC* in Figure 6.4 and Figure 6.5. In the further course of this thesis, the results of the non-proportional load paths will be compared to the linearised FLC.

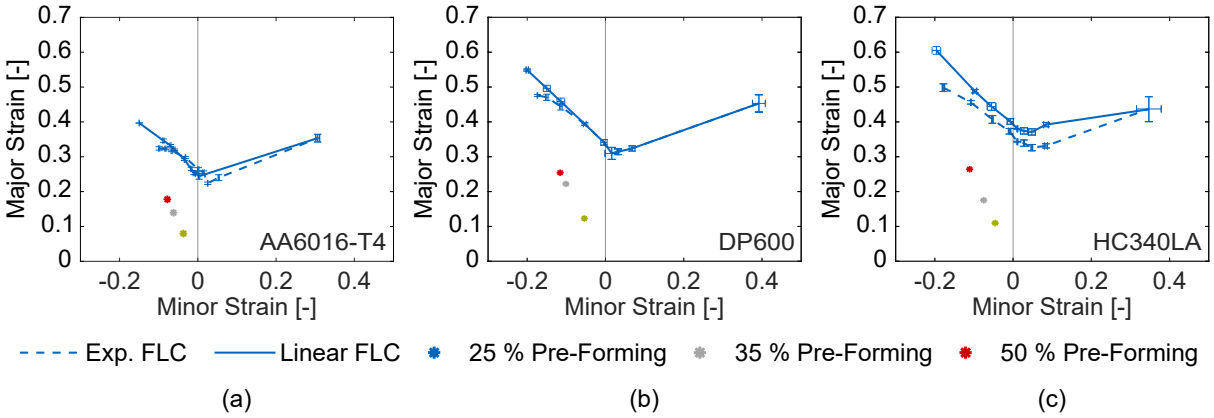

Figure 6.4: Pre-forming levels for AA6016-T4 (a), DP600 (b) and HC340LA (c) used in the consecutive Nakajima experiments.

For the tensile tests with pre-formed material, lower pre-forming states are used. The lower pre-forming states are chosen to have sufficient remaining formability before diffuse necking occurs. If the same pre-forming levels as for the Nakajima experiments were used, the 50 % pre-forming would be beyond the uniform elongation in the tensile test. In total, six different pre-forming levels were investigated in the tensile tests. The levels can be seen in Figure 6.5.

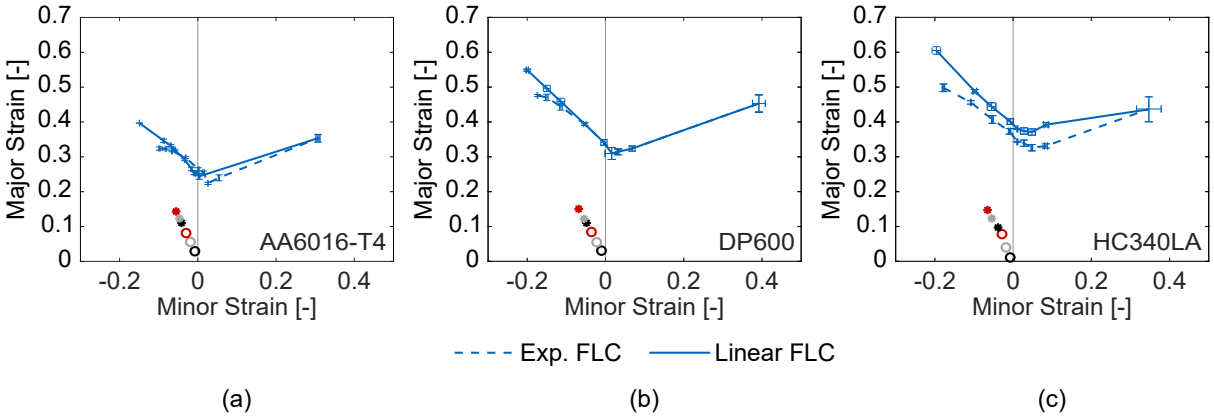

Figure 6.5: Pre-forming levels for AA6016-T4 (a), DP600 (b) and HC340LA (c) used in the consequtive tensile test experiments.

6.2.2 Nakajima Experiments with Pre-formed Materials

Nakajima specimens are cut out from the pre-formed samples to investigate the influence of the pre-forming level and a change in loading direction on the formability. The specimens are cut out at 0°, 22.5° 45°, 67.5°, and 90° with respect to the initial loading direction, which is parallel to the RD.

AA6016-T4

Figure 6.6 represents the results for the aluminium alloy AA6016-T4. Regardless of the pre-forming level or the change in loading direction, the remaining formability remains almost the same. A small reduction is observed for the uniaxial post-forming state in combination with the highest pre-forming level. Here, a reduction of around 20 % with respect to the major strain occurs for the IF0-PF67.5 and IF0-PF90 specimens. The higher the change in loading direction, the higher the loss of formability is.

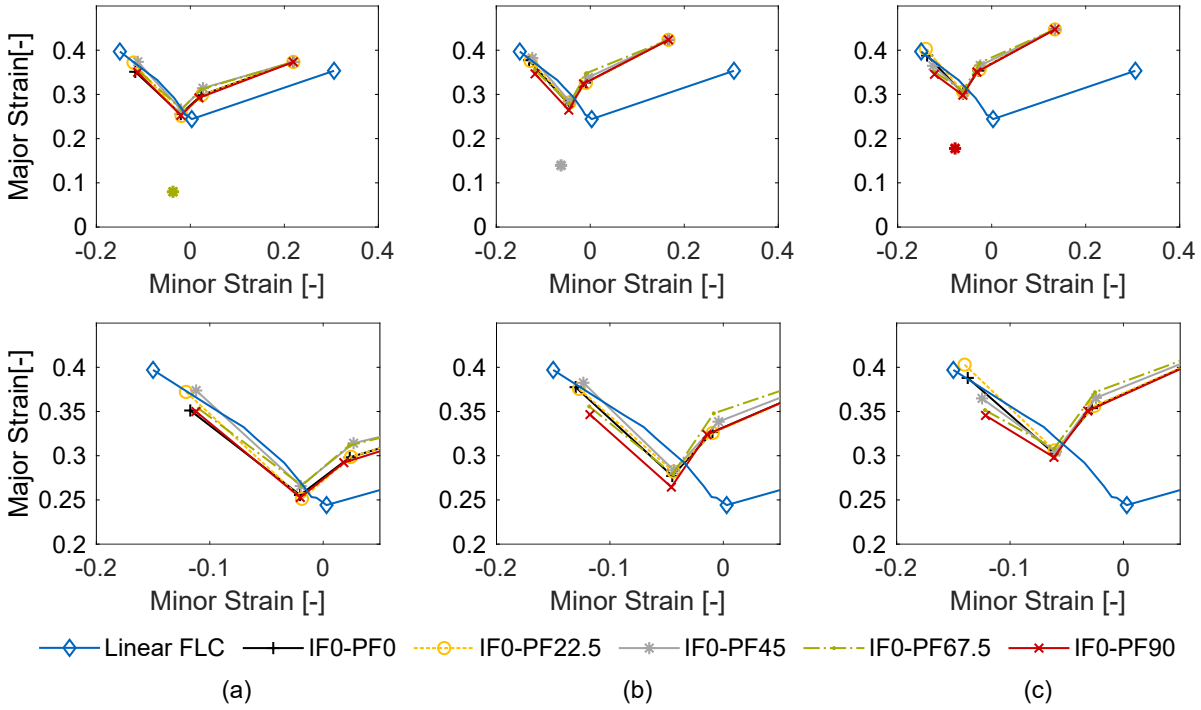

Figure 6.6: Influence of the 25 % (a), the 35 % and the 50 % pre-forming level and a change in loading direction on the formability of the aluminium alloy AA6016-T4.

All specimen geometries tested with this material have shown a sudden occurance of the crack. The detection of the last image before the crack occurs is therefore simple. The determination of the FLCs is done exclusively using the TDEM. The use of the adapted TDEM is not needed for this material as all specimen show an steady increase in the thickness reduction rate $\dot{\varepsilon_3}$ until

the failure of the specimen. In Figure 6.7 the TDEM can be seen for a IF0-PF0 specimen (a) and for a IF0-PF90 specimen (b) after a pre-forming of 50 %.

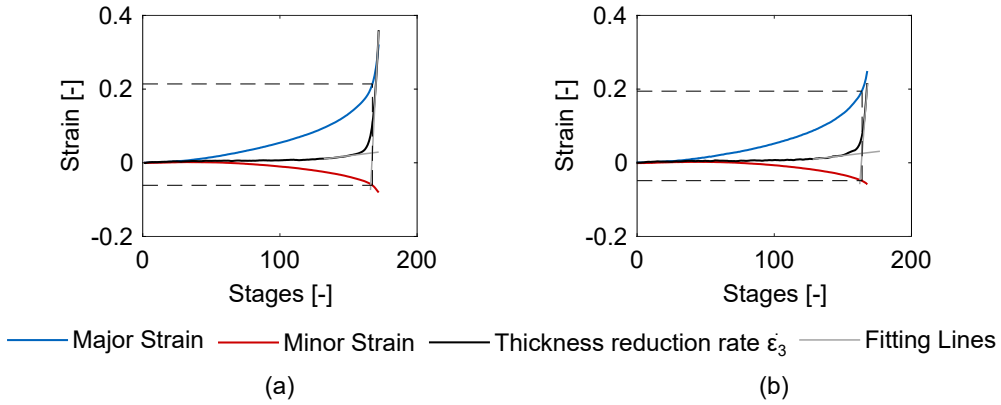

Figure 6.7: TDEM for the 50 % pre-formed aluminium alloy AA6016-T4 and the IF0-PF0 specimen (a) and the IF0-PF90 specimen (b).

When looking at the strain distribution of a 30 mm Nakajima specimen at the time of the onset of necking, a clear necking zone can be observed for the IF0-PF0 and IF0-PF90 specimens after a pre-forming of 50 %, see Figure 6.8. Therefore, failure occurs in the center of the specimen due to a failure over the thickness with a change of the strain state to the plane-strain state. This behaviour is the common failure mode for such a material. The behaviour of the initial material without pre-forming and the material with pre-forming is almost identical regarding the failure mode. Such a failure mode, a necking over the thickness, will be referred to as failure mode *Type I* in the further course.

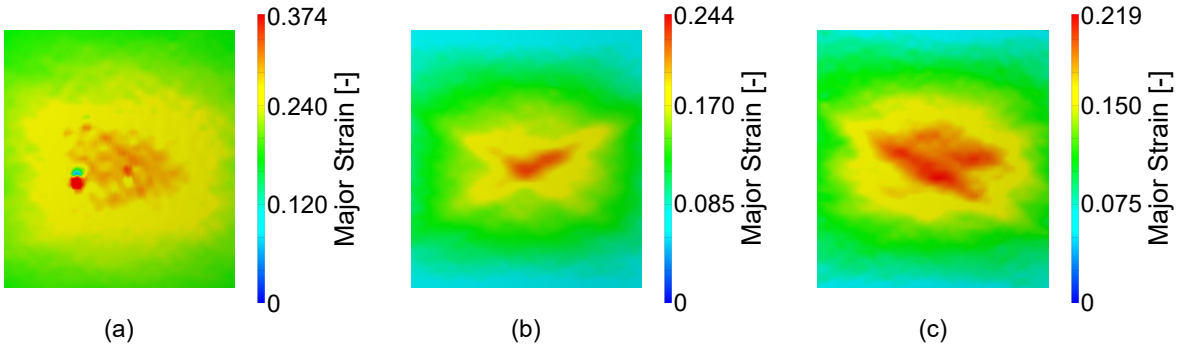

Figure 6.8: Major strain distribution at the onset of necking determined by the TDEM for the aluminium alloy AA6016-T4 and the inital 30 mm specimen (a), the 50 % pre-formed IF0-PF0 specimen (b) and the 50 % pre-formed IF0-PF90 specimen (c).

DP600

For the DP600 steel, an increase in the pre-forming level leads to a decrease in formability after a change in the loading direction. After a pre-forming of 35 % of the linear FLC, a reduction of the formability after a change in loading direction by more than 22.5° of the 30 mm, 100 mm and 130 mm specimens is observed. Tis reduction is even more significant with a pre-forming level of 50 %. The highest influence of a change in the loading direction is found for the 30 mm specimens with their uniaxial load case. The IF0-PF67.5 specimens show the lowest formability of all directions which were investigated. In general, the higher the pre-forming level, the lower the formability after a change in the loading direction, see Figure 6.9.

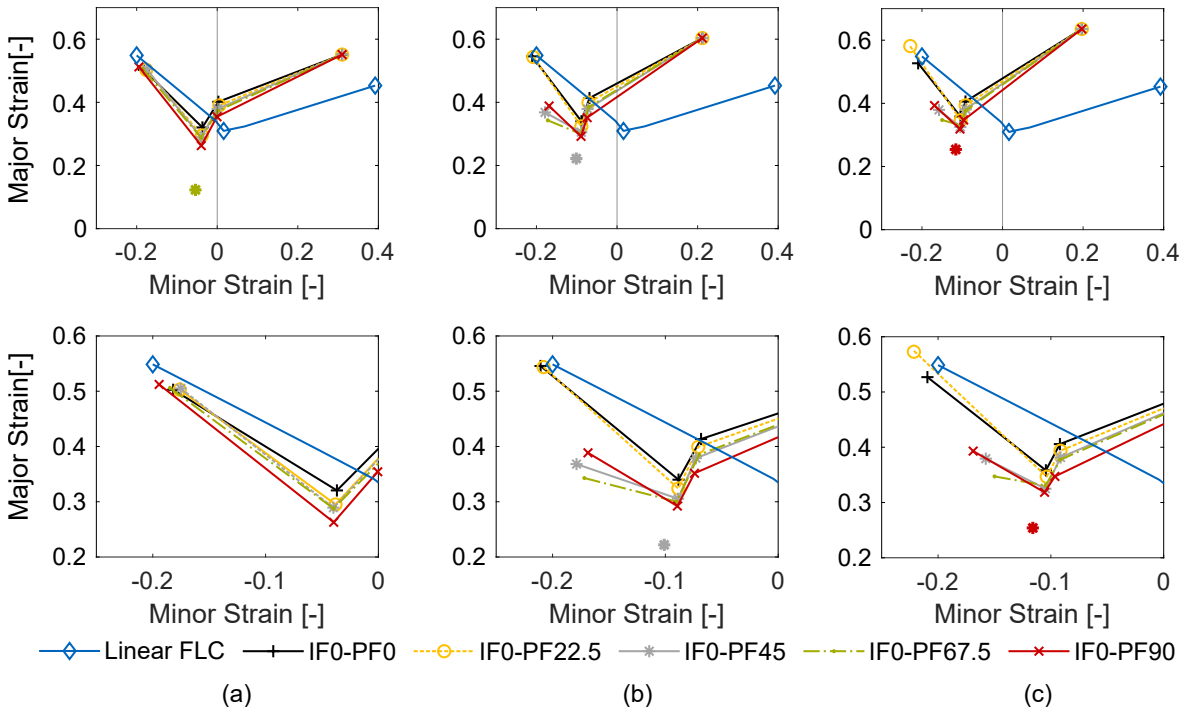

Figure 6.9: Influence of the 25 % (a), the 35 % and the 50 % pre-forming level and a change in loading direction on the formability of the DP600 steel.

The IF0-PF0 or IF0-PF22.5 specimens showed a steady increase in the thickness reduction rate, see Figure Figure 6.10 (a), similar to the aluminium alloy. These two configurations are also the ones which did not show a decrease in the formability after pre-forming. The failure mode of these two configurations is *Type I*.

In comparison to the aluminium alloy or the IF0-PF0 or IF0-PF22.5 specimens, the thickness reduction rate of the IF0-PF67.5 or the IF0-PF90 specimens did not show a steady increase in the thickness reduction rate $\dot{\varepsilon}_3$, see the black line in Figure 6.10 (b).

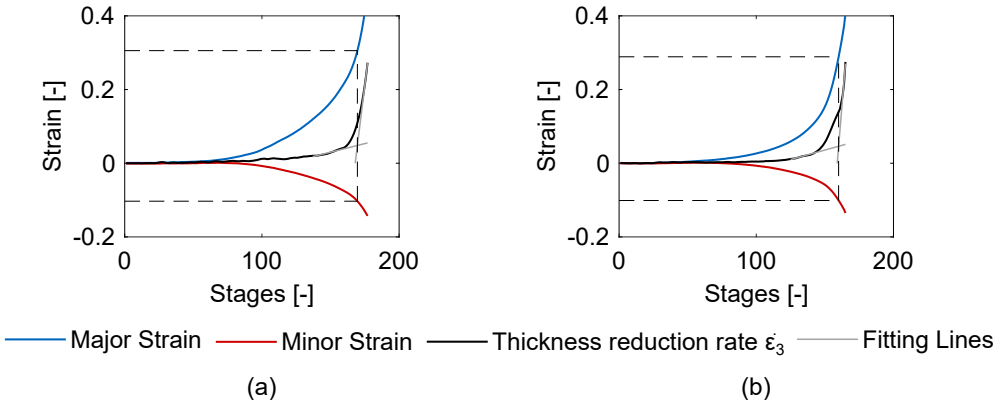

Figure 6.10: TDEM for the 50 % pre-formed DP600 steel and the IF0-PF0 specimen (a) and the IF0-PF67.5 specimen (b).

The specimens with a none steady increase in the thickness reduction rate show a shear failure behaviour. As a pure shear deformation leads to no change in the thickness of the specimen, the thickness reduction rate $\dot{\varepsilon}_3$ is also reduced after the occurrence of a shear band. This leads to the non-steady behaviour of the thickness reduction rate. The occurrence of a shear band happens already in the early stages of the experiment. In the further progress of the Nakajima experiment, one shear band starts to dominate and finally leads to the rupture of the specimen.

The differences between specimens with a localised necking over the thickness, see Figure 6.11 (a), and specimens with a shear failure, see Figure 6.11 (b), is clearly visible. While a necking over the thickness is characterised by a lens-shaped "hot-spot", the shear failure has shear bands. Next to the shear band, almost no increase in the strain is observed. This leads to a sharp decrease in the strains between the shear band and the neighbouring areas. Such a failure mode, a shear failure, will be referred to as failure mode *Type II* in the further course.

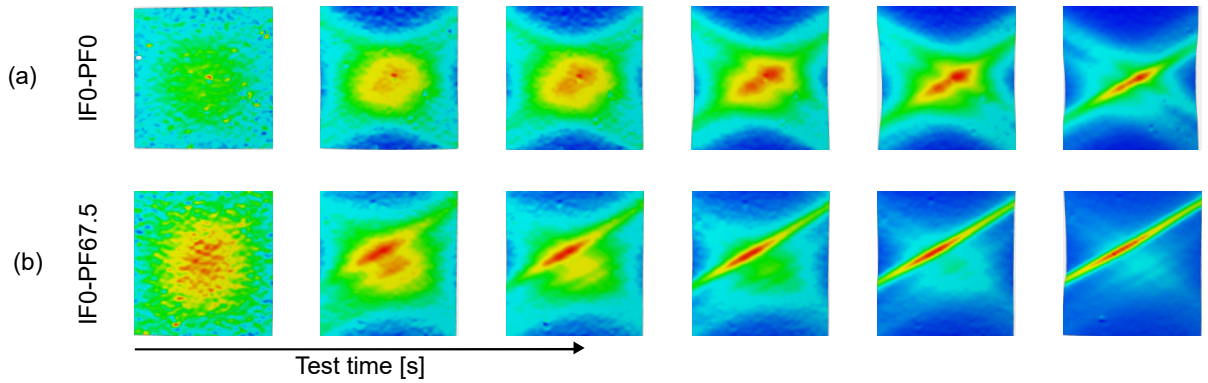

Figure 6.11: Major strain distribution during the Nakajima experiment for the DP600 steel and the 30 mm specimen of the 50 % pre-formed IF0-PF0 specimen (a) and the 50 % pre-formed IF0-PF67.5 specimen (b).

The major strain distributions at the determined onset of localised necking by the TDEM are presented in Figure 6.12. If the determination of the onset of necking is done by the TDEM, a significant overestimation of the formability is assessed for specimens with a shear failure. The major strain distribution of a IF0-PF67.5 specimen is presented in Figure 6.12 (c). The localised shear band is clearly visible.

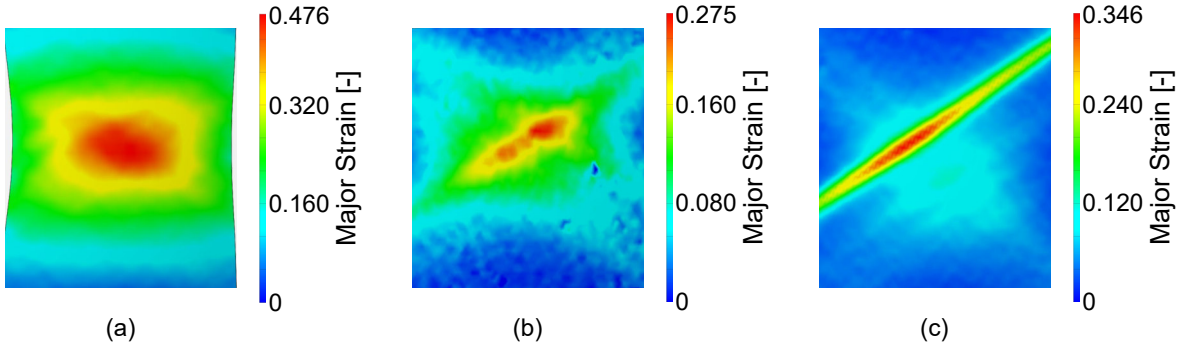

Figure 6.12: Major strain distribution at the onset of necking determined by the TDEM for the DP600 steel and the inital 30 mm specimen (a), the 50 % pre-formed IF0-PF0 specimen (b) and the 50 % pre-formed IF0-PF67.5 specimen (c).

If a specimen showed such a behaviour, a visible shear band and a none steady increase in the thickness reduction rate $\dot{\varepsilon_3}$, the modified TDEM was used to determine the onset of localised necking. Using the modified TDEM, the onset of localised necking is much more reliable. While the classical TDEM leads to strains at which the specimen clearly showed shear bands (see Figure 6.13 (a)), the modified TDEM lead to strains at which the shear bands are not yet visible, see Figure 6.13 (b).

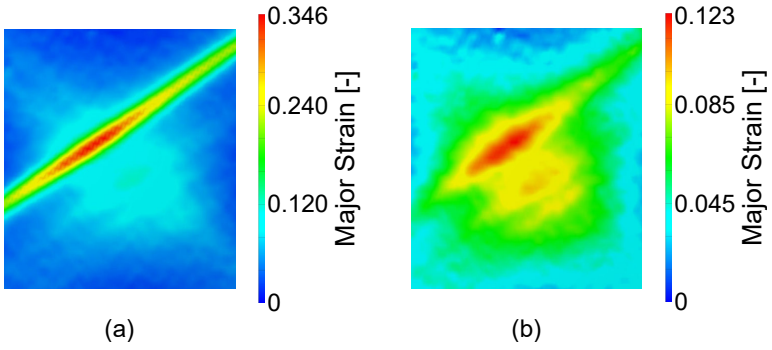

Figure 6.13: Major strain distribution at the onset of necking for the 50 % pre-formed IF0-PF67.5 specimens of DP600 determined by the TDEM (a) and the modified TDEM (b).

HC340LA

The HC340LA is the most affected material when a change in loading direction occurs. Even for the lowest pre-forming level, a reduction of the formability of the 100 mm specimens with a change in loading direction by 67.5° and 90° is visible. At a pre-forming level of 50 % of the linear FLC, almost instant necking occurs for the IF0-PF90 specimens with a width of 100 mm. But again, as already observed for the dual-phase steel DP600, the left-hand side of the FLC is affected the most. This means the specimens with a negative minor strain have the most significant loss of formability.

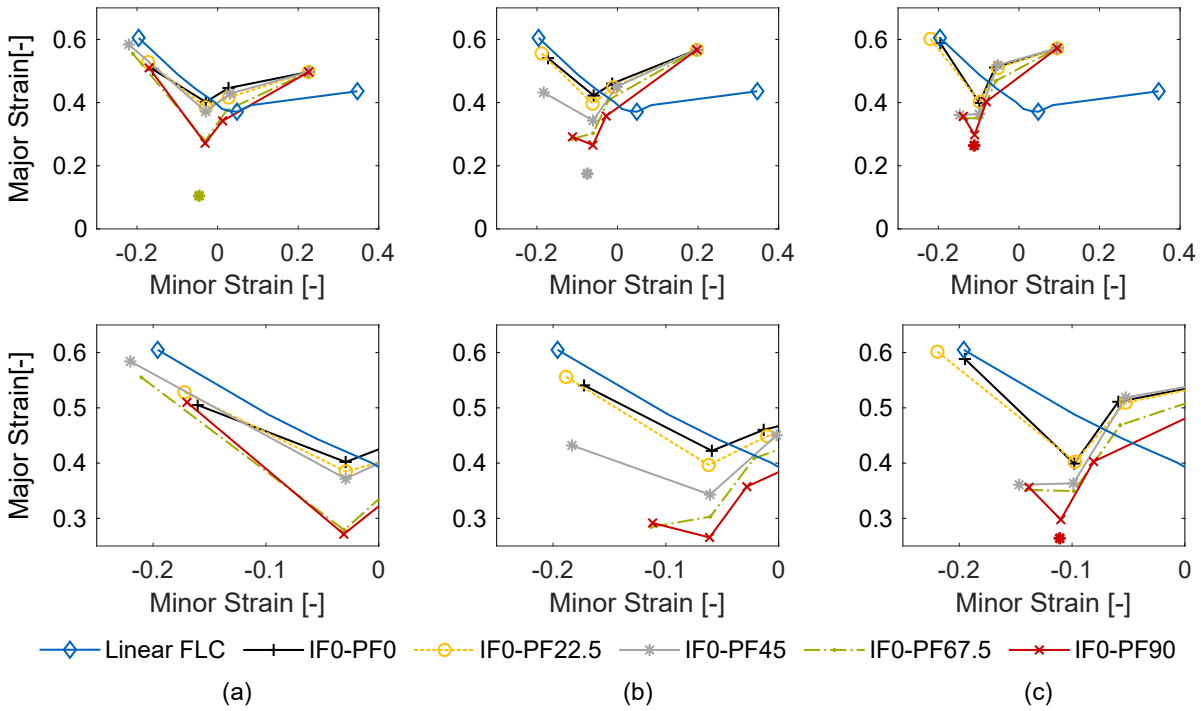

Figure 6.14: Influence of the 25 % (a), the 35 % and the 50 % pre-forming level and a change in loading direction on the formability of the HC340LA steel.

The thickness reduction rate also showed no steady increase for the specimens with a loss of formability. For the HC340LA steel some specimens, such as the IF0-PF67.5 specimens after a pre-forming of 50 %, even a short period with a saturation, therefore no increase in the thickness reduction rate $\dot{\varepsilon}_3$, is found as shown in Figure 6.15 (b). The TDEM assesses the onset of necking of the IF0-PF90 specimens at higher strains than that for the IF0-PF0 specimens. This could lead to the assumption that a change in the loading direction increases the formability of the HC340LA steel which is clearly wrong. Similar to the DP600 steel, the configurations with a loss of formability all showed a *Type II* failure. While the IF0-PF0 and the IF0-PF22.5 specimens show a *Type I* failure mode.

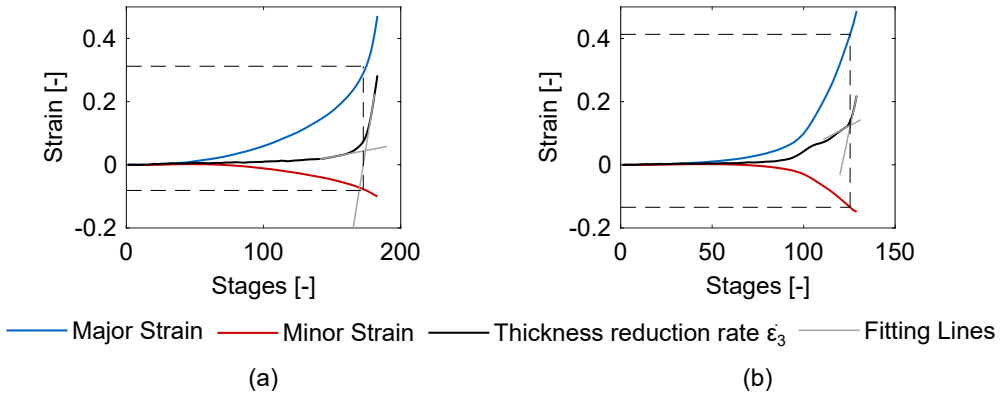

Figure 6.15: TDEM for the 50 % pre-formed HC340LA steel and the IF0-PF0 specimen (a) and the IF0-PF67.5 specimen (b).

A significant overestimation of the formability is assessed when using the TDEM. The shear bands are again clearly visible for the IF0-PF45, IF0-PF67.5 and IF0-PF90 specimens. The shear bands of a IF0-PF67.5 specimen, which showed the lowest formability, can be seen in Figure 6.16. At the beginning of the deforamtion, multiple shear bands are visible from which one leads to the final fracture of the specimen. The IF0-PF22.5 specimens, which showed the highest formability, fail due to necking over the thickness. But also here, some slight shear bands are already visible, but the thickness reduction rate $\dot{\varepsilon_3}$ shows a continuous increase, therefore the TDEM is applied to determine the onset of localised necking.

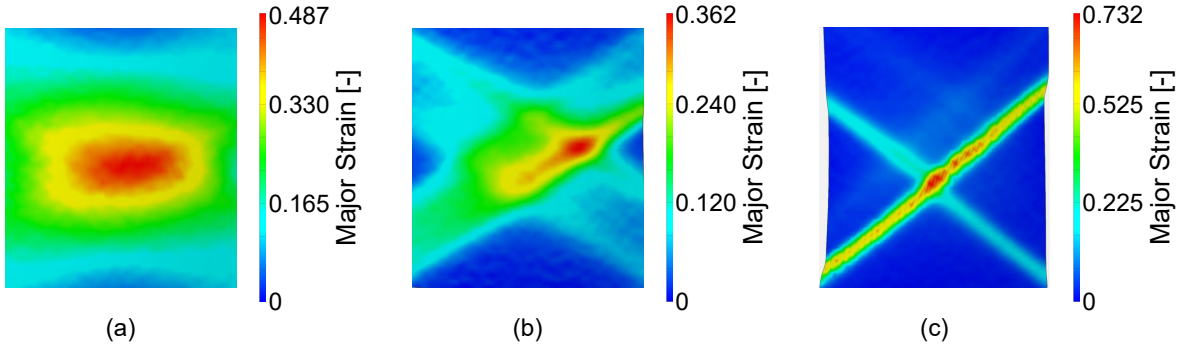

Figure 6.16: Major strain distribution at the onset of necking determined by the TDEM for the HC340LA steel and the inital 30 mm specimen (a), the 50 % pre-formed IF0-PF22.5 specimen (b) and the 50 % pre-formed IF0-PF67.5 specimen (c).

The use of the modified TDEM led to a reliable determination of the onset of necking, see Figure 6.17. The major strain distribution showed no evolved shear bands or any sign of localisation. For all specimens, regardless of the specimen width, which showed a *Type II* failure mode, the modified TDEM is used to determine the onset of necking. In all cases, the modified TDEM lead to realiable values for the FLC.

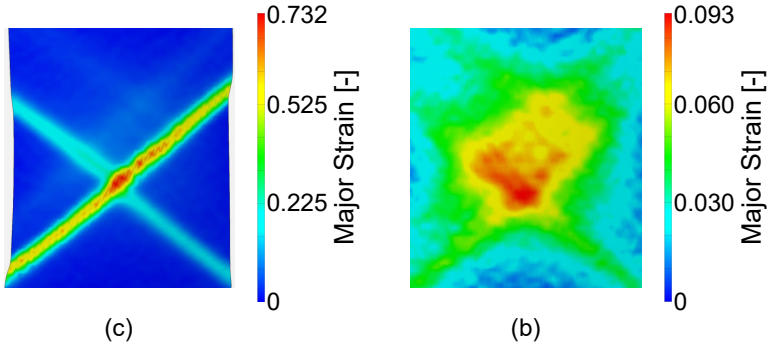

Figure 6.17: Major strain distribution at the onset of necking for the 50 % pre-formed IF0-PF67.5 specimens of HC340LA determined by the TDEM (a) and the modified TDEM (b).

Due to the use of a DIC-system, the strain paths can be further analised. Two different configurations are looked at closer, the uniaxial IF0-PF0 and the IF0-PF90 specimens after a pre-forming of 50 %. Inside the the shear band no change to the plane-strain state occurs for the IF0-PF90 specimens. Nevertheless, for the IF0-PF0 specimens this change of the strain state is visible inside the necking zone. After localisation, the void growth rate is significantly higher for the IF0-PF90 specimens in comparison to the IF0-PF0 specimens for the 50 % pre-formed HC340LA steel. Also the void size is significantly bigger for the IF0-PF90 specimens, see Figure 6.18..

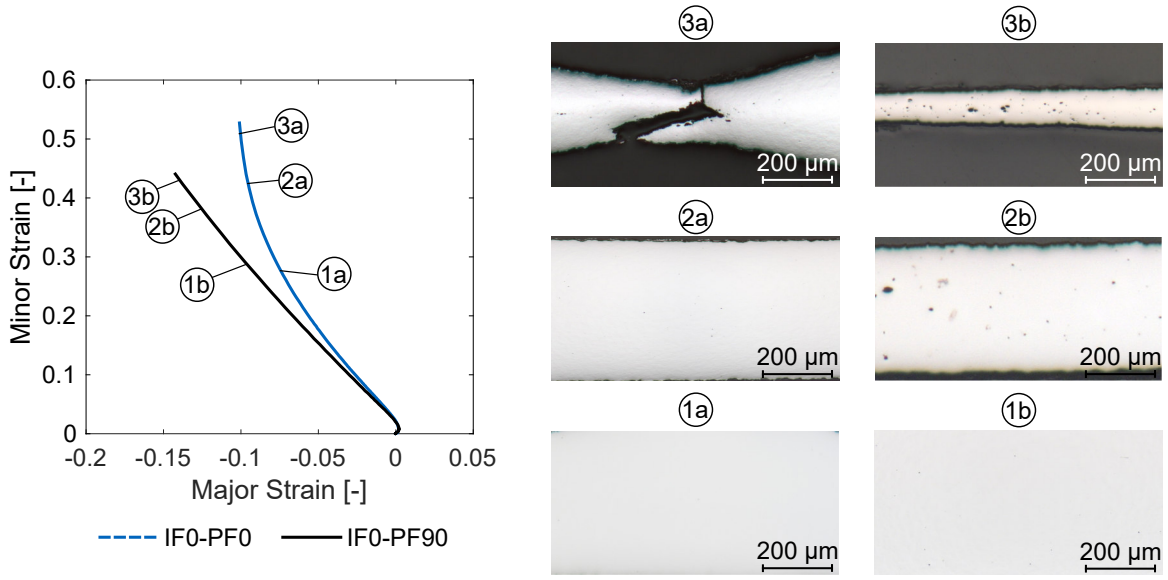

Figure 6.18: Different strain paths of the IF0-PF0 and the IF0-PF90 specimens and the corresponding microstructure at different deformation states.

The Nakajima tests with pre-formed material showed that not all materials are sensitive to a change in the loading direction. For example, the aluminium alloy AA6016-T4 showed hardly any change in formability, regardless of how high the pre-forming level was. All investigated configurations of pre-forming level and change in the loading direction lead to a *Type I* failure mode. This failure type is defined by a localised necking voer the thickness. The determination is, therefore, done exclusively by the TDEM.

On the other hand, the steels showed a clear dependence of formability on a change in the loading direction. If a certain pre-forming level is exceeded, a change in the loading direction leads to a significant decrease in the achievable degrees of deformation. The single-phase steel HC340LA showed the highest loss of formability of the three investigated materials. In the uniaxial post-forming state, the IF0-PF67.5 specimens showed the earliest onset of localised necking.

Looking at the strain distribution over the expierment, the specimens with a reduced formability show the formation of shear bands with a *Type II* failure mode. The specimens show numerous shear bands at the begin of deformation, but as the test progresses, a shear band forms, which finally leads to shear failure. The classic determination of the FLC using the TDEM is unreliable in such a failure case. This is caused by the fact that the thickness reduction rate $\dot{\varepsilon}_3$ shows no constant increase over the experiment. For some combinations, even a stagnation of the increase is observed. The TDEM leads to an apparent overestimation of the forming capacity. However, by introducing a modified TDEM, such shear failures can also be analysed. The modified TDEM leads to much more reliable results.

6.2.3 Tensile Tests with Pre-formed Materials

Due to the experimental setup in the Nakajima experiment, it is challenging to attach additional measuring equipment. Therefore, in order to carry out further investigations into the cause of the occurrence of shear failure, the tensile test is used. The good accessibility of the sample makes it possible to attach different sensors to the sample, such as temperature sensors for example. Here again, pre-formed samples are examined. The pre-forming levels are already presented in section 6.2.1 and lie below the ones used for the Nakajima experiments. Again, as for the Nakajima experiments, five different post-loading directions are chosen. The strains shown are related to the extensometer measuring length of 50 mm, representing the global strains while the results of the Nakajima experiments represent the local strains.

A closer look at the results in terms of uniform and fracture elongation shows that above a certain pre-forming level, approximately $\varepsilon_{pre} = 0.08$, the steels have a significant decrease in formability, see Figure 6.19 (b) and (c). Even a small increase in the pre-forming level from $\varepsilon_{pre} = 0.05$ to $\varepsilon_{pre} = 0.08$ substantially reduces the uniform and fracture elongation. This sudden behaviour occurs at the same pre-forming levels regardless of the different strengths and microstructures of the HC340LA and DP600 steels. The HC340LA steel shows the most significant loss of formability after a change in the loading direction. This is in good agreement with the findings of the Nakajima experiments. As already in the Nakajima experiments, the aluminium alloy is hardly influenced by a change in the loading direction on the uniform or fracture elongation.

The different colours in Figure 6.19 indicate failure due to necking, a *Type I* failure mode (blue) or failure due to shear failure, a *Type II* failure mode (red). for the specimens with no change in the loading direction, the IF0-PF0 specimens, a linear decrease of the formability is observed. The linear decrease corresponds well with the increased pre-forming level.

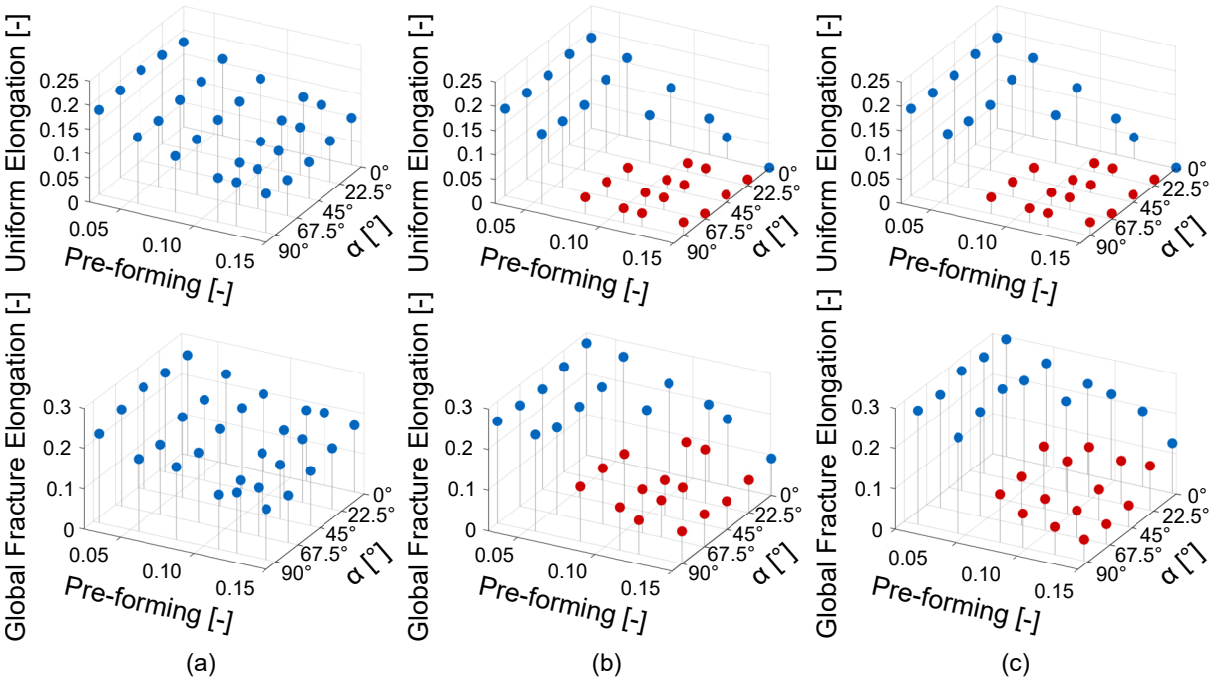

Figure 6.19: Uniform and fracture elongation of pre-formed AA6016-T4 (a), DP600 (b) and HC340LA (c) under different loading angles.

The decrease in the fracture elongation corresponds well with the reduction in the uniform elongation for specimens with a change in the loading direction. If the uniform elongation occurs at low strains, almost instantly after the onset of yielding, the fracture elongation is significantly reduced. Next to the elongations, also the hardening behaviour of the different

materials is further investigated. The flow curves of the differently pre-formed specimens are compared to the flow curve of the corresponding initial material in RD. The pre-forming strains are added to the strains obtained in the tensile test.

For the aluminium alloy AA6016-T4, the IF0-PF0 specimens show a latent hardening behaviour followed by an increase in the flow stress. The increase in the flow stress is similar to that of the initial material, see Figure 6.20. Such a latent hardening could also be observed for the IF0-PF22.5 specimens at higher pre-forming levels. All other observed loading directions lead to a permanent softening of the material. When softening the material occurs, the flow curve after a change in the loading direction is below the flow curve of the initial material. A higher permanent softening is noticed for higher pre-forming levels and changes in the loading direction (IF0-PF67.5 and IF0-PF90 specimens).

At the beginning of the experiment, specimens with a change in loading direction show different elastic-plastic transition. While the IF0-PF0 specimens are characterised by a sharp transition with a latent hardening, which makes it easy to determine the onset of plastification, the elastic-plastic transition is much smoother for specimens with a change in the loading direction. The higher the pre-forming level and the higher the change in loading direction, the smoother the transition is.

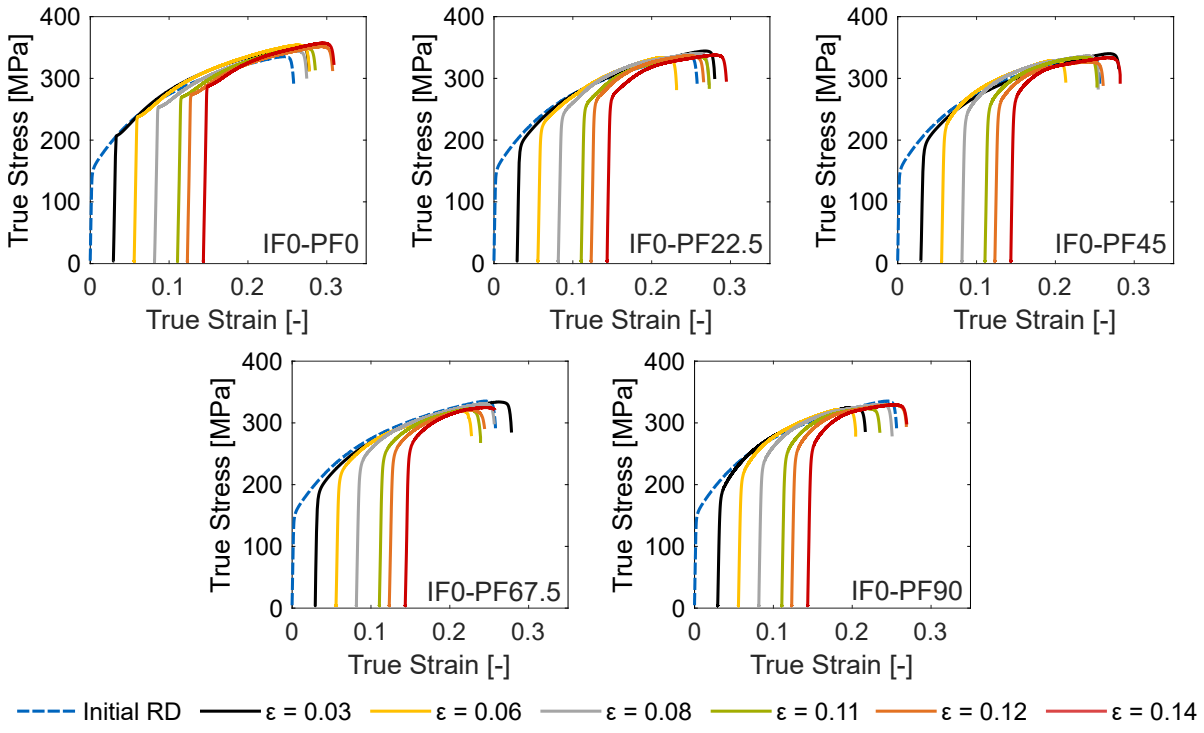

Figure 6.20: Flow curves of the aluminium alloy AA6016-T4 for the different pre-forming levels and changes in the loading direction in comparison to the initial flow curve in RD.

For the DP600 steel, the proportional load cases with no change in the loading direction (IF0-PF0) reveal a latent hardening behaviour. After the latent hardening period, the flow curve follows the flow curve of the initial material quite well. Due to the latent hardening behaviour, the onset of yielding can be easily determined. As soon as there is a change in loading direction in combination with a certain pre-forming level of $\varepsilon_{pre} = 0.08$, the flow curves behave differently. A stress overshoot can be observed at the beginning of the experiment, where the flow curve lies above the initial flow curve. The higher the change in loading direction, the higher the observed stress overshoot is.

After the stress overshoot, the flow curve shows a negative hardening behaviour meaning that the flow stress is reduced with increasing strain. The flow curves with decreasing flow stress also show a shear failure (*Type II* failure mode), presented by the red dots in Figure 6.19. For those specimens with such a significant loss of formability, determining the onset of yielding is especially difficult. The elastic-plastic transition is very smooth, and for high pre-forming levels ($\varepsilon_{pre} = 0.12$ or $\varepsilon_{pre} = 0.15$), the transition starts already at low stresses. This can be seen for the IF0-PF90 specimens after a pre-forming of $\varepsilon_{pre} = 0.15$, where a deviation from the linear elastic behaviour is visible at lower strains.

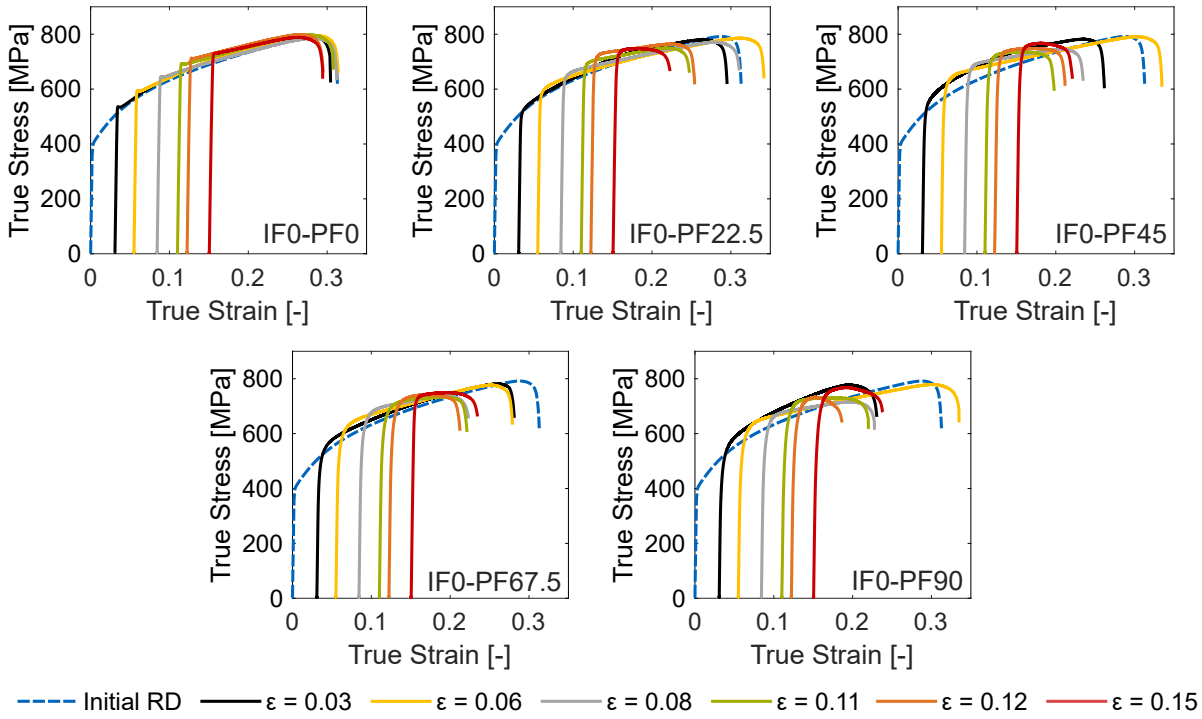

Figure 6.21: Flow curves of the DP600 steel for the different pre-forming levels and changes in the loading direction in comparison to the initial flow curve in RD.

Compared to the DP600 steel, the HC340LA steel shows an even higher stress overshoot for specimens with a change in loading direction higher than 45°. For high pre-forming levels, above ε_{pre} = 0.1, and high changes in the loading direction (IF0-PF45, IF0-PF67.5 and IF0-PF90), the flow stress decreases rapidly after reaching the uniform elongation. This decrease is even more significant with higher pre-forming levels. Specimens with no change in loading direction (IF0-PF0) show a latent hardening followed by an increase in the flow stress similar to the hardening behaviour of the initial material. As for the DP600 steel, the determination of the onset of yielding is difficult by the standardised methods. Again, the transition between the elastic and the plastic regime is challenging to distinguish.

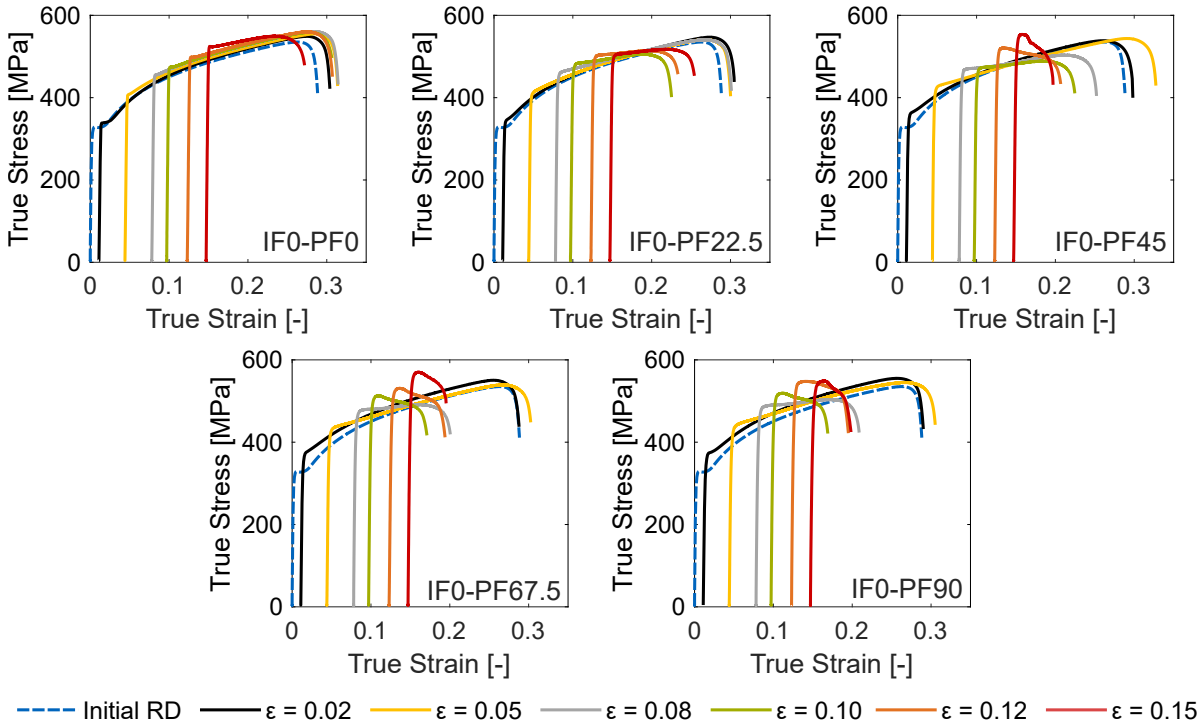

Figure 6.22: Flow curves of the HC340LA steel for the different pre-forming levels and changes in the loading direction in comparison to the initial flow curve in RD.

In summary, the results of the Nakajima tests are reflected in the tensile tests. The aluminium alloy does not show any influence of pre-forming or a change of loading direction with regard to uniform and fracture elongation. The AA6016-T4 was the only material where a permanent softening occured after pre-forming and a change in the loading direction.

For the steels, a permanent hardening behaviour is observed at low pre-forming levels as soon as a change in loading direction is applied. With increasing pre-forming level, a change in the loading direction leads to a reduction of the forambility. As for the Nakajima experiments, the

uniform and fracture elongation is significantly reduced. The specimens which show a stress overshoot correspond well with the specimens showing reduced formability in Figure 6.19. The specimens with a reduced formability all show a *Type II* failure mode.

The use of a DIC-System allows a closer look at the strains inside the failure zone during the tensile test experiments. A sufficiently small facet size of approximately 0.5 mm is required where the facets fit into the shear band. For specimens with a pre-forming level of $\varepsilon_{pre} = 0.05$ a shift towards the plane-strain state occurs. this behaviour is in good agreement with the assumptions made by the eMMFC - model by Hora et al. (1996). This happens regardless of the applied loading direction. Such a behaviour is expected for a ductile failure over the thickness (*Type I* failure mode). After a pre-forming of $\varepsilon_{pre} = 0.1$, the IF0-PF0 specimens again show a ductile failure behaviour with a change in the strain state towards plane-strain. The IF0-PF90 specimens, on the other hand, show no shift in the plane-strain state, see Figure 6.23 (b). As there is no change to the plane-strain state, a predicition of such a *Type II* failure mode by the eMMFC - model is difficult.

Compared to the strains measured in Figure 6.19, the strains determined by the DIC-System are much higher. Therefore, the strains in Figure 6.19 are global strains using a measurement length of 50 mm, while the strains in Figure 6.23 are local strains with a measurement length of approximately 0.5 mm.

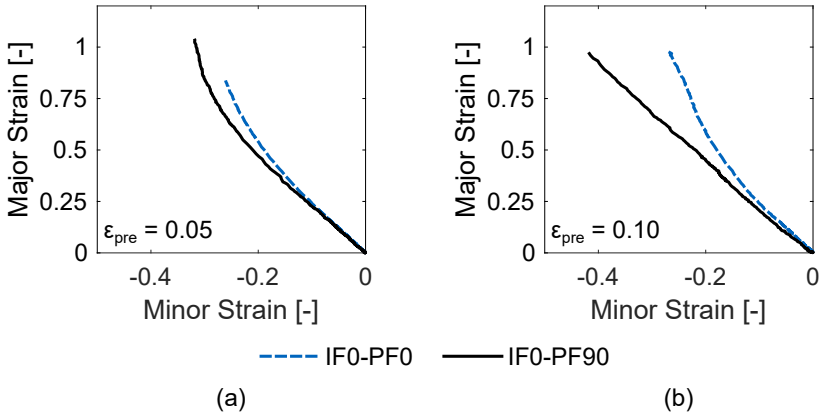

Figure 6.23: Strain path for the HC340LA steel with different pre-forming levels at $\epsilon_{pre} = 0.05$ (a) and $\epsilon_{pre} = 0.1$ (b).

6.2.4 Differences between Nakajima Experiments and Tensile Tests with Pre-formed Materials

Applied Strain Rate

The results of the Nakajima experiments and tensile tests show differences. The most pronounced difference is that in the Nakajima experiments, a pre-forming level of approximately $\varepsilon_{pre} = 0.15$ is required to distinguish the effect of a change in the loading direction. In the tensile tests, a pre-forming level of $\varepsilon_{pre} = 0.08$ is sufficient to see a significant loss of formability. To further investigate the reasons for this behaviour, different experiments are conducted.

One difference between the two mentioned experiments is the strain rate which is applied during the tests. Therefore, two pre-forming and directional change combinations are examined in more detail below. The IF0-PF0 and IF0-PF90 specimens with a pre-forming of $\varepsilon = 0.1$. For those combinations, the strain rate is varied from the quasi-static rate at 0.00025 1/s up to 0.1 1/s.

The aluminium shows a low strain-rate dependency for the IF0-PF0 specimens, which is expected for this material grade, see Figure 6.24. Regardless of the applied strain rate, the flow curves all show the same strength for the IF0-PF90 specimens. Nevertheless, a reduced fracture elongation is observed with increasing strain rate, independent of the loading direction.

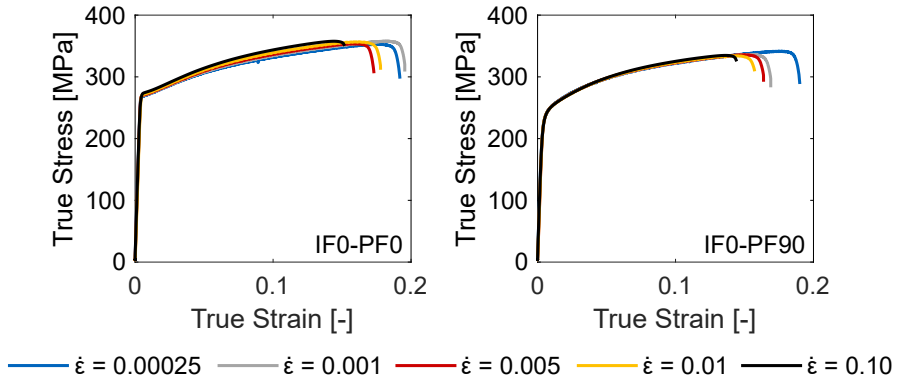

Figure 6.24: Flow curves of the AA6016 specimens with $\varepsilon_{pre} = 0.1$ for different strain rates.

The two steel grades on the other hand reveal a strain rate dependency, see Figure 6.26 and Figure 6.25. The flow curve is increased with increasing strain rate. The HC340LA steel shows the higher strain rate dependency compared to the DP600 steel. This behaviour is also observed for the initial material without pre-forming. For the IF0-PF0 specimens a loss of ductility is observed with increasing strain rate. The IF0-PF90 specimens on the other hand show an increase in strength and an increase in the ductility with rising strain-rate. The uniform and

fracture elongation is significantly increased at a strain rate of 0.1 1/s. This means, that the material has a positive work hardening behaviour which is not observed for lower strain rates.

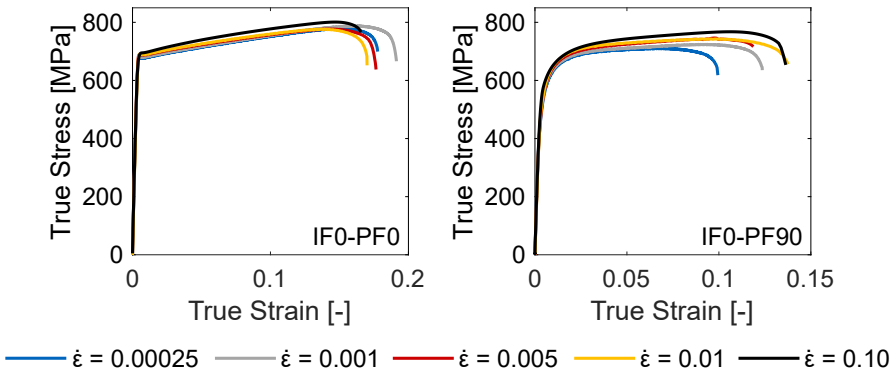

Figure 6.25: Flow curves of the DP600 specimens with $\varepsilon_{pre} = 0.1$ for different strain rates.

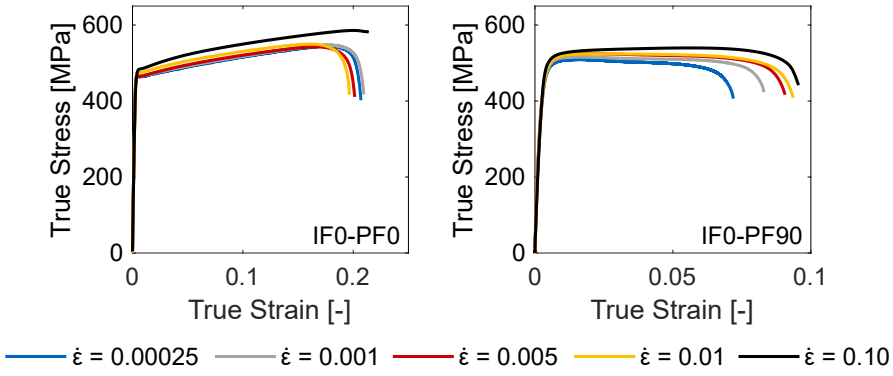

Figure 6.26: Flow curves of the HC340LA specimens with $\varepsilon_{pre} = 0.1$ for different strain rates.

Strain rate sensitivity is a phenomenon caused by dislocation movement. Below a critical strain rate of approximately $\dot{\varepsilon} = 0.005$, the deformation is athermally activated. In this regime, the flow stress is dominated by the interaction between long-range obstacles and dislocations. Beyond the critical strain rate, the deformation is thermally activated and shows a higher strain rate dependency. This is also observed for the steel grades in this study. In this regime, thermal energy assists in overcoming short-range Peierl's stress barriers. Peierl's stress is the force required to move a dislocation within a lattice plane. It depends on the size and width of the dislocation and the lattice distance. Nevertheless, the waiting time for dislocations to overcome short-range obstacles is reduced at higher strain rates. Additional mechanical energy has to be added, which leads to an increased flow stress. (Larour et al., 2013)

As the formability and the flow stress are increased in the experiments with the IF0-PF90 steel specimens, dislocation mechanisms are one reason for this behaviour. Also, the processes which cause the loss of formability are time-dependent. The loss of formability is reduced with less available time due to the higher strain rate.

Bending Effect

The experimental setup of the Nakajima experiments consists of a hemispherical punch with a diameter of 100 mm, see Figure 2.4 (a). The hemispherical punch leads to a bending of the specimen. Such a curvature can postpone the rupture of the specimen. A strain gradient in the thickness direction of the specimen causes this effect. (Hora and Tong, 2008)

To overcome the bending effect, Marciniak experiments with the HC340LA steel are conducted. This experimental setup has a flat punch and, therefore, no bending effect in the evaluation area of the specimen, see Figure 2.4 (b). Also, no contact between the punch and the specimens takes place due to the carrier blank. The observed area is hence friction-free.

For the experiments, the samples were pre-formed to the same levels as for the Nakajima experiments. The investigations with the Marciniak setup are limited to the IF0-PF0 and IF0-PF90 samples. The formability of the material shows that already for the pre-forming level of 25 % a small reduction of the formability is observed, see Figure 6.27 (a). The higher the pre-forming level, the higher the loss of formability for the IF0-PF90 specimen is, see Figure 6.27 (b) and (c).

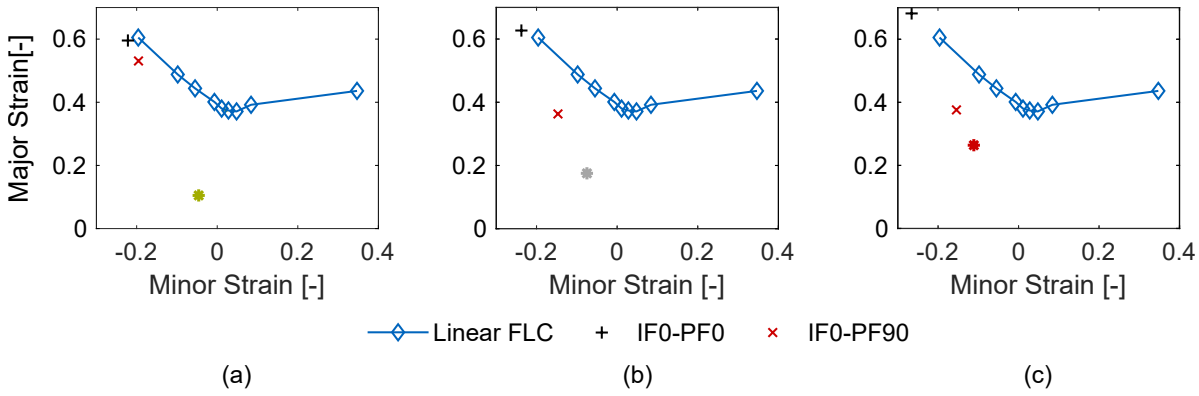

Figure 6.27: Influence of the 25 % (a), the 35 % and the 50 % pre-forming level and a change in loading direction on the formability of the HC340LA steel obtained by the Marciniak experiment.

When the results of the Nakajima experiments, shown in Figure 6.14, are compared to the results of the Marciniak experiments, the IF0-PF0 specimens show an increase in formability. This increase is caused by the more linear strain path in the Marciniak setup. Again due to the hemispherical punch in the Nakajima setup a biaxial pre-forming takes place at the beginning of the experiment. This biaxial pre-forming takes not place in the Marciniak setup. A biaxial pre-forming is known to reduce the formability in a uniaxial post-forming, see Figure 2.26 (b).

A closer look at the major strain distribution of the samples with a pre-forming level of 50 % shows similar results as the Nakajima experiments. The IF0-PF0 specimens show a localised necking with a failure over the thickness. For the IF0-PF90 multiple, parallel shear bands are visible. Compared to the Nakajima experiments, the amount of visible shear bands significantly increases. Again, the localisation takes place already at low strains. The areas next to the shear bands show no further deformation after localisation. In the further progress of the experiment, one shear band leads to the final failure of the material.

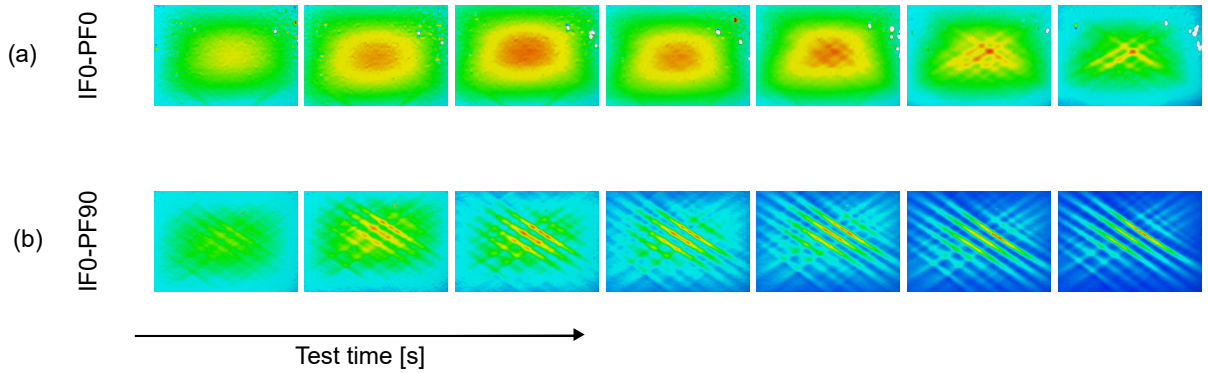

Figure 6.28: Major strain distribution during the Marciniak experiment for the HC340LA steel and the uniaxial specimen of the 50 % pre-formed IF0-PF0 specimen (a) and the 50 % pre-formed IF0-PF90 specimen (b).

6.2.5 Summary of the Macroscopic Experiments

In summary, the macroscopic experiments revealed that not all materials are sensitive to a change in the loading direction. The examined aluminium alloy AA6016-T4 is almost insensitive to a change in loading direction, irrespectively of the applied pre-forming level. This is in strong contrast to the investigated steel materials DP600 and HC340LA. A strong dependency of the remaining formability on the loading direction is observed for both materials. After a certain pre-forming level, a significant reduction after a change in the loading direction can be observed. This loss of formability happens for specimens which show a shear failure (*Type II* failure mode).

Therefore, no classical necking over the thickness emerges. Instead, multiple shear bands start to evolve from which one leads to the final failure of the specimen. The onset of localised necking can not be evaluated using the TDEM. Instead, a novel modified TDEM is introduced to overcome this problem. The use of the modified TDEM, for specimens with a *Type II* failure mode, leads to much more reliable results.

The results of the uniform and fracture elongation in the tensile test confirmed the observations from the Nakajima experiments. Again, the aluminium alloy shows no dependency of the formability on a change in the loading direction, while the steels show a clear dependency. Nevertheless, also for the aluminium alloy, the flow curves are different. A change in the loading direction after a certain pre-forming level leads to a permanent softening of the material. Also, the onset of yielding is strongly affected. All examined materials show a latent hardening for the IF0-PF0 specimens. This makes the determination of the onset of yielding easier. Specimens with a change in the loading direction all show a smooth elastic-plastic transition. This smooth transition makes an assessment of the yield strength difficult.

One reason the effect of the loss of formability in the tensile and Nakajima tests occurs at different strain levels is the applied strain rate. While for the tensile tests with a strain rate of $\dot{\varepsilon} = 0.001$ 1/s, the sudden loss of formability is visible at $\varepsilon_{pre} = 0.08$. The Nakajima tests have a strain rate of up to $\dot{\varepsilon} = 0.3$-0.4 1/s close to fracture, see Figure 6.7, 6.10 and 6.15. This increases the formability of the material, as shown in the tensile test and requires higher pre-forming levels of minimum $\varepsilon_{pre} = 0.15$ to make the loss of formability visible.

Another reason is the bending effect which inevitably occurs using the Nakajima setup. This bending effect postpones the rupture of the material. When using a Marciniak setup, a small loss of formability is already observed at a pre-forming level of $\varepsilon_{pre} = 0.1$ of 25 % of the linear FLC. Nevertheless, this effect is small compared to that of the strain rate.

6.3 Microscopic Experiments

Microscopic experiments allow a closer look into the material and the mechanisms leading to the observed results from the macroscopic experiments. Due to the better accessibility, the tensile test is used to further investigate the materials. Four configurations of pre-forming levels and loading directions are chosen for the following experiments. The chosen configurations are the IF0-PF0 and IF0-PF90 specimens at a pre-forming level of $\varepsilon_{pre} = 0.05$ and $\varepsilon_{pre} = 0.1$. The low pre-forming level of $\varepsilon_{pre} = 0.05$ showed no influence of a change in the loading direction on the formability in the tensile test, while for the pre-forming level of $\varepsilon_{pre} = 0.1$ a strong dependency is observed for the two steel materials DP600 and HC340LA. Therefore, the four selected configurations offer a detailed view of the microscopic mechanisms inside the materials.

6.3.1 Determination of the Onset of Yielding

One finding of the macroscopic tensile tests is the different behaviour of the materials after a change in the loading direction at the onset of yielding. Temperature-based methods and Young's modulus method are used to determine the onset of yielding, as presented in section 5.2.2.

For the AA6016-T4, the change in loading direction leads to a reduced yield strength determined by the temperature-based methods, see Figure 6.29. This reduction is not observed when the classical method using Young's modulus is applied. This discrepancy is due to the fact that the temperature signal, depicted in blue in Figure 6.29, is significantly rounder when the loading direction is changed. As the deviation from the linear decrease is used to determine YS_0, the value is therefore significantly below $YS_{0.2\%}$ or YS_{Tmin}. The higher the pre-forming level, the higher the difference between the three applied methods. Nevertheless, the smoother temperature signal corresponds quite well with the smoother elastic-plastic transition, which is visible in the stress-strain curve.

For specimens with no change in loading direction (IF0-PF0), the elastic-plastic transition is sharp, and also the temperature signal is sharper than the signal of the IF0-PF90 specimens. Due to the sharp transition, the two temperature-based methods are close to each other while the $YS_{0.2\%}$ shows again a higher yield stress. For those specimens, the latent hardening behaviour is clearly visible in figure 6.29 (a) and (c). The YS_{Tmin} and YS_0 values are below the onset of the latent hardening.

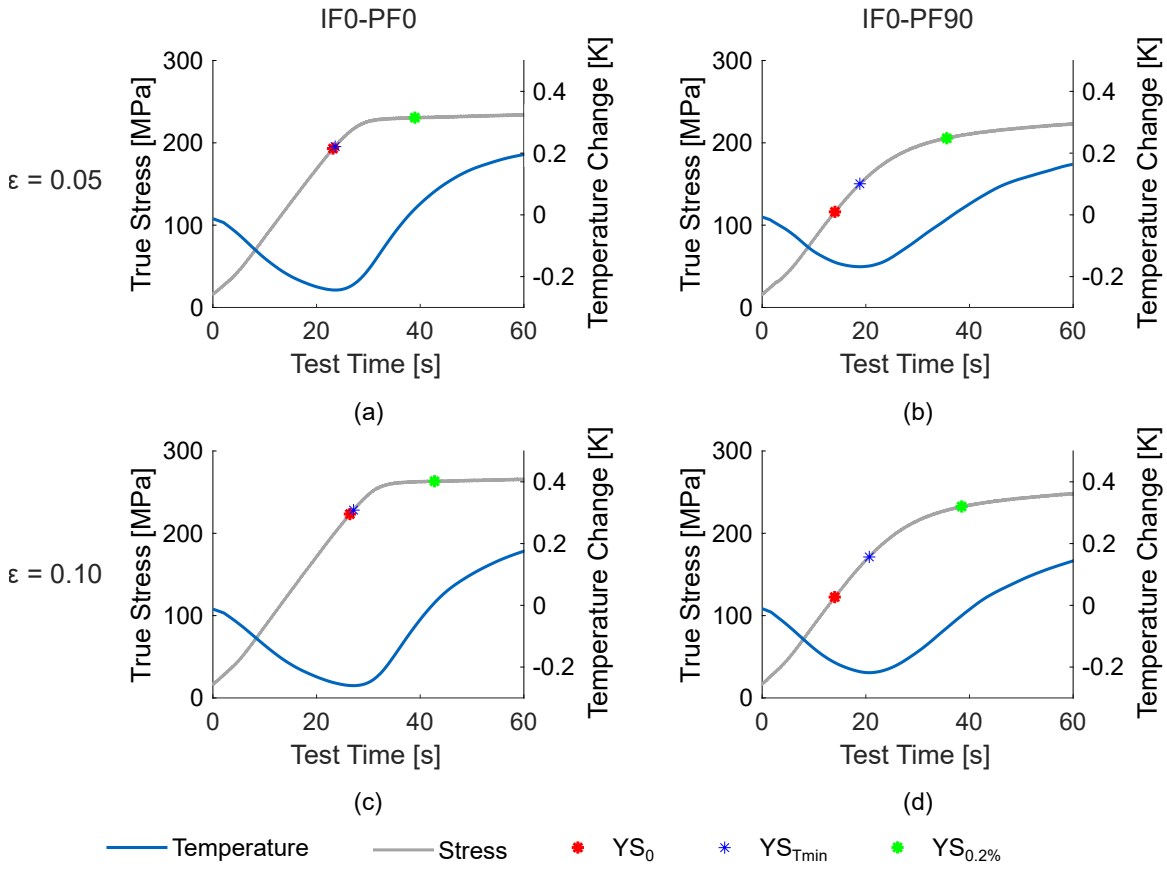

Figure 6.29: Determination of the onset of yielding for the AA6016-T4 with the configurations IF0-PF0, $\varepsilon_{pre} = 0.05$ (a), IF0-PF90, $\varepsilon_{pre} = 0.05$ (b), IF0-PF0, $\varepsilon_{pre} = 0.10$ (c) and IF0-PF90, $\varepsilon_{pre} = 0.10$ (d).

The two steel materials show a similar behaviour to the aluminium alloy. Here, too, a change in the direction of loading leads to a reduced yield stress in the case of determination using temperature-based methods in comparison to the $YS_{0.2\%}$-method, see Figure 6.30 (b) and (d). The temperature signal of the IF0-PF0 specimens is even sharper than that of the aluminium alloy, also caused by the higher amount of work needed to deform the material. The higher the work, the higher the temperature increase during plastification, as most of the work is dissipated into heat. The results for the DP600 are shown in the appendix in section D.2.

The finding that the temperature-based methods migrate closer together at a proportional load (IF0-PF0) after pre-forming is in good agreement with the results of Vitzthum et al. (2022a). Here the same effect was observed and attributed to the fact that the already plasticised grains already have activated slip planes. These are reactivated almost simultaneously when a new load in the same direction is applied, leading to this sharp transition between elastic and plastic material behaviour.

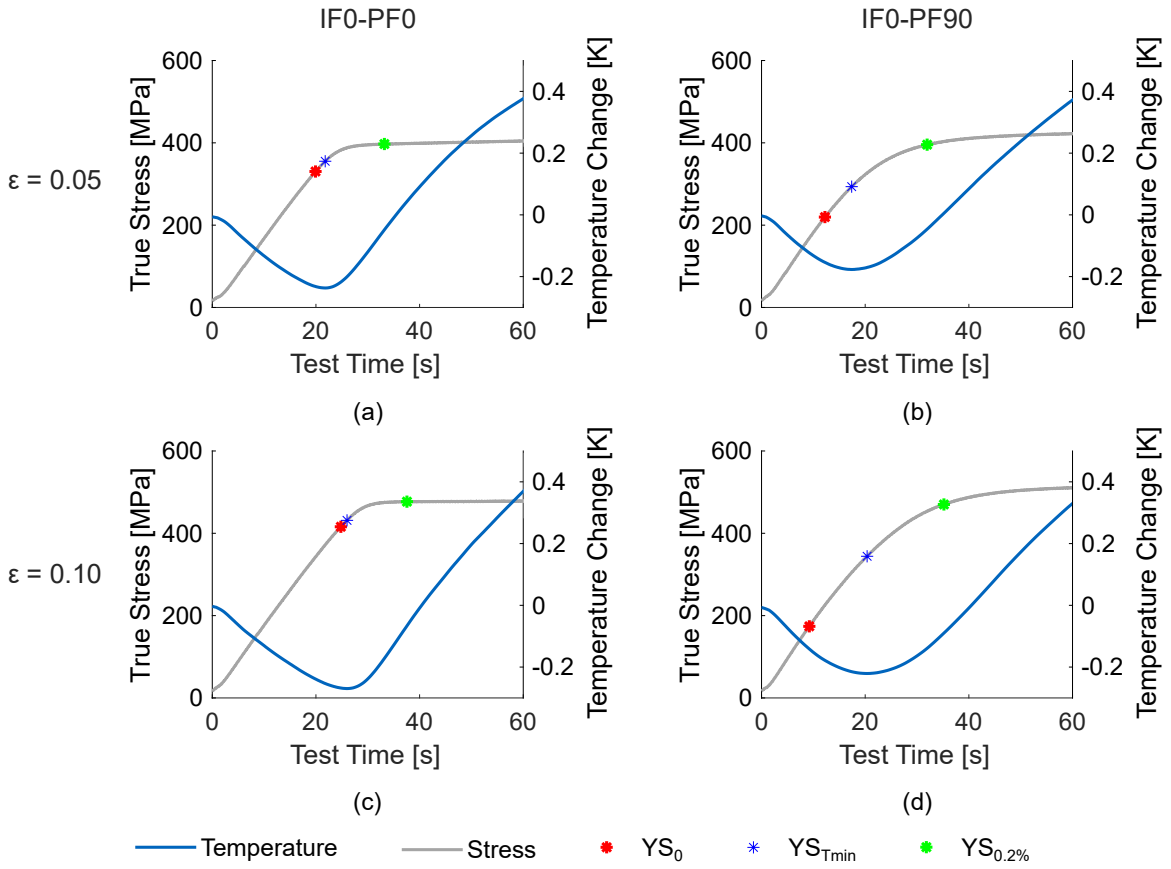

Figure 6.30: Determination of the onset of yielding for the HC340LA with the configurations IF0-PF0, $\epsilon_{pre} = 0.05$ (a), IF0-PF90, $\epsilon_{pre} = 0.05$ (b), IF0-PF0, $\epsilon_{pre} = 0.10$ (c) and IF0-PF90, $\epsilon_{pre} = 0.10$ (d).

Evaluation of the Lattice Strains

The different behaviour of the temperature signals is connected to mechanisms on a microscopic scale. One way to investigate those mechanisms is the look at the strains inside the individual lattice planes.

The lattice strains for the aluminium alloy AA6016-T4 with the *fcc*-structure are evaluated for the lattice planes (111), (200), (220), (311), (400) and (331). During the elastic deformation, the lattice strains increase monotonically. As soon as the plastification starts, the lattice strains saturate. At the time of plastification, the atomic distance between the individual atoms has reached its maximum, and any further deformation leads to plastic deformation and can, therefore, not increase anymore.

For the IF0-PF0 specimens, see Figure 6.31 (a) and (c), the elastic-plastic transition is sharp and corresponds well with the onset of yielding determined by the temperature-based methods.

The $YS_{0.2\%}$-method depicts the onset of yielding beyond plastification. The different slopes of the individual lattice planes are caused by microstructural anisotropy. Each lattice plane has its own elastic constant, which are in the case of aluminium similar to each other (Eigenmann and Macherauch, 1996). Regardless of the individual elastic constant, all lattice planes can absorb almost the same amount of elastic strain.

On the contrary, the IF0-PF90 specimens show a completely different behaviour. The individual lattice planes and even individual grains yield at very different stresses. Also, the elastic-plastic transition of those planes is slower than observed for the IF0-PF0 specimens. This transition behaviour is also represented by the temperature signal with its round appearance. After the elastic-plastic transition, some lattice planes still show an increase in the lattice strain. Some lattice planes can, therefore, still absorb elastic strain. The two lattice planes (200) and (400) are multiples and hence must show similar behaviour as they do in the case of the investigated material. The curves are almost identical for those two lattice planes.

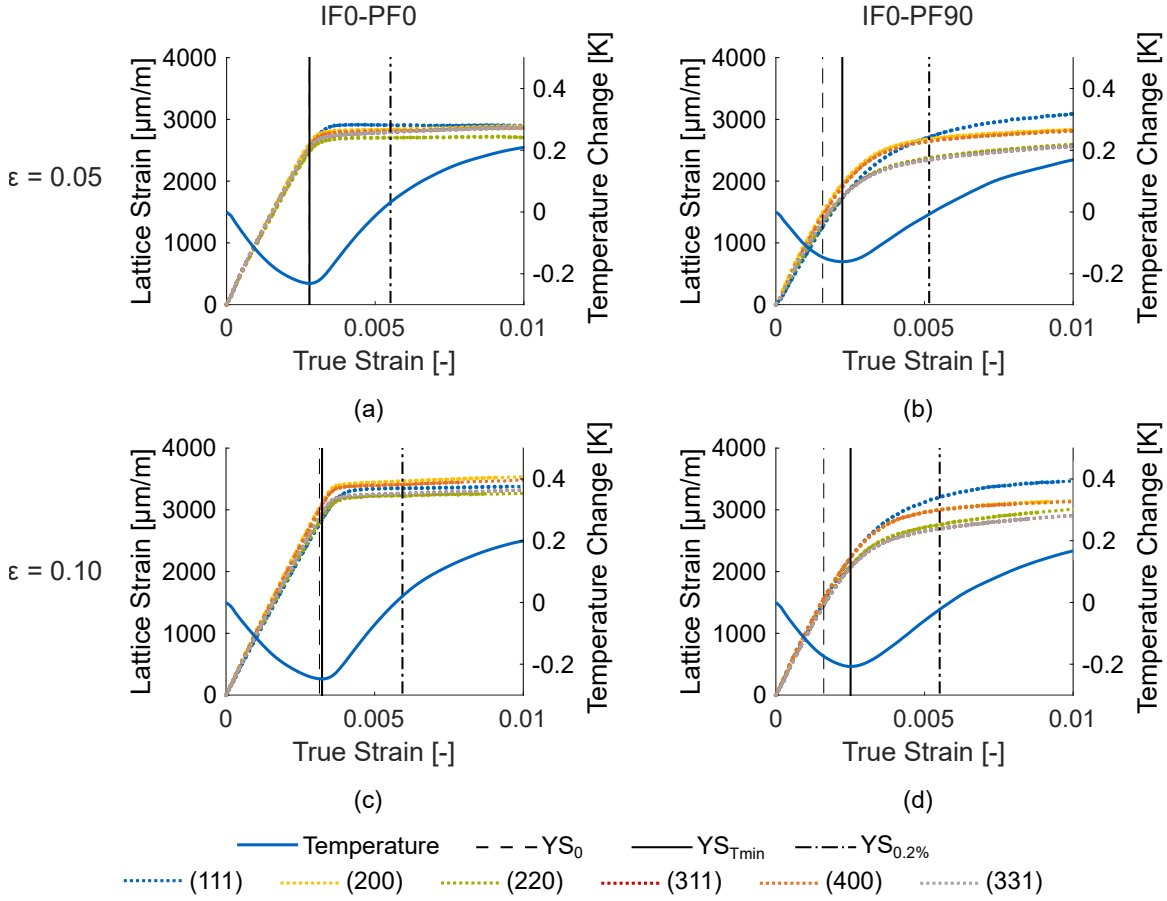

Figure 6.31: Lattice strains of the AA6016-T4 with the configurations IF0-PF0, $\epsilon_{pre} = 0.05$ (a), IF0-PF90, $\epsilon_{pre} = 0.05$ (b), IF0-PF0, $\epsilon_{pre} = 0.10$ (c) and IF0-PF90, $\epsilon_{pre} = 0.10$ (d).

As described in section 2.2.1, different lattice planes are visible in synchrotron diffraction experiments, depending on the crystallite structure. Due to the *bcc*-structure of the steels, the lattice planes (110), (200), (211), (220) and (310) are further investigated.

The observed lattice strains show similar behaviour for the steel as for the aluminium alloy. A proportional load path leads to almost simultaneous plastification, regardless of the lattice plane, see Figure 6.32 (a) and (c).

A change of the loading direction by 90° (IF0-PF90), on the other hand, leads to a clearly different course of the lattice strain, see Figure 6.32 (b) and (d). As with aluminium, it is evident that the lattice planes plasticise at significantly different stresses. In comparison to the aluminium alloy, the deviation from linearity happens at even lower strains.

As for the lattice planes (200) and (400) in *fcc*-structures, the lattice planes (110) and (220) are again multiples for the *bcc*-structures. The curves of those lattice planes hence have to show similar results.

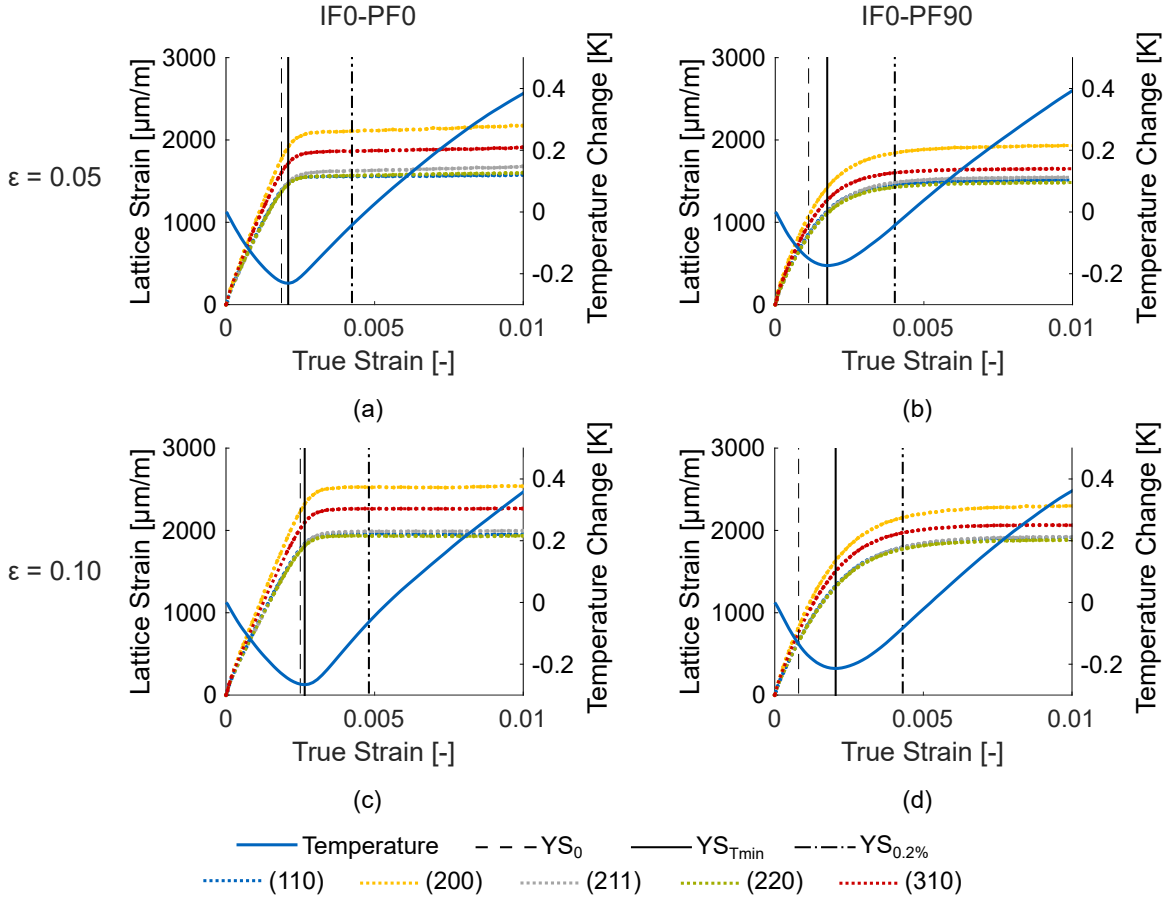

Figure 6.32: Lattice strains of the HC340LA with the configurations IF0-PF0, $\varepsilon_{pre} = 0.05$ (a), IF0-PF90, $\varepsilon_{pre} = 0.05$ (b), IF0-PF0, $\varepsilon_{pre} = 0.10$ (c) and IF0-PF90, $\varepsilon_{pre} = 0.10$ (d).

The individual lattice planes show an even more anisotropic behaviour than the lattice planes of the aluminium alloy. The elastic constants of the individual lattice planes differ even more for the HC340LA steel. Also, the capability to absorb strains is much more different. While for the aluminium alloy, every investigated lattice plane has more or less the same capability, the lattice planes (200) and (310) for the steel material have a much higher capability to absorb elastic strains. The results for the DP600 are shown in the appendix in section D.3.

In conclusion, the temperature-based determination of the yield stresses by YS_{Tmin} and YS_0 is an effective way to determine the physical onset of yielding. The yield strength could be determined precisely for samples with a smooth elastic-plastic transition. The plastification of individual lattice planes could verify the determined yield stresses. In contrast, applying the classical $YS_{0.2\%}$ method leads to a significant overestimation of the onset of yielding and, therefore, to significantly higher yield stresses for specimens with a smooth elastic-plastic transition. The use of temperature-based methods is recommended for such specimens.

6.3.2 Determination of the Dislocation Density

As stated in section 2.4.2, dislocations are greatly affected by non-proportional load paths. In order to evaluate the effect of orthogonal loading on the dislocations, the dislocation density is evaluated. Additionally, the dislocation density is another possibility to determine the onset of yielding. The dislocation density and yield strengths determined by the three methods are depicted in Figure 6.33 for the AA6016-T4. Below the onset of yielding, no increase in the dislocation density occurs as plastic deformation is required to increase the number of dislocations. After the first plastic deformation, an increase is observed for the IF0-PF0 specimens. This increase is caused by the activation of new slip systems. The increase of the dislocation density is also visible in the two different starting densities. The inital density of the $\varepsilon_{pre} = 0.05$ specimens is below that from the $\varepsilon_{pre} = 0.1$ specimens.

For the IF0-PF90 specimens, a different behaviour can be seen. With the onset of plastification, a slight decrease in the dislocation density is found. After a certain decrease, the dislocation density starts to increase again, as observed for the IF0-PF0 specimens. The beginning of the slight decrease correlates well with the onset of yielding determined by the YS_0-method. The $YS_{0.2\%}$-method depicts the onset of yielding at higher stresses and after the first clearly visible increase in the dislocation density.

For the steels, a slight decrease of the dislocation density can be observed for the IF0-PF0 specimens in Figure 6.34 (a) and (c) in the elastic region. This decrease is caused by annihilation

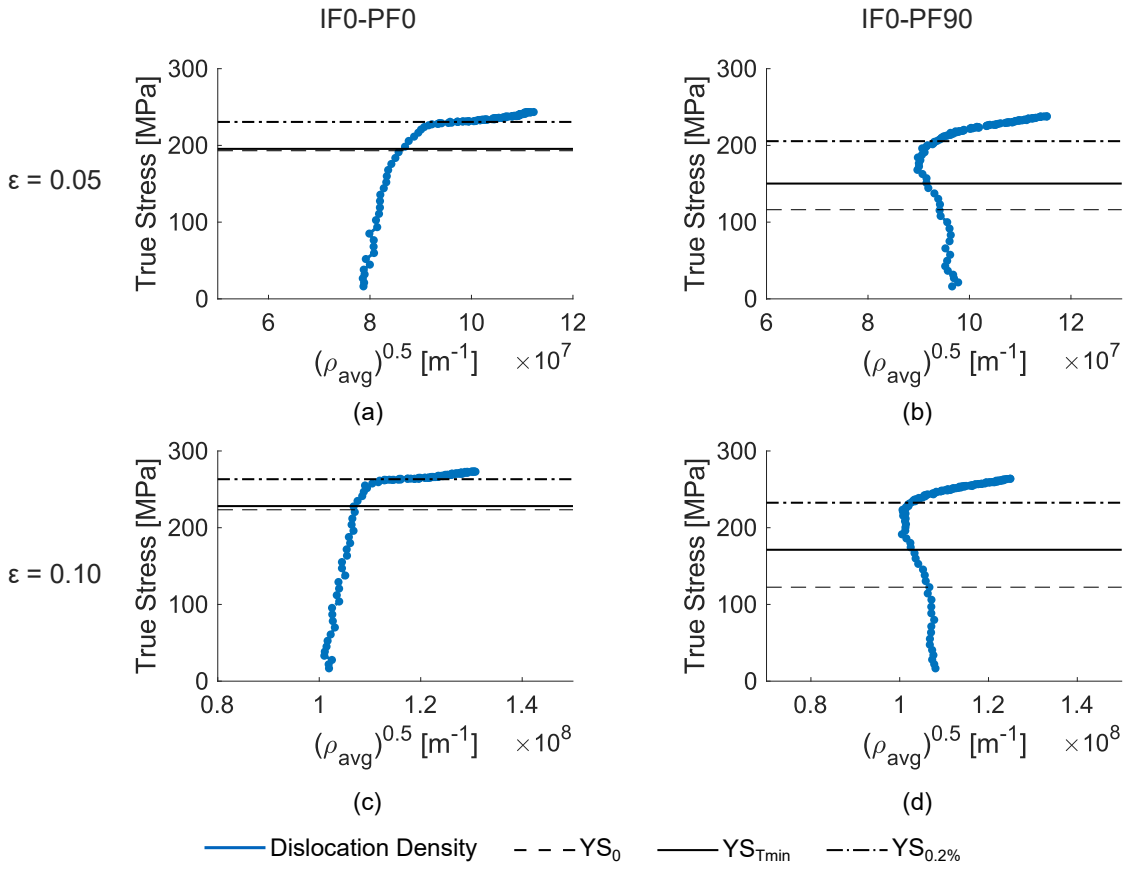

Figure 6.33: Dislocation density of the AA6016-T4 with the configurations IF0-PF0, $\epsilon_{pre} = 0.05$ (a), IF0-PF90, $\epsilon_{pre} = 0.05$ (b), IF0-PF0, $\epsilon_{pre} = 0.10$ (c) and IF0-P9F0, $\epsilon_{pre} = 0.10$ (d).

of dislocations with opposing directions. The higher the pre-forming level, the higher the annihilation is. This effect was not observed for the aluminium alloy.

The behaviour of the IF0-PF90 specimens is different to that of the IF0-PF0 specimens. A strong decrease after the onset of yielding is visible, see Figure 6.34 (b) and (d). This decrease is higher for the specimens with a pre-forming level of $\epsilon_{pre} = 0.1$. For the HC340LA specimens, localisation occurs before the dislocation density has reached its starting value again.

This strong decrease in the dislocation density in the longitudinal is not visible in the transversal direction, see Figure 6.35. The dislocation densities in the transversal direction remain almost constant until the specimen is fully plasticised. The different behaviour of the dislocations leads to the conclusion that the pre-forming leads to the creation of dislocation structures inside the grains. Those structures have a preferred orientation, depending on the activated slip system. Therefore, a cross-loading activates different slip systems which now weaken the existing dislocation structures, while new dislocations are created due to the plastic deformation.

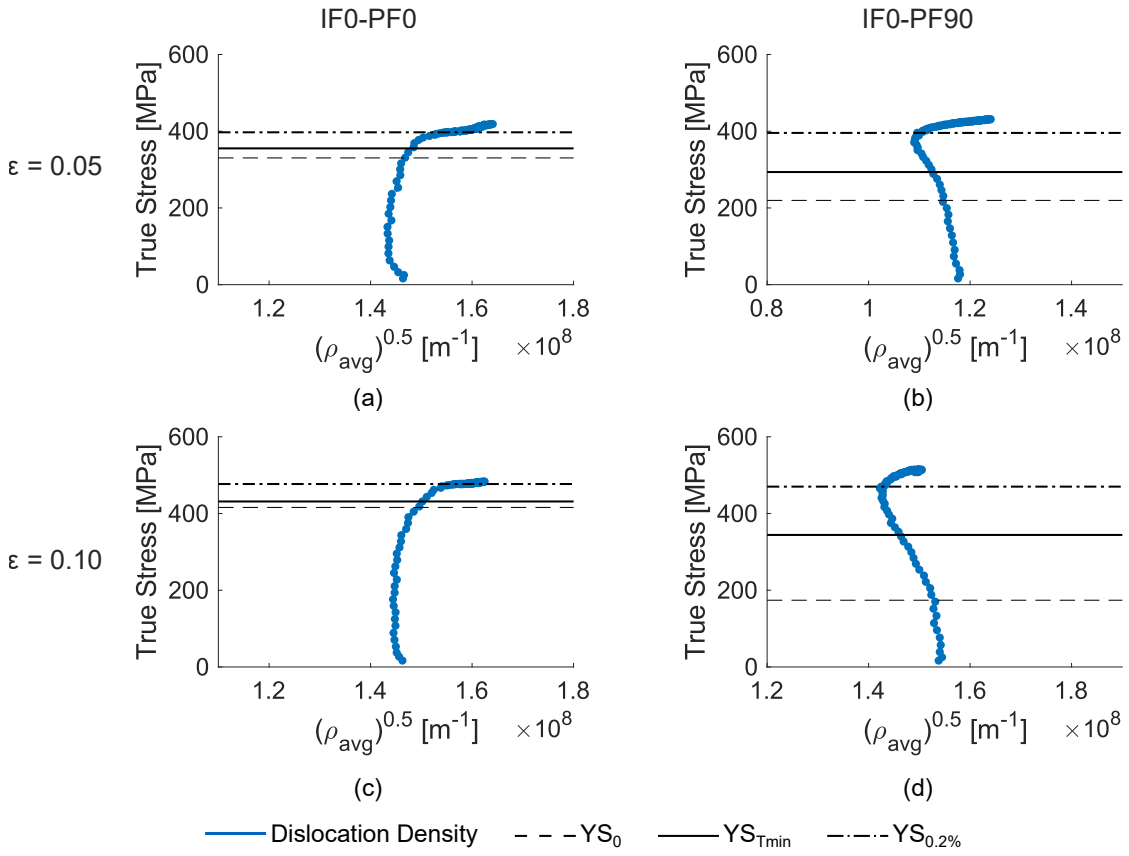

Figure 6.34: Dislocation density of the HC340LA with the configurations IF0-PF0, $\epsilon_{pre} = 0.05$ (a), IF0-PF90, $\epsilon_{pre} = 0.05$ (b), IF0-PF0, $\epsilon_{pre} = 0.10$ (c) and IF0-PF90, $\epsilon_{pre} = 0.10$ (d).

The results for the DP600 are shown in the appendix in section D.4 and D.5.

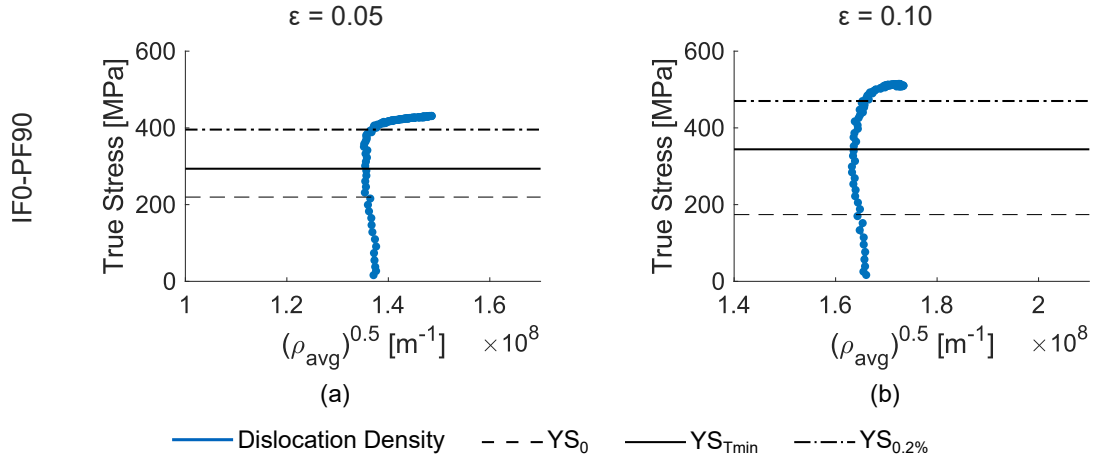

Figure 6.35: Dislocation density of the HC340LA with the configurations IF0-PF90, $\epsilon_{pre} = 0.05$ (a), IF0-PF90, $\epsilon_{pre} = 0.1$ (b) in the transversal direction.

Using EBSD, the structure of the GNDs can be visualised. By investigating the HC340LA steel at different strain levels, the development of the GND structures can be calculated. The resulting maps are presetned in Figure 6.36. for the initial state, the amount of GNDs is quite low. After pre-forming, a increase of the dislocations is observed. The dislocations show a banded structure. If the specimen is reloaded in the same direction (IF0-PF0) until uniform elongation, these structures have an increased density. For the IF0-PF90 a different behaviour is observed. The dislocation density is only marginal increased after reloading until uniform elongation. Also the banded structure of the dislocations is not visible anymore.

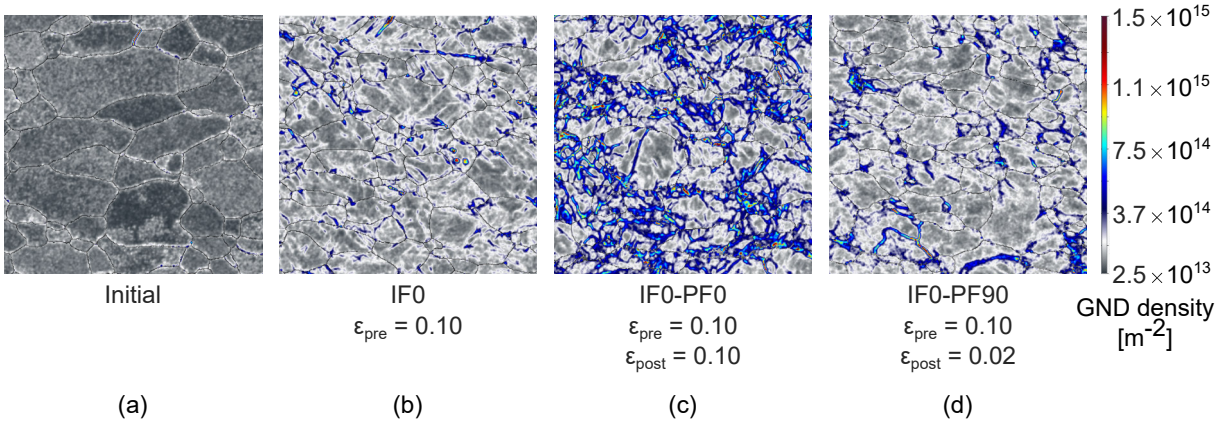

Figure 6.36: GND structures of HC340LA in various pre-forming states, initial (a), $\varepsilon_{pre} = 0.1$ (b), IF0-PF0 (c) and IF0-PF90 (d) at the time of maximum force.

When looking at the total dislocation density obtained by EBSD, the same behaviour as for the synchrotron experiments is found. The dislocation density increases with increasing strain if the loading direction is kept constant, see Figure 6.37 (a)-(c). If the loading direction is changed by 90°, there is only a small increase in the dislocation density at the time of the uniform elongation, see Figure 6.37 (d). This leads to the conclusion, that the banded dislocation structures which form during the pre-forming under 0° to the initial RD (IF0) are weakened at the beginning of the deformation during the reloading under 90° (PF90). With increasing strain, new structures form leading to the small increase in the dislocation density. In order to avoid that the investigated area represents an outlier, two measurements were carried out for each configuration.

The dislocation density obtained by EBSD has the unit m^{-2}, while the dislocation density obtained by the Williamson-Smallman model has the unit m^{-1}. Hence, the values between the two ways to determine the dislocation density differ.

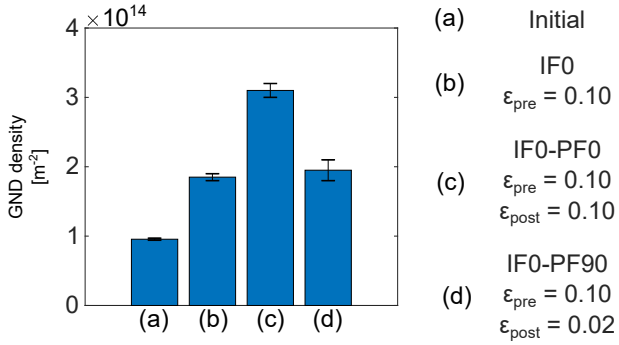

Figure 6.37: GND density of HC340LA in various pre-forming states, initial (a), $\varepsilon_{pre} = 0.1$ (b), IF0-PF0 (c) and IF0-PF90 (d) at the time of maximum force.

6.3.3 Texture Analysis

The texture analysis allows conclusions about the evolution of the microstructure during deformation. The tensile tests for the bi-linear load paths were stopped when the maximum force, hence the uniform elongation, was reached. The specimens were unloaded again and prepared for texture analysis, as shown in section 5.2.2. This process was done in the same way for all three investigated materials.

For the AA6016-T4 the texture at four different deforming levels and three Euler sections $\varphi_2 = 0°$, 45° and 60°, is presented in Figure 6.38. The material shows a strong cube component $\{001\}\langle100\rangle$ in all four states, which is clearly visible in the Euler section $\varphi_2 = 0°$. Such a texture is typical for a recrystallization texture of an AA6016-T4 alloy (Engler, 2022). In that section also, the development of a brass-component $\{001\}\langle211\rangle$ is visible. This component shows an increased strength with increased deformation, regardless of the loading direction. For the IF0-PF0 state (see Figure 6.38 (c)), an increased copper component $\{112\}\langle111\rangle$ and R component $\{124\}\langle211\rangle$ is present in the Euler section $\varphi_2 = 45°$ and $\varphi_2 = 60°$.

The evolution of the copper and brass components are also found. Their development is dependent on the number of active slip systems. Fewer slip systems lead to slower development of those components. These two components vanish during the orthogonal loading of the material. Overall, the cubic texture is increased with increasing strain, and orthogonal loading does not lead to a substantial texture evolution. The findings of this study are in good agreement with the findings of Delannay et al. (2002). Here, investigations using two different aluminium alloys also revealed that the cube-component remains strong throughout the deformation.

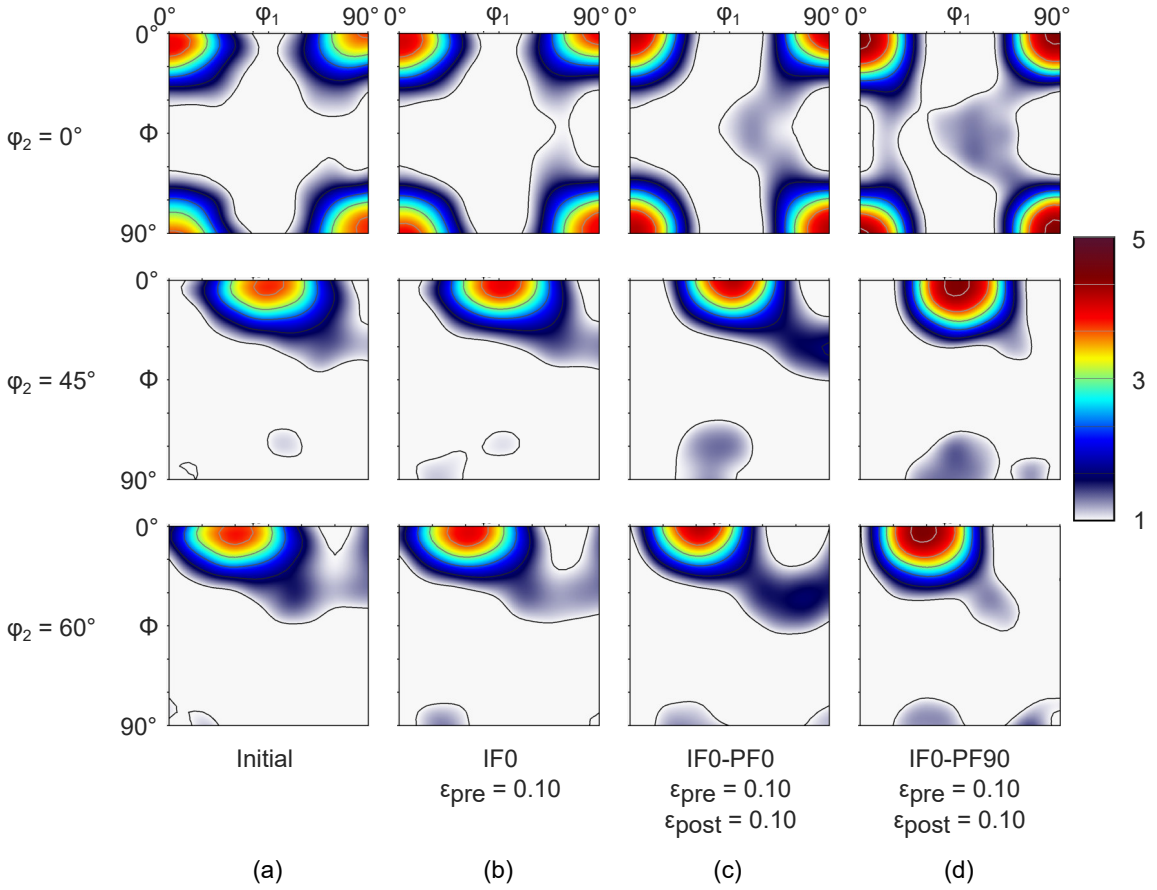

Figure 6.38: Texture of AA6016 in various pre-forming states, initial (a), $\varepsilon_{pre} = 0.1$ (b), IF0-PF0 (c) and IF0-PF90 (d) at the time of maximum force.

For the steels, only the Euler section $\varphi_2 = 45°$ is analysed, which is sufficient for a *bcc*-structure (Kestens and Pirgazi, 2016). The γ-fiber is depicted as the red line in Figure 6.39.

Both steels show a strong α- and γ-fiber texture, increasing with increased deformation. The α-fiber is parallel to RD, while the γ-fiber is parallel to ND. The materials have a typical cold-rolled texture. A typical cold rolled *bcc*-texture is composed by a strong α-fiber running from $\{001\}\langle 110\rangle$ to $\{111\}\langle 110\rangle$ and a strong γ-fiber running from $\{111\}\langle 110\rangle$ to $\{111\}\langle 112\rangle$ (Kestens and Pirgazi, 2016).

An increased deformation leads to an increase in the E-component $\{111\}\langle 110\rangle$ and a rotated cube component $\{111\}\langle 011\rangle$ which both lay on the γ-fiber. While the other two components along the γ-fiber, $\{111\}\langle 121\rangle$ and $\{111\}\langle 112\rangle$, are decreasing. The two components, $\{111\}\langle 110\rangle$ and $\{111\}\langle 011\rangle$ as well as $\{111\}\langle 121\rangle$ and $\{111\}\langle 112\rangle$, are equivalent points by symmetry (Creuziger et al., 2014). The E-component is particularly strong after orthogonal loading.

Along the α-fiber, the components $\{112\}\langle 110\rangle$ and $\{223\}\langle 110\rangle$ are strongly developed. After orthogonal loading, a texture shift from the α-fiber towards the α^*-fiber is observed.

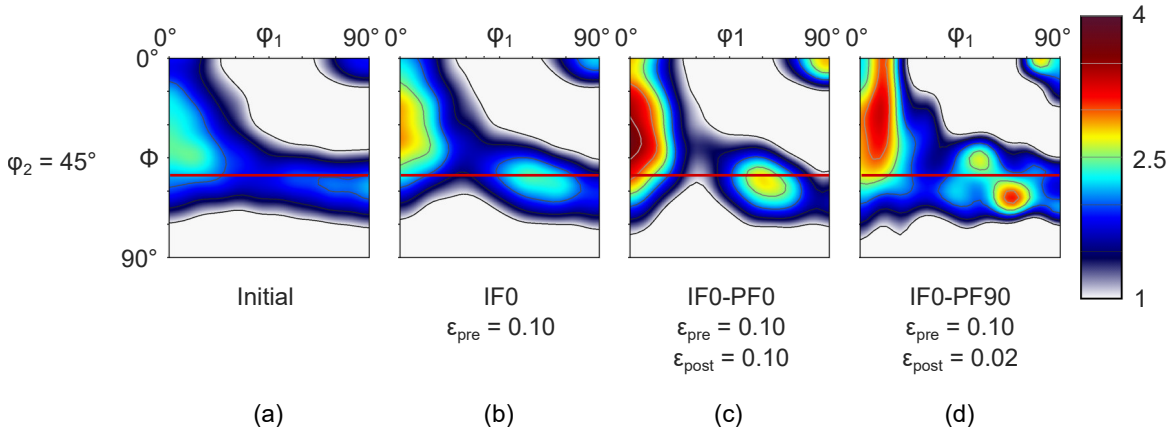

Figure 6.39: Texture of HC340LA in various pre-forming states, initial (a), $\varepsilon_{pre} = 0.1$ (b), IF0-PF0 (c) and IF0-PF90 (d) at the time of maximum force.

The texture of the DP600 steel is generally lower than that of the HC340LA steel, meaning that the DP600 has a more randomly distributed microstructure. The general evolution of the texture is, similar to that of the HC340LA steel. Nevertheless, the DP600 has a slight Rotated Goss component $\{011\}\langle 011\rangle$, which develops with increasing strain. This component is not observed for the HC340LA steel.

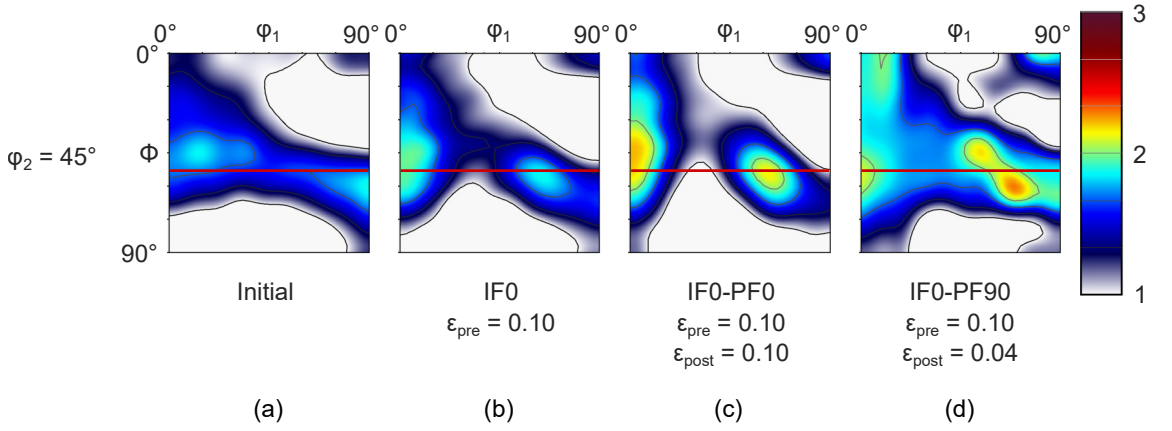

Figure 6.40: Texture of DP600 in various pre-forming states, initial (a), $\varepsilon_{pre} = 0.1$ (b), IF0-PF0 (c) and IF0-PF90 (d) at the time of maximum force.

The texture evolution is marginal after investigating the texture development of the three materials. The findings of Vrettou et al. (2022), where the loss of formability after pre-forming and

orthogonal loading of a mild DX54 steel is attributed to the texture evolution, could not be verified for the two steel grades. But texture evolution can play a role at higher pre-forming levels, as Barlat et al. (2003) found for an aluminium alloy AA1005. In this study, the pre-forming was done by shear specimens and levels up to $\varepsilon = 0.3$, which is significantly higher than the pre-forming level investigated in the microscopic experiments in this study.

6.3.4 Nanoindentation Experiments

For the nanoindentation experiments, the materials were pre-formed and compared to the material in the as-received state. By putting the indenter at grain centers and grain boundaries, respectively, the differences in between those two areas could be investigated. At least ten indents in each area are evaluated to achieve a sufficient statistic.

The DP600 steel, with its two phases and a small grain size in combination with the used radius of the indenter led to problems in the evaluation. No clear distinction could be made between the indents in the grains, the martensite islands and the grain boundaries. Therefore, the DP600 was not evaluated.

For the aluminium alloy in the as-received state, the grain boundaries show a higher hardness compared to that in the grain center, see left side of Figure 6.41. The difference between the two areas is quite small compared to the HC340LA steel for the as-received material. With increasing strain, the grain centers become harder than the grain boundaries but they differ only marginally.

The steel grade HC340LA shows a different behaviour. In the as-received state, the grain boundaries are harder than the grain centers. For this material the grain boundaries show a higher increase in strength than the grain centers, see right side of Figure 6.41. The difference between the two areas is therefore increasing. This can be explained by the increased dislocation density at grain boundaries. Grain boundaries are obstacles to the dislocation movement. Hence, a dislocation pile-up takes place at the grain boundaries. A higher dislocation density leads to an increase in force which is required to deform the material.

The material and even the grains of the HC340LA have a strength gradient and are no longer homogenous. This inhomogeneity increases with increasing strain. On the other hand, the aluminium alloy becomes more homogeneous with increasing strain.

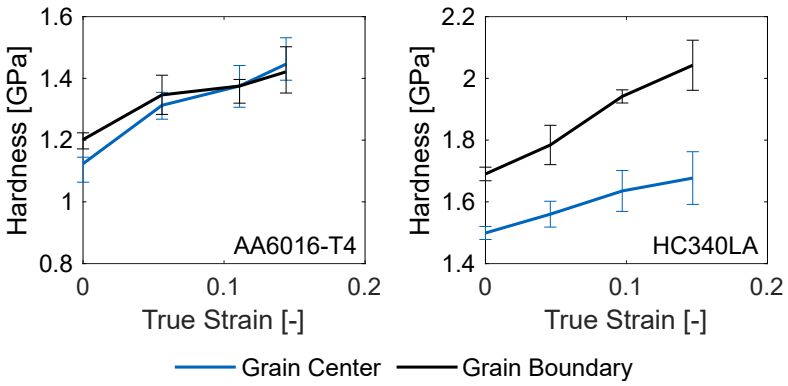

Figure 6.41: Nanohardness of the grain center and the grain boundary of the AA6016-T4 and the HC340LA for different pre-forming levels.

6.3.5 SEM Microscopy

Microstructure

For different pre-forming levels, the microstructure has been investigated using SEM microscopy. SEM microscopy allows a close look at the evolution of the grain deformation and the presence of voids or other signs of damage.

The aluminium alloy AA6016-T4 shows many randomly distributed non-metallic inclusions, visible as white sharp-edged structures. These inclusions differ significantly in shape and size. The machining process causes the holes around the inclusions and within grains during the polishing of the surface. The mechanical grinding and polishing process loosens hard inclusions and leaves holes within the grains. Overall, no damage is visible for the aluminium alloy AA6016-T4.

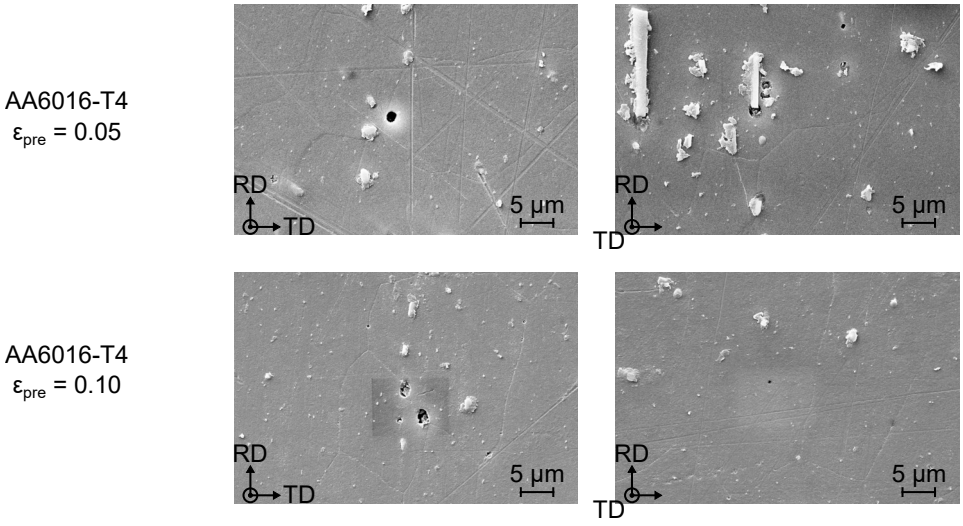

Figure 6.42: SEM images of the AA6016-T4 for different pre-forming levels and orientations.

For the dual-phase steel, the martensite grains are clearly visible as grey areas in Figure 6.43. As for the aluminium alloy, no damage is visible after pre-forming up to $\varepsilon_{pre} = 0.1$. Therefore, no voids or cracked martensite grains are found in the microstructure.

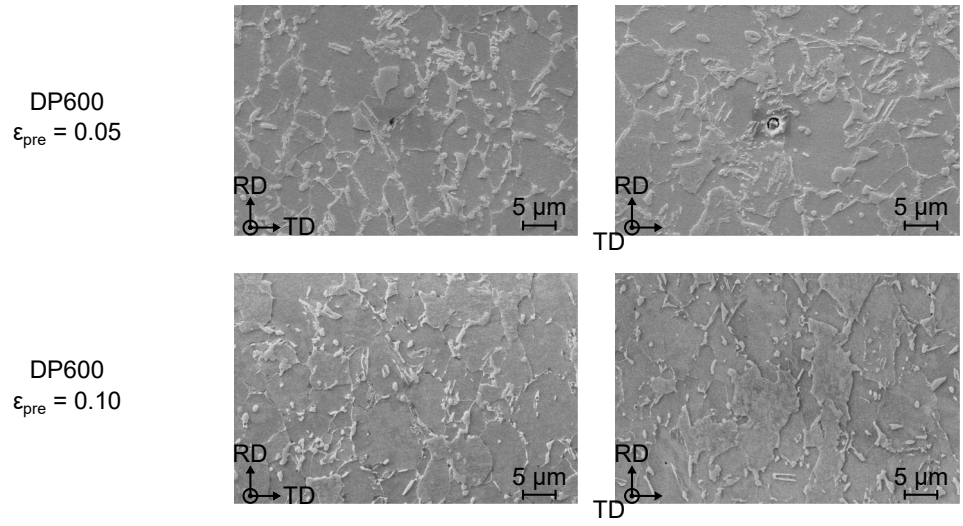

Figure 6.43: SEM images of the DP600 for different pre-forming levels and orientations.

Within the microstructure of the HC340LA an alignment of the grains in the loading direction at $\varepsilon_{pre} = 0.1$ is observed. The white dots are coagualted cementite which is dispersed in the microstructure. With increasing strain, also those inclusions are alinged in the loading direction. The HC340LA steel is the only material which shows some slight damage after pre-forming.

Those areas are marked with red arrows. Nevertheless, the damaged areas and the observed voids are small and only visible with a sufficient maginification using SEM microscopy.

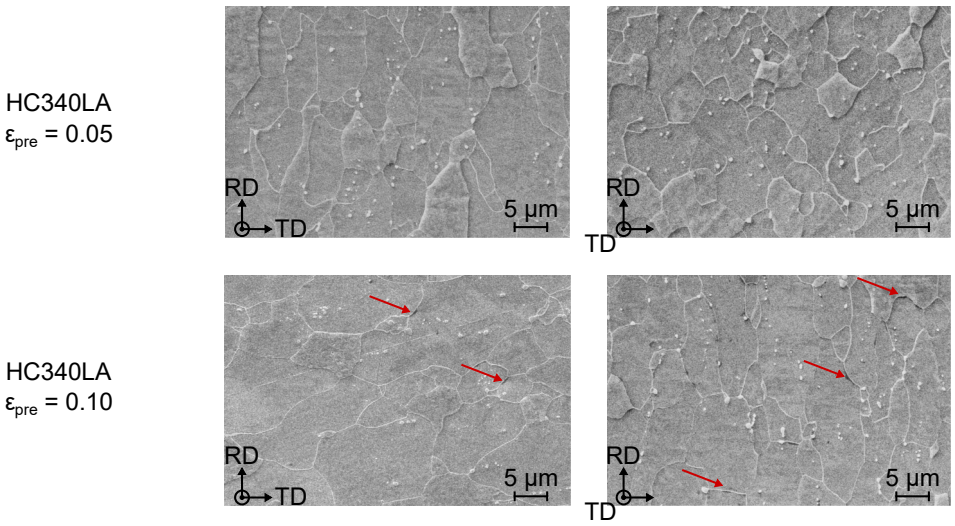

Figure 6.44: SEM images of the HC340LA for different pre-forming levels and orientations.

Fracture Surface

During failure of the material, void growth is significantly increased. The size and the shape of the voids is dependent on the applied stress state during failure. The fracture surfaces of the materials differ significantly.

While the aluminium alloy shows a brittle fracture with almost no signs of ductile fracture like small dimples, the steels show a ductile fracture behaviour. The pre-forming and especially a change in the loading direction lead to different failure mechanisms.

For the Nakajima specimens, the IF0-PF0 of the aluminium alloy and the IF0-PF90 show almost similar fracture surfaces. Due to the quite brittle fracture, only small dimples evolve during failure and a highly fissured surface forms.

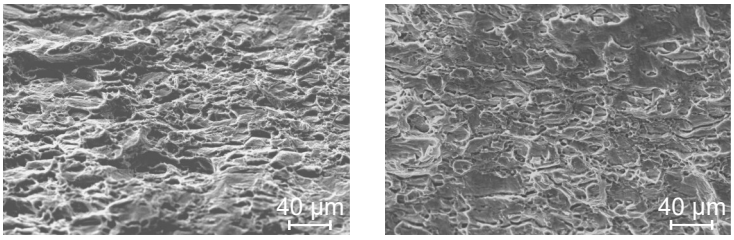

Figure 6.45: SEM images of the fracture surface of AA6016-T4 for the uniaxial Nakajima specimens with the 50 % pre-forming level.

On the other hand, a significant difference can be observed for the steels. The IF0-PF0 specimens show a ductile failure with many small dimples caused by void growth and coalescence. Coagulated cementite is visible on the ground of some dimples, concluding that the non-metallic inclusions are nucleation sides of voids. The IF0-PF90 specimens show a significantly increased void size. Some voids reach up to 20 μm in diameter. These increased voids are characteristic of shear failure mechanisms. During the shear process, the void size can increase rapidly.

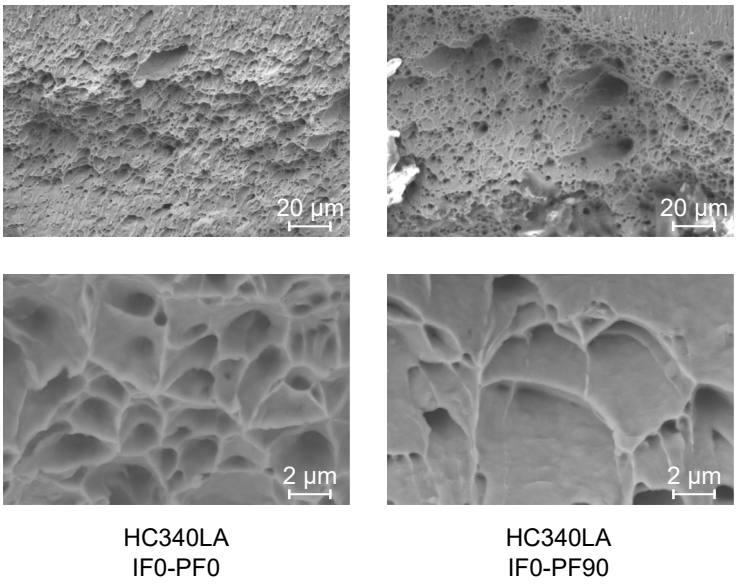

Figure 6.46: SEM images of the fracture surface of HC340LA for the uniaxial Nakajima specimens with the 50 % pre-forming level.

In between the voids of the IF0-PF90 specimens, the dimples show a parabolic apperance. Such parabolic dimples were observed in shear failure mechanisms for other materials like Ti-6Al-4V as well (Pineau et al., 2016).

7 Interpretation of the Results and Transfer

The results of the conducted experiments on a macroscopic and microscopic scale have been presented in Chapter 6. The aim of the experiments conducted was to further investigate the effects of non-proportional load paths in combination with a change in loading direction on the mechanical behaviour of three different sheet metals. In the following chapter, the findings are further discussed.

7.1 Interpretation of the Experimental Results

The results have shown that not all materials are sensitive to a change in the loading direction. For example the investigated aluminium alloy AA6016-T4. This material is only marginally influenced by a change in the loading direction with regard to formability. Nevertheless, the shape of the flow curve is influenced. This material showed a permanent softening behaviour.

On the other hand, the steels are sensitive to a change in the loading direction. After a certain pre-forming level, the formability is significantly reduced. This effect is the most pronounced when a post-forming on the left-hand side of the FLC took place. The loss of formability is combined with a stress overshoot in the flow curve shortly after the onset of plastification.

The flow curves from the tensile tests show that the following equation is fulfilled before the diffuse necking begins:

$$\frac{\partial \sigma}{\partial \varepsilon_1} + \frac{\partial \sigma_1}{\partial \beta} \frac{\partial \beta}{\partial \varepsilon_1} \geq \sigma_1 \quad . \tag{7.1}$$

At the time of the onset of diffuse necking, this equation is no longer satisfied and the Considère criterium is fulfilled, see equation 2.11. This criterion is valid for homogeneous materials with a classical necking behaviour over the thickness, such as the specimens with a *Type I* failure mode. The samples with reduced formability and a *Type II* failure mode show a softening behaviour with an almost constant decrease in stress after necking in the tensile experiments. Looking at the results of the fracture surfaces as well as the microstructure during the tests, a clearly increased pore growth can be seen for these samples. It is now assumed, that the material

still shows a hardening behaviour but the increased void growth rate leads to a global softening behaviour. The current cross-section of the material is therefore calulated the following,

$$A_{local} = A - A_{voids} \quad . \tag{7.2}$$

This means that the stress is locally higher than the global observation in the tensile test. The following criterion is therefore proposed for the samples with a type II failure mode at the time of localisation,

$$\frac{d\sigma}{d\varepsilon} \leq 0 \quad , \tag{7.3}$$

where σ is the true stress and ε the true strain. A further investigation of the macroscopic findings was done by using synchrotron diffraction experiments. These experiments revealed that the material behaviour after a change in loading direction by 90°, or orthogonal loading, is becoming inhomogeneous. The individual grains start to yield at different stress levels. Also, the dislocation density starts to decrease after plastification.

The cause for the observed material behaviour is found in the microstructure. During pre-forming, dislocations start to form dislocation walls with a high dislocation density. These dislocation walls were observed using EBSD for the HC340LA steel, see Figure 6.36 (b). The dislocation walls are aligned in the direction of the activated slip systems. With increasing strain, the dislocation density increases and further walls start to form as shown in Figure 6.36 (c). Next to the dislocation walls, dislocations are piled-up at the grain boundaries, leading to an increase in nanohardness for the HC340LA steel. Such an increase in nanohardness was not observed for the aluminium alloy AA6016-T4. For this material, the grain centers showed a higher increase in strength compared to the grain boundaries, see Figure 6.41.

When the loading direction is changed, the existing dislocation walls are weakened, or even extinguished and new dislocation walls start to form in the direction of the newly activated slip systems. For the HC340LA steel the banded structure of the dislocations vanishes and new structures form, see Figure 6.36 (d). In order for dislocations to be annihilated, two dislocations with opposing signs have to meet. To make such an encounter possible, dislocations have to move. For *bcc*-materials, the dislocation motion is related to dislocation core properties (e.g. Peierl's stress). The *fcc*-materials dislocation motion is based on phonon drag and is affected by various collective phenomena (Fan et al., 2021). The movement within *bcc*-materials seem to be easier, and therefore a higher annihilation rate is observed, see Figure 6.34 and D.3.

During this annihilation process, the hardening rate is reduced and premature macroscopic instability occurs, which is caused by the microscopic processes. The cause for the reduced hardening rate is due to the movement of dislocations. This movement leads to plastic deformation and the release of large stresses (Zhuang et al., 2019). The dislocation walls must have sufficient dislocation density for microscopic instability to occur. This is only the case after a certain level of plastic deformation. This level is at approximately $\varepsilon_{pre} = 0.08$ for the steel grades. This annihilation process is also time-dependent. With less available time, the annihilation can not take place in a sufficient amount and no equilibrium is reached. This leads to an increase in formability when the strain rate is increased for the *bcc*-materials which showed a dependency of the formability on a change in the loading direction.

With macroscopic instability, the failure of the material begins. As shown using SEM, the HC340LA steel, which is the most sensitive material investigated regarding a change in loading direction, shows some small voids after pre-forming. In combination with the microplastic processes, shear failure occurs. This shear failure has a characteristic fracture surface. The fracture surface shows large pores on the one hand and parabolically shaped dimples between the pores. Such a fracture surface could be observed for the HC340LA and the DP600 steel. The observed fracture surface for steels requires sufficient ductility. Otherwise, such voids can not form. The aluminium fracture surfaces look the same regardless of the pre-forming level or the loading direction. The fracture surface is dominated by brittle fracture mechanisms with almost no voids or dimples. These findings are in good agreement with the observed occurrence of shear failure.

The loss of formability caused by premature microscopic instability is, therefore, the result of processes on the nano- or microscale inside the material. These processes, like the development of dislocation walls, increased GNDs at the grain boundaries or dislocation movement, depend on the material's microstructure. This leads to the conclusion that not all materials are dependent on a change in the loading direction.

7.2 Development of a Phenomenological Model

Different models exist to predict failure after complex load paths as stated in section 3.1. The results of the investigations show that the causes for the dependence of formability on the direction of loading after pre-forming depend on numerous reasons. It is also shown that the assumptions made by some models do not apply to such complex strain paths.

The eMMFC-model requires a change of the strain state to the plane-strain after necking. Specimens with a *Type II* failure mode do not show such a behavior, see Figure 6.18 and 6.23. Other models are isotropic such as the the Bao-Wierzbicki model, which uses invariants, or the GISSMO-model. The anisotropic behaviour of the forambility of the material is not covered by such models. The stress-based models require a very precise description of the material behaviour. Especially the hardening behaviour must be reproduced very precisely. The model must be able to reproduce the permanent softening behaviour of the aluminium alloy or the stress-overshoot of the steel materials. A hardening model which is capable to cover non-isotropic and kinematic hardening is required. This leads to a higher experimental effort in the material characterisation.

To avoid the problems mentioned prior, phenomenological models can be used. In this case, it is not necessary to understand all occuring mechanisms, such as dislocation movement or dislocation annihiliation, in detail in order to make predictions about the material behaviour or failure.

The GFLC model, presented in section 2.5.3, is able to predict the deformation capacity in non-proportional load paths without changing the loading direction. Due to its modular structure, the model can be supplemented with further parameters with little effort. In the case of the load paths investigated in this work, this is the change in the direction of loading. Instead of a linear Lagrange interpolation of a 4-node element, a linear interpolation of an 8-node element is now required. The differences between the GFLC and the 3D-GFLC are schematically shown in Figure 7.1.

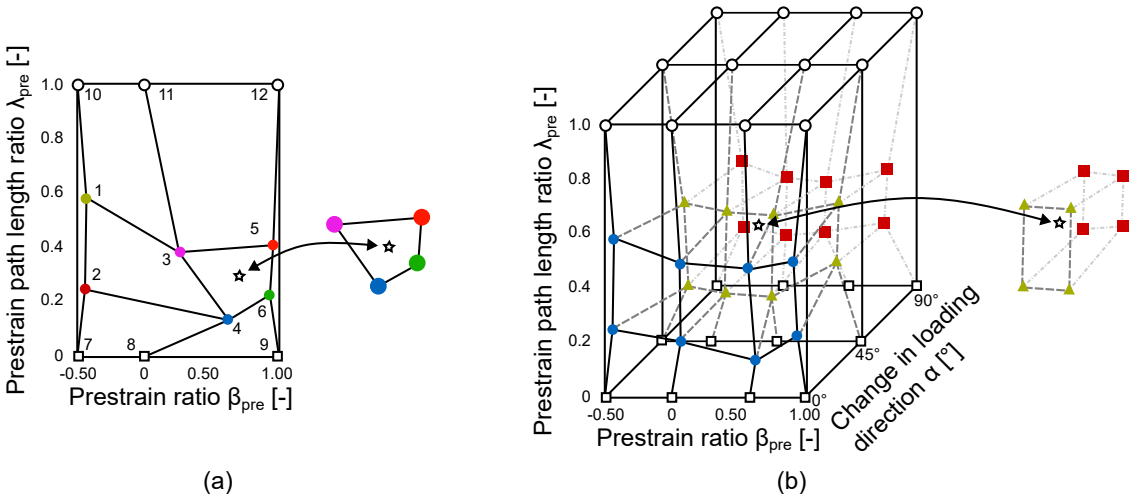

Figure 7.1: Differences between the GFLC (a) and the 3D-GFLC (b).

As for the GFLC model, an experimental database is also required for the 3D-GFLC model. However, since the influences of a change in the loading direction for different pre-forming levels must also be investigated here, the database is much more comprehensive. Three directions, IF0, IF45 and IF90, are already required for the initial pre-forming. From the pre-formed specimens, specimens are again taken in three directions, PF0, PF45 and PF90. The pre-forming states are the uniaxial, the plane-strain, the biaxial and an intermediate state in between the plane-strain and the biaxial state. In total, this results in 600 experiments. The different pre-forming levels for the HC340LA steel are presented in Figure 7.2. Every single dot represents the pre-forming state for the following determination of the FLC for three different loading directions. Due to its isotropic behaviour, the biaxial pre-forming is done only for the IF0 specimens.

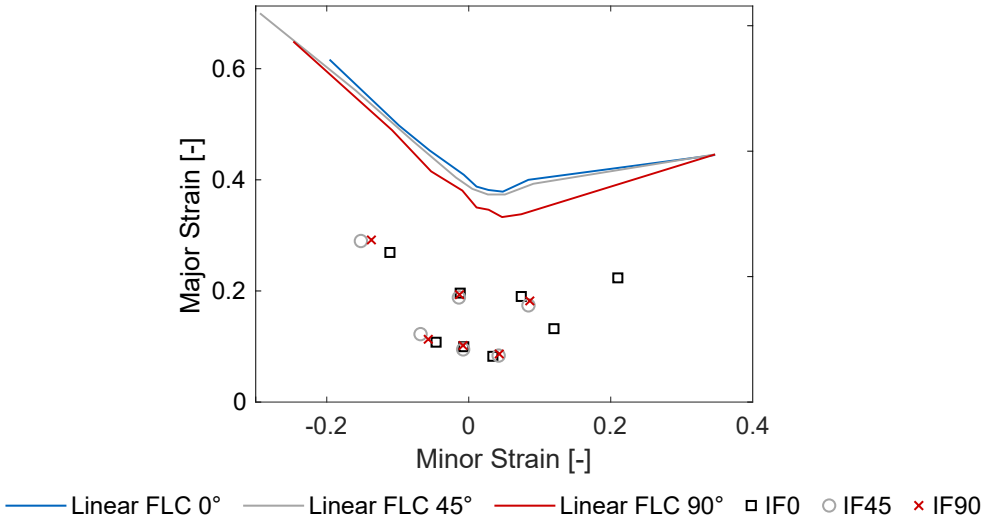

Figure 7.2: Pre-Forming states for the 3D-GFLC model.

The GFLC model is already implemented in the commercial FE software AutoForm. To implement further models or user-defined functionalities into AutoForm, the R&D plug-in can be used. This plug-in is available since the version R10. The implementation of such functionalities is done by using the programming language C. To compile the code Visual Studio is used. The resulting .dll file can be read by AutoForm R10.

Due to the implicit solver, only the current increment can be used for the calculations. For the implementation of the 3D-GFLC, the current strain increment, the loading ratio $\beta = \varepsilon_2/\varepsilon_1$ as the current loading angle α are needed from the simulation. The loading angle defines the loading direction of the last and current step with regard to the initial loading direction. In combination with the experimental database, the calculation of the failure variable λ is possible. Failure occurs as soon as $\lambda > 1$.

7.3 Industrial Application of the 3D-GFLC model

To validate the 3D-GFLC model, the industrial part presented in 3.1 is used. The material used in the presented part is a CR4 steel with excellent formability. The material is purely ferritic, as the HC340LA steel investigated in this thesis. The load path presented in 3.1 shows a sudden change in the loading direction after a plane-strain pre-forming. This pre-forming is caused due to the passing of the draw bead. As soon as the radius of the part is reached, the orthogonal loading of the material begins. The initial strain increment is under 90° to the initial loading direction. The notation of the specimens is IF90-PF90 for the specimens with no change in loading direction and IF90-PF0 for the specimens with a change in the loading direction by 90°. To prove if the sudden crack is caused by shear failure, the load path of the component is reproduced on a laboratory scale. For this purpose, the same experimental procedure was chosen as for the materials already investigated.

The initial FLCs under 0° and 90° to the initial rolling direction reveal that the investigated CR4 material has almost no anisotropic behaviour with regard to the formability, see the blue (0°) and red (90°) curve in Figure 7.3 (a). The specimens with no change in loading direction, IF90-PF90, are in good agreement with the initial FLCs, as expected when there is a proportional load path. The PF90-IF0 specimens show a significantly reduced formability, as observed for the other steel grades in this study. This reduced formability is also clearly visible when looking at the force-punch travel curves in Figure 7.3 (b). The deviation in between the individual investigated specimens is marginal. The load path of the industrial part can be accurately recreated with the experimental setup used.

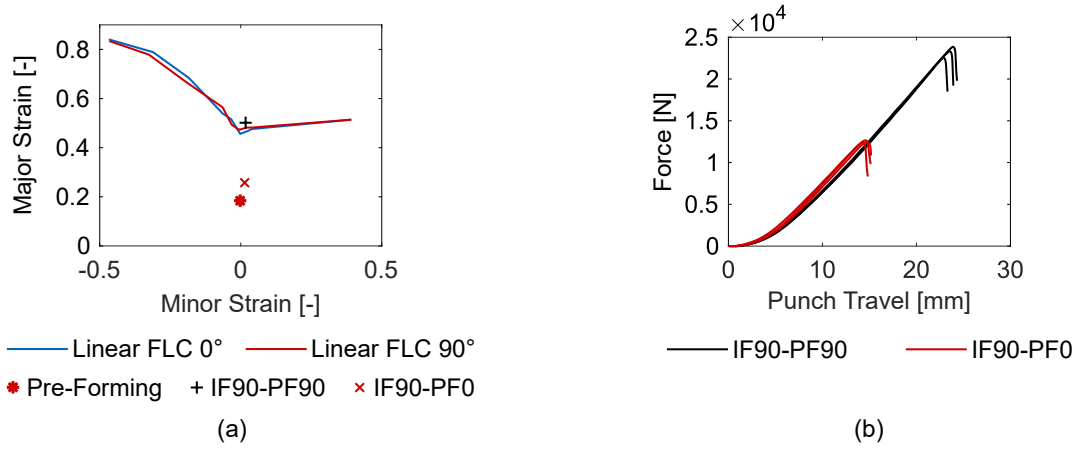

Figure 7.3: Influence of a plane-strain pre-forming and a change in loading direction on the formability (a) and the force-punch travel curves (b).

The experimental database of the HC340LA steel is used to predict the onset of localized necking for the CR4 steel part. This procedure is valid as both materials are purely ferritic and of the same material grade. To account for the different formabilities of the CR4 and the HC340LA steels, the formability is scaled. For the scaling process, the linear FLC is used as a basis. As the linear FLC of the CR4 lies above that of the HC340LA, the remaining formability is increased. Transferring the experimental results of the strains into the required format for the code is done manually in a different tool. Within this tool, the strains of each datapoint are converted into the values β, λ and α. The convertion is done in the same way as for the GFLC-model as described in section 2.5.3. These values are added manually to the code using a database.

After implementing and compiling the 3D-GFLC code, the simulations can be performed. For each step during the simulation, the results of the user-defined variables are calculated. Through this procedure, the evolution of the variables can be followed. The resulting failure variables at the final step of the simulation obtained by the linear FLC, the GFLC and the 3D-GFLC are compared to each other, see Figure 7.4. The failure variable of the linear FLC, see Figure 7.4 (b), as well as the failure variable of the GFLC model, see Figure 7.4 (c), show no risk of failure even when a safety margin is applied for the FE simulation. For the linear FLC, a failure value of $\lambda = 0.975$, and for the GFLC model, a failure value of $\lambda = 0.937$ is determined. The failure variable of the 3D-GFLC model reaches a value of $\lambda = 1.444$ in the area where the split occurs, see Figure 7.4 (d). Therefore, the 3D-GFLC model is the only model to accurately predict failure.

Nevertheless, the current implementation also shows some false positive areas where a risk of splits is detected. Due to the very small strain increments needed to detect the change in the loading direction, the angle α is not stable. The angle α is calculated using the strains in x- and y-direction also called ε_{11} and ε_{22}. These strains are also used to calculate the major and minor strain. This means that the ε_{11} and ε_{22} strains vary in the amount of +/-0.001 leading to changes in the value of the angle α. Those jumps are currently handled as a change in the loading direction. Due to the many changes in the loading direction and the limited remaining formability, the failure value is rapidly increasing. To overcome this problem, a smoothing of the ε_{11} and ε_{22} strain values would be necessary.

Also, the 3D-GFLC model is only active for those elements with a major strain above 0.1. Below this level, the GFLC model is sufficient. This assumption seems valid as a change in the loading direction affects the formability only at higher strains. Another limitation is that only angles between 0° and 90° are currently considered. A change in the loading direction by 135° is handled like a change in the loading direction by 45°.

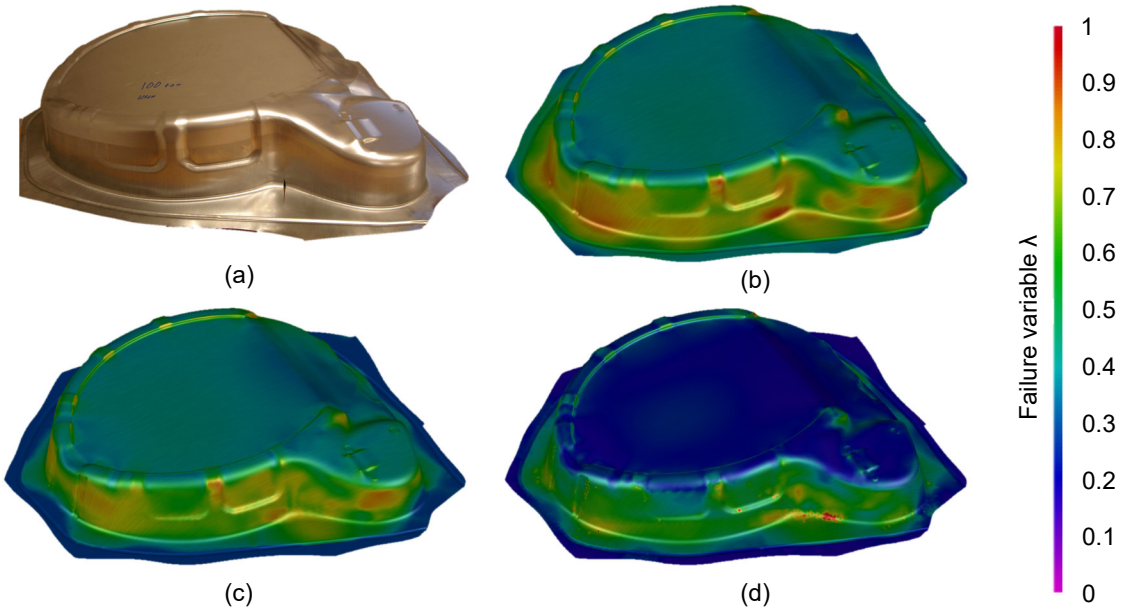

Figure 7.4: Industrial part to be simulated (a), results obtained by the linear FLC (b), the GFLC model (c) and the 3D-GFLC model (d).

8 Summary and Outlook

8.1 Summary

Modern FE simulations are able to predict the onset of localized necking in sheet metal forming for numerous components. Many improvements and extensions of the functionalities, such as more complex material models (BBC2005, YLD2000 or Vegter) or the implementation of complex friction models, have led to an even better prediction of failure. The occurring load path has a significant influence on the prediction accuracy. Different models have been developed for non-proportional load paths. However, all these models have the limitation of not being able to predict the failure of load paths with a change in load direction.

This work, therefore, dealt with the influence of the change in loading direction on the mechanical behaviour of three different materials. These three materials cover a large part of industrially used materials and, therefore, have an industrial relevance. The three materials are the HC340LA steel with its single-phase microstructure, the DP600 steel as a representative of the dual-phase steels with its microstructure consisting of ferrite and martensite, and the aluminium alloy AA6016-T4. Besides the experimental analysis of the influence by means of different experiments, from the macroscopic to the microscopic level, a methodology was developed to predict the failure after complex load paths with a change of the loading direction.

With the help of a modified Marciniak tool, it was possible to introduce specific pre-forming states into the materials. Its punch geometry makes it possible to extract further samples from the pre-formed blank. The first part of this thesis is specifically concerned with determining the influence of pre-forming with a change in loading direction on formability. For this purpose, a standardised Nakajima test was carried out with the pre-formed samples. The influence could be determined through three different pre-forming levels combined with five different post-loading directions.

The two steels show a clear dependency. This was particularly evident in the case of post-forming on the left side of the FLC (uniaxial and plane-strain). No necking over the thickness was observed for those specimens but the evolution of shear bands. In some cases, the evolution of multiple shear bands was visible, especially for the high pre-forming levels. Beside these shear bands, almost no further plastic deformation occurred. In the further progress of the experiment, the shear bands strengthened and finally led to the failure of the specimen. Notably,

the decrease in formability only occurs after a certain pre-forming level. Below this level, a change in the loading direction hardly affects the formability. In contrast to the two steels, the aluminium alloy is almost unaffected by a change in the direction of loading. Regardless of the pre-forming level or the change of the loading direction, this material showed almost identical formability.

To investigate the cause of this different behaviour in more detail, tensile tests were also investigated with pre-formed samples. The application of further sensors on Nakajima specimens is challenging due to the contact between the punch and the specimen. The tensile test, on the other hand, offers the advantage of good accessibility to the specimen and the possibility of applying additional sensors such as temperature sensors or strain gauges.

The tensile tests confirmed the behaviour already observed in the Nakajima tests. The steels show a significant dependence of the fracture elongation on the loading direction after a pre-forming. The aluminium alloy, in turn, is unaffected. It was striking that the reduced fracture elongation already occurred at pre-forming levels of approx. $\varepsilon_{pre} = 0.08$. In the Nakajima tests, a pre-forming level of approx. $\varepsilon_{pre} = 0.15$ was necessary to observe a reduction. Further investigations with different strain rates in the tensile test as well as Marciniak tests, could show that the strain rate has a considerable influence on the formability. Since significantly higher strain rates occur in the Nakajima test than in the tensile test, this leads to an increase in formability. The curvature of the Nakajima punch also has a positive effect on formability, but this effect is smaller than that of the strain rate.

The general obervation of the decrease in formability cannot be explained on a macroscopic level. Therefore, further investigations were carried out at the microscopic level. For this purpose, in-situ diffraction experiments were conducted at the German Electron Synchrotron. These allow a time-synchronous acquisition of the macroscopic and microscopic processes in the material during the tensile test.

These investigations showed that a change in the direction of loading has significant effects on formability and the onset of yielding. Thus, an orthogonal loading in the second deformation significantly reduces the yield stress, regardless of the material investigated. This could be shown with the help of the lattice strains as well as the dislocation density. For this purpose, the peak shift was used to determine the lattice strain and the peak broadening to determine the dislocation density. The Young's modulus $YS_{0.2\%}$ method is no longer sufficient to precisely determine the yield stress for such an orthogonal loading. The use of the temperature-based methodologies YS_{Tmin} and YS_0 developed by Vitzthum et al. (2022a) lead to much more reliable results.

After the onset of plastic deformation assessed by the temperature-based method YS_0, there is a decrease in dislocation density in the longitudinal direction in the case of orthogonal loading. The decrease in dislocation density was most pronounced for the HC340LA as well as the DP600 steel. The aluminium alloy AA6016-T4 showed only a slight decrease in dislocation density. In the further course of the tensile test, the dislocation density increases again for all materials. But, this decrease could not be observed in the transverse direction.

The analysis of the texture of the materials shows that the existing initial texture increases with increasing deformation. The steels keep their rolling texture with a strong α- and γ-fiber, while the aluminium alloy keeps its cubic texture. Only slight changes in the texture were observed after orthogonal loading in the second step. A greater influence of the texture on the material behaviour could not be shown.

The investigation of the microstructure by means of nanoindentation could only be carried out for two materials. These were the HC340LA and the AA6016-T4. This is due to the need for sufficiently large grains. Due to the two phases of the DP600 in combination with a small grain size, the indents could not be clearly assigned to a phase or the grain boundary. The materials were tested after different pre-forming levels from the initial state up to $\varepsilon_{pre} = 0.15$. The HC340LA showed a greater increase in the strength of the grain boundaries compared to the grain center. AA6016-T4 showed the opposite behaviour. Here, the grain centers show a higher hardening than the grain boundaries.

The examination of the fracture surfaces using SEM imaging of the tensile and Nakajima specimens showed clear differences between the specimens with and without a change in the direction of loading. The steels examined showed ductile failure with numerous small dimples in the IF0-PF0 specimens. The IF0-PF90 specimens, on the other hand, showed significantly larger pores with parabolically shaped dimples between them. This appearance is caused by shear failure of the sample. The aluminium alloy showed brittle fracture behaviour for both specimens, IF0-PF0 and IF0-PF90, without the formation of dimples. After the pre-forming, no damage like voids or martensite cracks occurred in the AA6016-T4 and the DP600 materials, as found in SEM images. Only the HC340LA showed a small number of voids in the size below 1 µm.

The investigations carried out have shown numerous effects of changing the direction of loading after pre-forming. The following points list the most important causes for the observed material behaviour in their chronological order of occurrence during the experiments:

- **Grain-to-grain yielding**
  Specimens with a change in the loading direction showed that the individual lattice planes start to plasitify at different stress levels. The higher the pre-forming level, the more the individual lattice planes differ. This behaviour is caused by grain-to-grain yielding. The activation of new slip systems influences the onset of yielding. Due to the different stress levels at which yielding starts, the elastic-plastic transition is rather smooth. For specimens with no change in the loading direction, a sharp elastic-plastic transition is observed, which corresponds well with the findings of the lattice strains. The onset of yielding for both loading directions, IF0-PF0 and IF0-PF90, was captured accurately by temperature-based methods.

- **Dislocation density**
  The decrease in the dislocation density is due to the presence of dense dislocation walls developed during the pre-forming of the specimens. These dislocation walls are weakened during orthogonal loading of the specimen. This weakening is caused by the annihilation of dislocations. Mobile dislocations with opposing sign meet and cancel themselves out. The annihilation process is dependent on the possibility of dislocations to move. This seems to be easier within the investigated *bcc*-materials. The annihilation process of the dislocations is time-dependent. If there is not sufficient time, no equilibrium can be reached, and fewer dislocations are annihilated, leading to an increase in formability and a positive hardening rate. Nevertheless, the formability is still significantly reduced compared to the IF0-PF0 specimens. Suppose the experiments are conducted at lower strain rates. In that case, the sufficiently high annihilation of the dislocations leads to a decrease in the strain hardening rate, even to negative values and, therefore, strain softening. One key factor for this process to lead to early failure is sufficiently dense dislocation walls. Such walls need a certain level of pre-forming, as observed in the tensile and Nakajima tests.

- **Shear bands and fracture**
  The strain softening leads to microscopic plastic instability. Meaning that the material starts to fail on a microscopic scale. This microscopic instability leads to macroscopic shear bands, which start to evolve. The loss of formability for sufficiently high pre-formed materials in the Nakajima and Marciniak tests all show such shear bands. Especially in the Marciniak experiments with its flat punch, many shear bands are visible, see Figure 6.28 (b). The shear failure is also observed in SEM images of the fracture surface. The fracture surface of specimens with shear bands shows an increased void size in combination with parabolic dimples indicating shear failure processes.

Not all materials are sensitive to a change in the loading direction. For example, the AA6016-T4 examined in this study. This might be attributed to the ability to form dislocations. Materials with only a small amount of inclusions, and therefore a larger distance between possible pinning points, need a lower critical shear stress to create dislocations according to the Frank-Read mechanism (Frank and Read, 1950), where the distance between the pinning sites of the dislocation plays a crucial role. The amount of GNDs is also dependent on the microstructure. The density of GNDs is directly linked to the grain size D and burgers vector b and the plastic deformation ϵ by Ashby's model (Ashby, 1970):

$$\rho_{GND} = \frac{\epsilon}{4bD} \tag{8.1}$$

Meaning that, for example, the investigated aluminium alloy AA6016-T4 with many non-metallic inclusions and a large grain size requires a higher critical shear stress for the dislocation multiplication using the Frank-Read mechanism to happen. Also, the density of the GNDs is reduced due to the larger grain size compared to the two investigated steels. This can also explain why the aluminium alloy has a lower increase in the nano hardness at the grain boundaries compared to the grain centers, as GNDs are dominant at the grain boundaries. In the study of Volk et al. (2020a), the IF-steel HC260Y, with its large grain size and no inclusions, showed the most significant loss of formability. While the DP600, with its small grain size and two phases investigated in this study, showed a lower loss of formability than the HC340LA or HC260Y steel.

Even though the mechanisms behind the loss of formability result from processes at different length scales, it is possible to predict failure after such complex load paths with a change in the loading direction. Using an extension of the phenomenological GFLC model, it was possible to implement the 3D-GFLC model into the commercial FE software AutoForm using the R&D plug-in. The accuracy and the functionality of the proposed model were shown by predicting the failure of an industrial part which showed a change in the loading direction after a plane-strain pre-forming. This is in contrast to the other failure criteria investigated, the linear FLC and the GFLC model.

8.2 Outlook

Despite the numerous studies that have been carried out within the framework of this work, there are still further open questions. Some mechanisms or types of dislocations can not be examined by an experimental study but can be simulated. These open questions will be discussed in the further course:

- **Other pre-forming states**
  The investigation of different pre-forming states for the database of the 3D-GFLC model showed that the loss of formability occurs more on the left side of the FLC for materials which are sensitive to a change in the loading direction. For this pre-forming state, only three different changes in the loading direction are investigated. The influence of a high plane-strain pre-forming on the three materials can be seen in Figure 8.1. For the steels, a plane-strain post-forming leads to almost instant necking of the specimens.

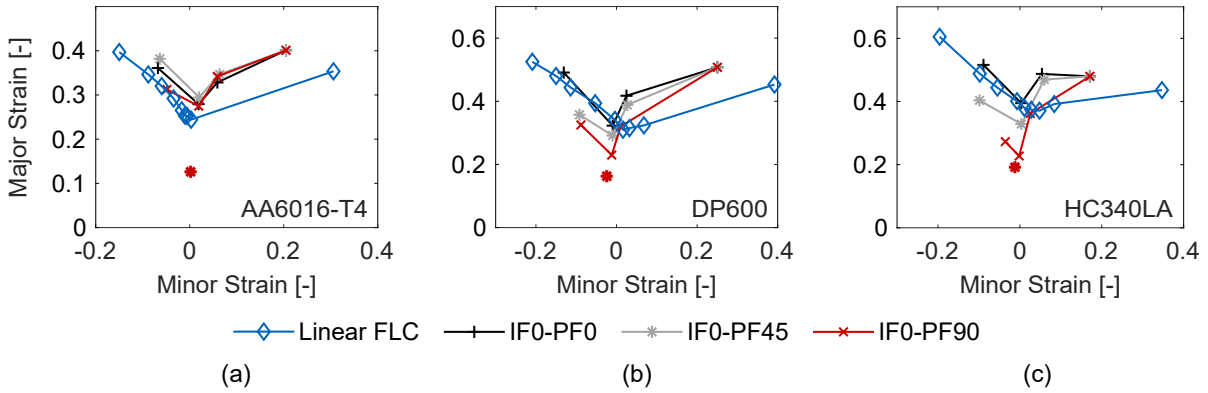

Figure 8.1: Influence of a plane-strain pre-forming on AA6016-T4 (a), the DP600 (b) and the HC340LA (c).

  Further investigations of other pre-forming states (e.g. plane-strain, biaxial) on the onset of yielding or the dislocation density have not yet been carried out. These would provide further insight into the cause of this material behaviour.

- **Investigations using TEM**
  Since the cause of the material behaviour is based on dislocation mechanisms, further investigation of these mechanisms is desirable. TEM investigations are a good way to do this. TEM can be used to show dislocation structures and to determine the actual dislocation density. In contrast to EBSD, not only GNDs can be analysed with this method. Newer experimental set-ups are also able to carry out in-situ TEM investigations.

These would be particularly interesting with regard to the decrease in dislocation density after the onset of yielding.

- **Dislocation based simulations**
  The distinction between mobile and immobile dislocations is also not possible by means of synchrotron diffraction, EBSD or TEM. However, since these two types of dislocations greatly influence the material behaviour, further investigation is of interest here. Simulation methods which can handle dislocation behaviour, like the discrete dislocation dynamics simulation (DDD) or crystal-plasticity-based simulations, are able to show the different dislocation types by means of models. These simulations could lead to further clues as to the causes.

- **Investigation of further material classes and grades**
  Three classes of materials were investigated in this work. These showed partly clearly different material behaviour. Since the cause for this is based on the microstructure, further investigations with different material classes are necessary. The investigation of IF-steels such as HC260Y would be particularly useful to confirm the theories that have been put forward, as it already has been proven that this material is sensitive to a change in the loading direction. Likewise, a different heat treatment condition would be interesting for the aluminium alloy AA6016-T4. Due to the fact that the heat treatment leads to the precipitation or distribution of inclusions. A heat treatment that leads to few inclusions would be desirable, or even pure aluminium, like AA1050-O.

- **Optimisation of the current 3D-GFLC implementation in AutoForm**
  The current implementation of the 3D-GFLC model still needs some improvement. There are false positives in some places. This is due to the fact that a change in direction is difficult to detect because of the implicit calculation methodology with many individual increments. In the case of the component under investigation, there is an abrupt change in the loading direction. This is an advantage in detecting such directional changes. In the case of other components, however, there may be a gradual change in the loading direction. Such cases still need to be covered.

A change in the loading direction after pre-forming can massively influence the material behaviour. This work was a first step towards a deeper understanding of the effect and the causes.

A List of Figures

B List of Tables

C Bibliography

ANDRADE, F. X. C., M. FEUCHT, A. HAUFE, and F. NEUKAMM (2016). “An incremental stress state dependent damage model for ductile failure prediction”. In: *International Journal of Fracture* 200, pp. 127–150.

ARRIEUX, R., M. BOIVIN, and F. LE MAÎTRE (1987). “Determination of the Forming Limit Stress Curve for Anisotropic Sheets”. In: *CIRP Annals* 36, pp. 195–198.

ARSENLIS, A. and D.M PARKS (1999). “Crystallographic aspects of geometrically-necessary and statistically-stored dislocation density”. In: *Acta Materialia* 47, pp. 1597–1611.

ASHBY, M. F. (1970). “The deformation of plastically non-homogeneous materials”. In: *The Philosophical Magazine: A Journal of Theoretical Experimental and Applied Physics* 21, pp. 399–424.

AŞIK, E. E., E. S. PERDAHCIOĞLU, and A. H. VAN DEN BOOGAARD (2019). “Microscopic investigation of damage mechanisms and anisotropic evolution of damage in DP600”. In: *Materials Science and Engineering: A* 739, pp. 348–356.

AVRAMOVIC-CINGARA, G., C. A. R. SALEH, M. K. JAIN, and D. S. WILKINSON (2009). “Void Nucleation and Growth in Dual-Phase Steel 600 during Uniaxial Tensile Testing”. In: *Metallurgical and Materials Transactions A* 40, pp. 3117–3127.

AYDOGAN, E., S. PAL, O. ANDEROGLU, S. A. MALOY, S. C. VOGEL, G. R. ODETTE, J. J. LEWANDOWSKI, D. T. HOELZER, I. E. ANDERSON, and J. R. RIEKEN (2016). “Effect of tube processing methods on the texture and grain boundary characteristics of 14YWT nanostructured ferritic alloys”. In: *Materials Science and Engineering: A* 661, pp. 222–232.

BAIKER, M. (2016). “Mikrostruktursimulationen zur Ermittlung von Materialeigenschaften für Blechwerkstoffe und Anwendung in der Umformsimulation”. Dissertation. Fraunhofer-Institut für Werkstoffmechanik IWM.

BANABIC, D., Bunge H.-J., Pohlandt K., and Tekkaya A. E. (2000). *Formability of metallic materials: Plastic anisotropy, formability testing, forming limits*. Berlin and Heidelberg: Springer Berlin Heidelberg.

BANABIC, D. and H. HUETINK (2006). *Determination of the yield locus by means of temperature measurement*.

BANABIC, D., L. LAZARESCU, L. PARAIANU, I. CIOBANU, I. NICODIM, and D. S. COMSA (2013). “Development of a new procedure for the experimental determination of the Forming Limit Curves”. In: *CIRP Annals* 62, pp. 255–258.

BAO, Y. and T. WIERZBICKI (2004). “On fracture locus in the equivalent strain and stress triaxiality space”. In: *International Journal of Mechanical Sciences*, pp. 81–98.

BARLAT, F., J. M. FERREIRA DUARTE, J. J. GRACIO, A. B. LOPES, and E. F. RAUCH (2003). “Plastic flow for non-monotonic loading conditions of an aluminum alloy sheet sample”. In: *International Journal of Plasticity* 19, pp. 1215–1244.

BARLAT, F., J. J. GRÁCIO, M.-G. LEE, E. F. RAUCH, and G. VINCZE (2011). "An alternative to kinematic hardening in classical plasticity". In: *International Journal of Plasticity* 27, pp. 1309–1327.

BARLAT, F., G. VINCZE, J. J. GRÁCIO, M.-G. LEE, E. F. RAUCH, and C. N. TOMÉ (2014). "Enhancements of homogenous anisotropic hardening model and application to mild and dual-phase steels". In: *International Journal of Plasticity* 58, pp. 201–218.

BARLAT, F., S.-Y. YOON, S.-Y. LEE, M.-S. WI, and J.-H. KIM (2020). "Distortional plasticity framework with application to advanced high strength steel". In: *International Journal of Solids and Structures* 202, pp. 947–962.

BEAUSIR, B. and J.-J. FUNDENBERGER (2016). *Analysis Tools for Electron and X-ray diffraction, ATEX - software*. Université de Lorraine - Metz. URL: www.atex-software.eu.

BIJU, V., N. SUGATHAN, V. VRINDA, and S. L. SALINI (2008). "Estimation of lattice strain in nanocrystalline silver from X-ray diffraction line broadening". In: *Journal of Materials Science* 43, pp. 1175–1179.

BINDU, P. and S. THOMAS (2014). "Estimation of lattice strain in ZnO nanoparticles: X-ray peak profile analysis". In: *Journal of Theoretical and Applied Physics* 8, pp. 123–134.

BIRKERT, A., S. HAAGE, and M. STRAUB (2013). *Umformtechnische Herstellung komplexer Karosserieteile: Auslegung von Ziehanlagen*. Berlin, Heidelberg: Springer Berlin Heidelberg.

BRAGG, W. H. (1913). "The Reflection of X-Rays by Crystals". In: *Nature* 91, p. 477.

BRÜNIG, M., S. GERKE, and M. ZISTL (2019). "Experiments and numerical simulations with the H-specimen on damage and fracture of ductile metals under non-proportional loading paths". In: *Engineering Fracture Mechanics* 217, p. 106531.

CASALS, O. and J. ALCALÁ (2005). "The duality in mechanical property extractions from Vickers and Berkovich instrumented indentation experiments". In: *Acta Materialia* 53, pp. 3545–3561.

CHAE, D., J.P BANDSTRA, and D.A KOSS (2000). "The effect of pre-strain and strain-path changes on ductile fracture: experiment and computational modeling". In: *Materials Science and Engineering: A* 285, pp. 165–171.

CHEN, J. H. and R. CAO (2015). "Effects of Material Microstructure on Cleavage Fracture". In: *Micromechanism of Cleavage Fracture of Metals*. Elsevier, pp. 241–270.

CHOI, B.-W., D.-H. SEO, J.-Y. YOO, and J.-I. JANG (2009). "Predicting macroscopic plastic flow of high-performance, dual-phase steel through spherical nanoindentation on each microphase". In: *Journal of Materials Research* 24, pp. 816–822.

CHRISTIEN, F., M. T. F. TELLING, K. S. KNIGHT, and R. LE GALL (2015). "A method for the monitoring of metal recrystallization based on the in-situ measurement of the elastic energy release using neutron diffraction". In: *Review of Scientific Instruments* 86, p. 053901.

CLAUSMEYER, T., G. GERSTEIN, S. BARGMANN, B. SVENDSEN, A. H. VAN DEN BOOGAARD, and B. ZILLMANN (2013). "Experimental characterization of microstructure development during loading path changes in bcc sheet steels". In: *Journal of Materials Science* 48, pp. 674–689.

COLLINS, D. M., T. ERINOSHO, F. P. E. DUNNE, R. I. TODD, T. CONNOLLEY, M. MOSTAFAVI, H. KUPFER, and A. J. WILKINSON (2017). “A synchrotron X-ray diffraction study of non-proportional strain-path effects”. In: *Acta Materialia* 124, pp. 290–304.

CONNOLLY, M., M. MAY, P. BRADLEY, D. LAURIA, A. SLIFKA, R. AMARO, C. LOONEY, and J.-S. PARK (2019). “In situ high energy X-ray diffraction measurement of strain and dislocation density ahead of crack tips grown in hydrogen”. In: *Acta Materialia* 180, pp. 272–286.

CONSIDÈRE, M. (1885). “L’emploi du fer et de l’acier dans les constructions”. In: *Annales Des Ponts et Chausses* 1885, pp. 574–775.

CREUZIGER, A., L. HU, T. GNÄUPEL-HEROLD, and A. D. ROLLETT (2014). “Crystallographic texture evolution in 1008 steel sheet during multi-axial tensile strain paths”. In: *Integrating Materials and Manufacturing Innovation* 3, pp. 1–19.

CUNIBERTI, A., A. TOLLEY, V. RIGLOS M. Castro, and R. GIOVACHINI (2010). “Influence of natural aging on the precipitation hardening of an AlMgSi alloy”. In: *Materials Science and Engineering: A* 527, pp. 5307–5311.

DA BARATA ROCHA, A., F. BARLAT, and J. M. JALINIER (1985). “Prediction of the forming limit diagrams of anisotropic sheets in linear and non-linear loading”. In: *Materials Science and Engineering* 68, pp. 151–164.

DEBYE, P. and P. SCHERRER (1916). “Interferenzen an regellos orientierten Teilchen im Röntgenlicht. I.” In: *Nachrichten von der Gesellschaft der Wissenschaften zu Göttingen, Mathematisch-Physikalische Klasse* 1916, pp. 1–15.

DELANNAY, L., S. R. KALIDINDI, and P. VAN HOUTTE (2002). “Quantitative prediction of textures in aluminium cold rolled to moderate strains”. In: *Materials Science and Engineering: A* 336, pp. 233–244.

DELHEZ, R., T. H. de KEIJSER, and E. J. MITTEMEIJER (1982). “Determination of crystallite size and lattice distortions through X-ray diffraction line profile analysis”. In: *Fresenius’ Zeitschrift für analytische Chemie* 312, pp. 1–16.

DICK, R. E., J. W. YOON, and T. B. STOUGHTON (2016). “Path-independent forming limit models for multi-stage forming processes”. In: *International Journal of Material Forming* 9, pp. 327–337.

DILMEC, M., H. S. HALKACI, F. OZTURK, H. LIVATYALI, and O. YIGIT (2013). “Effects of sheet thickness and anisotropy on forming limit curves of AA2024-T4”. In: *The International Journal of Advanced Manufacturing Technology* 67, pp. 2689–2700.

DIN 50125 (2022). *Testing of metallic materials - Tensile test pieces*. Berlin.

DIN EN 10268 (2013). *Cold rolled steel flat products with high yield strength for cold forming - Technical delivery conditions*. Berlin.

DIN EN 10346 (2015). *Continuously hot-dip coated steel flat products for cold forming - Technical delivery conditions;* Berlin.

DIN EN 573-3 (2022). *Aluminium and aluminium alloys - Chemical composition and form of wrought products - Part 3: Chemical composition and form of products*. Berlin.

DIN EN ISO 12004-2 (2021). *Metallic materials - Determination of forming-limit curves for sheet and strip - Part 2: Determination of forming-limit curves in the laboratory*. Berlin.

DIN EN ISO 6892-1 (2020). *Metallic materials - Tensile testing - Part 1: Method of test at room temperature*. Berlin.

DOEGE, E. and B.-A. BEHRENS (2018). *Handbuch Umformtechnik: Grundlagen, Technologien, Maschinen*. Berlin, Heidelberg: Springer Berlin Heidelberg.

DROTLEFF, K. (2021). "Verbesserte Prognose lokaler Einschnürungen in mehrstufigen Blechumformprozessen". Dissertation. Universität Stuttgart.

DROTLEFF, K. and M. LIEWALD (2018). "Application of an advanced necking criterion for nonlinear strain paths to a complex sheet metal forming component". In: *IOP Conference Series: Materials Science and Engineering* 418.

EDER, M. (2023). "Validierung von Materialmodellen: Der MUC-Test als Methodik zur Qualifizierung von Materialmodellen für Blechwerkstoffe". Dissertation. Technische Universität München.

EIGENMANN, B. and E. MACHERAUCH (1996). "Röntgenographische Untersuchung von Spannungszuständen in Werkstoffen. Teil III." In: *Materialwissenschaft und Werkstofftechnik* 27, pp. 426–437.

ENGLER, O. (2022). "Effect of precipitation state on plastic anisotropy in sheets of the age-hardenable aluminium alloys AA 6016 and AA 7021". In: *Materials Science and Engineering: A*.

FAN, H., Q. WANG, J. A. EL-AWADY, D. RAABE, and M. ZAISER (2021). "Strain rate dependency of dislocation plasticity". In: *Nature Communications* 12.

FRANK, F. C. and W. T. READ (1950). "Multiplication Processes for Slow Moving Dislocations". In: *Physical Review* 79, pp. 722–723.

FU, L., G. WU, C. ZHOU, Z. XIU, W. YANG, and J. QIAO (2021). "Effect of Microstructure on the Dimensional Stability of Extruded Pure Aluminum". In: *Materials* 14.

GERKE, S., M. ZISTL, A. BHARDWAJ, and M. BRÜNIG (2019). "Experiments with the X0-specimen on the effect of non-proportional loading paths on damage and fracture mechanisms in aluminum alloys". In: *International Journal of Solids and Structures* 163, pp. 157–169.

GOODWIN, G. M. (1968). "Application of Strain Analysis to Sheet Metal Forming Problems in the Press Shop". In: *SAE Technical Paper Series* 77, pp. 380–387.

GRAF, A. and W. HOSFORD (1993). "Calculations of Forming Limit Diagrams for Changing Strain Paths". In: *Metallurgical and Materials Transactions A* 24, pp. 2497–2501.

– (1994). "The influence of strain-path changes on forming limit diagrams of A1 6111 T4". In: *International Journal of Mechanical Sciences* 36, pp. 897–910.

HA, J., M.-G. LEE, and F. BARLAT (2013). "Strain hardening response and modeling of EDDQ and DP780 steel sheet under non-linear strain path". In: *Mechanics of Materials* 64, pp. 11–26.

HAMMERSLEY, A. P. (2016). "FIT2D : a multi-purpose data reduction, analysis and visualization program". In: *Journal of Applied Crystallography* 49, pp. 646–652.

HARJO, S., S. KUBOTA, W. GONG, T. KAWASAKI, and S. GAO (2020). “Neutron diffraction monitoring of ductile cast iron under cyclic tension–compression”. In: *Acta Materialia* 196, pp. 584–594.

HÉRAULT, D., S. THUILLIER, S.-Y. LEE, P.-Y. MANACH, and F. BARLAT (2021). “Calibration of a strain path change model for a dual phase steel”. In: *International Journal of Mechanical Sciences* 194.

HIPPKE, H., B. BERISHA, and P. HORA (2018). “A failure model for non-proportional loading under plane stress condition based on GFLC in comparison to eMMFC and PEPS”. In: *IOP Conference Series: Materials Science and Engineering* 418.

HOFFMANN, H., R. NEUGEBAUER, and G. SPUR (2012). *Handbuch Umformen*. München: Hanser.

HÖLSCHER, Martin, Dierk RAABE, and Kurt LÜCKE (1991). “Rolling and recrystallization textures of bcc steels”. In: *Steel Research* 62, pp. 567–575.

HORA, P. and L. TONG (2008). “Theoretical prediction of the influence of curvature and thickness on the FLC by the enhanced Modified Maximum Force Criterion”. In: *Proceedings of the Numisheet 2008*.

HORA, P., L. TONG, and B. BERISHA (2013). “Modified maximum force criterion, a model for the theoretical prediction of forming limit curves”. In: *International Journal of Material Forming* 6, pp. 267–279.

HORA, P., L. TONG, and J. REISSNER (1996). “A prediction method for ductile sheet metal failure in FE-simulation”. In: *Proceedings of the NUMISHEET96* 7, pp. 252–256.

HOTZ, W., M. MERKLEIN, A. KUPPERT, H. FRIEBE, and M. KLEIN (2013). “Time Dependent FLC Determination Comparison of Different Algorithms to Detect the Onset of Unstable Necking before Fracture”. In: *Key Engineering Materials* 549, pp. 397–404.

HSUEH, Chun-Hway, Siegfried SCHMAUDER, Chuin-Shan CHEN, Krishan K. CHAWLA, Nikhilesh CHAWLA, Weiqiu CHEN, and Yutaka KAGAWA, eds. (2019). *Handbook of mechanics of materials*. Singapore: Springer.

HUGHES, D.A (2001). “Microstructure evolution, slip patterns and flow stress”. In: *Materials Science and Engineering: A* 319-321, pp. 46–54.

INAL, K., K. W. NEALE, and A. ABOUTAJEDDINE (2005). “Forming limit comparisons for FCC and BCC sheets”. In: *International Journal of Plasticity* 21, pp. 1255–1266.

JAMAATI, R. and M. R. TOROGHINEJAD (2014). “Effect of stacking fault energy on deformation texture development of nanostructured materials produced by the ARB process”. In: *Materials Science and Engineering: A* 598, pp. 263–276.

JOCHAM, D. (2018). “Bestimmung der lokalen Einschnürung nach linearer und nichtlinearer Umformhistorie sowie Ermittlung dehnungs- und geschwindigkeitsabhängiger Materialkennwerte”. Dissertation. Technische Universität München.

JOCHAM, D., C. GABER, O. BÖTTCHER, P. WIEDEMANN, and W. VOLK (2017). "Experimental prediction of sheet metal formability of AW-5754 for non-linear strain paths by using a cruciform specimen and a blank holder with adjustable draw beads on a sheet metal testing machine". In: *International Journal of Material Forming* 10, pp. 597–605.

JUAN, R., N. X. BINH, W. LIU, and J. LIAN (2023). "Optimizing crystal plasticity model parameters via machine learning-based optimization algorithms". In: *Materials Research Proceedings* 28, pp. 1417–1426.

JUAN, R., W. LIU, X. INZA, X. URETA, J. MENDIGUREN, and J. LIAN (2022). "Crystal Plasticity Modeling of Al Alloy under Linear and Non-Linear Loading". In: *Key Engineering Materials* 926, pp. 2099–2108.

KEELER, S. P. (1961). "Plastic instability and fracture in sheets stretched over rigid punches". Dissertation. Massachusetts Institute of Technology.

– (1966). "Determination of Forming Limits in Automotive Stampings". In: *SAE Technical Paper Series* 74, pp. 1–9.

KESTENS, L. A. I. and H. PIRGAZI (2016). "Texture formation in metal alloys with cubic crystal structures". In: *Materials Science and Technology* 32, pp. 1303–1315.

KIM, H., F. BARLAT, Y LEE, S. B. ZAMAN, C. S. LEE, and Y. JEONG (2018). "A crystal plasticity model for describing the anisotropic hardening behavior of steel sheets during strain-path changes". In: *International Journal of Plasticity* 111, pp. 85–106.

KUWABARA, T., T. MORI, M. ASANO, T. HAKOYAMA, and F. BARLAT (2017). "Material modeling of 6016-O and 6016-T4 aluminum alloy sheets and application to hole expansion forming simulation". In: *International Journal of Plasticity* 93, pp. 164–186.

LAROUR, P., A. BÄUMER, K. DAHMEN, and W. BLECK (2013). "Influence of Strain Rate, Temperature, Plastic Strain, and Microstructure on the Strain Rate Sensitivity of Automotive Sheet Steels". In: *steel research international* 84, pp. 426–442.

LARSSON, R., O. BJÖRKLUND, L. NILSSON, and K. SIMONSSON (2011). "A study of high strength steels undergoing non-linear strain paths—Experiments and modelling". In: *Journal of Materials Processing Technology* 211, pp. 122–132.

LASSANCE, D., D. FABRÉGUE, F. DELANNAY, and T. PARDOEN (2007). "Micromechanics of room and high temperature fracture in 6xxx Al alloys". In: *Progress in Materials Science* 52, pp. 62–129.

LEOTOING, L., D. GUINES, I. ZIDANE, and E. RAGNEAU (2013). "Cruciform shape benefits for experimental and numerical evaluation of sheet metal formability". In: *Journal of Materials Processing Technology* 213, pp. 856–863.

LIAN, J., W. LIU, X. GASTAÑARES, R. JUAN, and J. MENDIGUREN (2022). "Plasticity evolution of an aluminum-magnesium alloy under abrupt strain path changes". In: *International Journal of Material Forming* 15, p. 205.

MACKENSEN, A. (2014). "Presswerkorientierte Analyse der Umform- und Scherschneideigenschaften von Mehrphasenstählen". Dissertation. Technische Universität München.

MADHAVI, J. (2019). “Comparison of average crystallite size by X-ray peak broadening and Williamson–Hall and size–strain plots for VO2+ doped ZnS/CdS composite nanopowder”. In: *SN Applied Sciences* 1.

MAIRE, E., O. BOUAZIZ, M. DI MICHIEL, and C. VERDU (2008). “Initiation and growth of damage in a dual-phase steel observed by X-ray microtomography”. In: *Acta Materialia* 56, pp. 4954–4964.

MANOPULO, N., P. HORA, P. PETERS, M. GORJI, and F. BARLAT (2015). “An extended Modified Maximum Force Criterion for the prediction of localized necking under non-proportional loading”. In: *International Journal of Plasticity* 75, pp. 189–203.

MARCINIAK, Z., J. L. DUNCAN, and S. J. HU (2002). *Mechanics of sheet metal forming*. Oxford: Butterworth-Heinemann.

MARCINIAK, Z. and K. KUCZYŃSKI (1967). “Limit strains in the processes of stretch-forming sheet metal”. In: *International Journal of Mechanical Sciences* 9, pp. 609–620.

MERKLEIN, M., A. KUPPERT, and M. GEIGER (2010a). “Time dependent determination of forming limit diagrams”. In: *CIRP Annals* 59, pp. 295–298.

MERKLEIN, M., A. KUPPERT, S. MÜTZE, and A. GEFFERT (2010b). “New Time Dependent Method for Determination of Forming Limit Curves Applied to SZBS800”. In: *Proceedings of the IDDRG conference 2010*. IDDRG 2010.

MILLER, W. H. (1839). *A Treatise on Crystallography*. Cambridge, UK: For J. & J. J. Deighton.

MITTEMEIJER, E. J. and U. WELZEL (2008). “The “state of the art” of the diffraction analysis of crystallite size and lattice strain”. In: *Zeitschrift für Kristallographie* 223, pp. 552–560.

MIYAHARA, K., S. MATSUOKA, and T. HAYASHI (2001). “Nanoindentation as a strength probe—a study on the hardness dependence of indent size for fine-grained and coarse-grained ferritic steel”. In: *Metallurgical and Materials Transactions A* 32, pp. 761–768.

MIYAJIMA, Y., T. UEDA, H. ADACHI, T. FUJII, S. ONAKA, and M. KATO (2014). “Dislocation Density of FCC Metals Processed by ARB”. In: *IOP Conference Series: Materials Science and Engineering*.

MORAWIEC, A. (2004). *Orientations and Rotations: Computations in Crystallographic Textures*. Berlin, Heidelberg: Springer.

MÜLLER, W. (1996). “Beitrag zur Charakterisierung von Blechwerkstoffen unter mehrachsiger Beanspruchung”. Dissertation. Technische Universität München.

MURÁNSKY, O., L. BALOGH, M. TRAN, C. J. HAMELIN, J.-S. PARK, and M. R. DAYMOND (2019). “On the measurement of dislocations and dislocation substructures using EBSD and HRSD techniques”. In: *Acta Materialia* 175, pp. 297–313.

MÜSCHENBORN, W. and H.-M. SONNE (1975). “Einfluß des Formänderungsweges auf die Grenzformänderungen des Feinblechs”. In: *Archiv für das Eisenhüttenwesen* 46, pp. 597–602. ISSN: 00038962.

NAKAJIMA, K., T. KIKUMA, and K. HASUKA (1968). “Study on the formability of steel sheets”. In: *Yawata Technical Report* 264, pp. 8517–8530.

NEUKAMM, F., M. FEUCHT, and A. HAUFE (2009). "Considering damage history in crashworthiness simulations". In: *LS-Dyna Anwenderforum*.

NORZ, R. and W. VOLK (2019). "Investigation of non-proportional load paths by using a cruciform specimen in a conventional Nakajima test". In: *IOP Conference Series: Materials Science and Engineering* 651, p. 012020.

OFENHEIMER, A., B. BUCHMAYR, R. KOLLECK, and M. MERKLEIN (2005). "Forming Limits in Sheet Metal Forming for Non-Proportional Loading Conditions — Experimental and Theoretical Approach". In: *AIP Conference Proceedings*. AIP, pp. 460–465.

OHMURA, T., K. TSUZAKI, and F. YIN (2005). "Nanoindentation-Induced Deformation Behavior in the Vicinity of Single Grain Boundary of Interstitial-Free Steel". In: *Materials Transactions* 46, pp. 2026–2029.

OSTERMANN, F. (2014). *Anwendungstechnologie Aluminium*. Berlin, Heidelberg: Springer Berlin Heidelberg.

PAPASIDERO, J., V. DOQUET, and D. MOHR (2015). "Ductile fracture of aluminum 2024-T351 under proportional and non-proportional multi-axial loading: Bao–Wierzbicki results revisited". In: *International Journal of Solids and Structures* 69-70, pp. 459–474.

PECHARSKY, V. K. and P. Y. ZAVALIJ (2005). *Fundamentals of powder diffraction and structural characterization of materials*. Boston, MA: Springer US.

PINEAU, A., A. A. BENZERGA, and T. PARDOEN (2016). "Failure of metals I: Brittle and ductile fracture". In: *Acta Materialia* 107, pp. 424–483.

PISCHINGER, S. and U. SEIFFERT (2016). *Handbuch Kraftfahrzeugtechnik*. Wiesbaden: Springer Vieweg.

POZNAK, A., D. FREIBERG, and P. SANDERS (2018). "Automotive Wrought Aluminium Alloys". In: *Fundamentals of Aluminium Metallurgy*. Elsevier, pp. 333–386.

QIN, J., B. HOLMEDAL, and O. S. HOPPERSTAD (2018). "A combined isotropic, kinematic and distortional hardening model for aluminum and steels under complex strain-path changes". In: *International Journal of Plasticity* 101, pp. 156–169.

REIMER, L. and H. KOHL (2008). *Transmission electron microscopy: Physics of image formation*. New York, NY: Springer.

REZVANIAN, O., M.A ZIKRY, and A.M RAJENDRAN (2007). "Statistically stored, geometrically necessary and grain boundary dislocation densities: microstructural representation and modelling". In: *Proceedings of the Royal Society A: Mathematical, Physical and Engineering Sciences* 463, pp. 2833–2853.

RÖSLER, J. (2012). *Mechanisches Verhalten der Werkstoffe*. Wiesbaden: Springer Vieweg.

SABU, T., T. RAJU, Z. AJESH, and M. RAGHVENDRA (2017). *Microscopy Methods in Nanomaterials Characterization*. Elsevier.

SALLAT, G. (1988). "Theoretische und experimentelle Untersuchungen zum Fliessverhalten von Blechen im zweiachsigen Hauptspannungszustand". Dissertation. Technische Universität Karl-Marx-Stadt.

SCHUREN, J. and M. MILLER (2011). “Quantifying the uncertainty of synchrotron-based lattice strain measurements”. In: *The Journal of Strain Analysis for Engineering Design* 46, pp. 663–681.

SEOK, M.-Y., Y.-J. KIM, I.-C. CHOI, Y. ZHAO, and J.-I. JANG (2014). “Predicting flow curves of two-phase steels from spherical nanoindentation data of constituent phases: Isostrain method vs. non-isostrain method”. In: *International Journal of Plasticity* 59, pp. 108–118.

SIGVANT, M., K. MATTIASSON, and M. LARSSON (2008). “The definition of incipient necking and its impact on experimentally or theoretically determined forming limit curves”. In: *IDDRG 2008 Conference Proceedings* 1, pp. 1–12.

SONG, X., L. LEOTOING, D. GUINES, and E. RAGNEAU (2017). “Identification of forming limits at fracture of DP600 sheet metal under linear and unloaded non-linear strain paths”. In: *Procedia Engineering* 207, pp. 562–567.

SPIESS, L., G. TEICHERT, R. SCHWARZER, H. BEHNKEN, and C. GENZEL (2019). *Moderne Röntgenbeugung: Röntgendiffraktometrie für Materialwissenschaftler, Physiker und Chemiker*. Wiesbaden: Springer Spektrum.

STANJEK, H. and W. HÄUSLER (2004). “Basics of X-ray Diffraction”. In: *Hyperfine Interactions* 154, pp. 107–119.

STARON, P. (2009). *AFit 3.6 by P.Staron*.

STOUGHTON, T. B. (2000). “A general forming limit criterion for sheet metal forming”. In: *International Journal of Mechanical Sciences* 42, pp. 1–27.

STOUGHTON, T. B. and J. W. YOON (2012). “Path independent forming limits in strain and stress spaces”. In: *International Journal of Solids and Structures* 49, pp. 3616–3625.

STRUNZ, P., P. LUKÁS, and D. NEOV (2001). “Data evaluation procedure for high-resolution neutron diffraction methods”. In: *Journal of Neutron Research* 9.2, pp. 99–106.

SUH, J. S. (2015). “Improvement in Cold Formability of AZ31 Magnesium Alloy Sheets Processed by Equal Channel Angular Pressing (ECAP)”. Dissertation. Technische Universität München.

SUN, X., K. S. CHOI, W. N. LIU, and M. A. KHALEEL (2009). “Predicting failure modes and ductility of dual phase steels using plastic strain localization”. In: *International Journal of Plasticity* 25, pp. 1888–1909.

SURYANARAYANA, C. (1998). *X-Ray Diffraction: A Practical Approach*. New York, NY: Springer.

SWADENER, J. G., E. P. GEORGE, and G. M. PHARR (2002). “The correlation of the indentation size effect measured with indenters of various shapes”. In: *Journal of the Mechanics and Physics of Solids* 50, pp. 681–694.

TARIGOPULA, V., O. S. HOPPERSTAD, M. LANGSETH, and A. H. CLAUSEN (2008). “Elastic-plastic behaviour of dual-phase, high-strength steel under strain-path changes”. In: *European Journal of Mechanics - A/Solids* 27, pp. 764–782.

TARIGOPULA, V., O. S. HOPPERSTAD, M. LANGSETH, and A. H. CLAUSEN (2009). "An evaluation of a combined isotropic-kinematic hardening model for representation of complex strain-path changes in dual-phase steel". In: *European Journal of Mechanics - A/Solids* 28, pp. 792–805.

TASAN, C. C., J. P. M. HOEFNAGELS, C. H. L. J. ten HORN, and M. G. D. GEERS (2009). "Experimental analysis of strain path dependent ductile damage mechanics and forming limits". In: *Mechanics of Materials* 41, pp. 1264–1276.

TATA STEEL EUROPE LIMITED (2016). *Cold-rolled DP600-UC*. URL: https://www.tatasteeleurope.com/automotive/products/metallic-coated/ahss-uhss (visited on 03/16/2023).

TEKKAYA, A. E., J. M. ALLWOOD, P. F. BARIANI, S. BRUSCHI, J. CAO, S. GRAMLICH, P. GROCHE, G. HIRT, T. ISHIKAWA, C. LÖBBE, J. LUEG-ALTHOFF, M. MERKLEIN, W. Z. MISIOLEK, M. PIETRZYK, R. SHIVPURI, and J. YANAGIMOTO (2015). "Metal forming beyond shaping: Predicting and setting product properties". In: *CIRP Annals* 64, pp. 629–653.

TEKOĞLU, C., J. W. HUTCHINSON, and T. PARDOEN (2015). "On localization and void coalescence as a precursor to ductile fracture". In: *Philosophical Transactions of the Royal Society A: Mathematical, Physical and Engineering Sciences* 373.

TEODOSIU, C. and Z. HU (1998). "Microstructure in the continuum modeling of plastic anisotropy". In: *Proceedings of 19th Risø International Symposium on Materials Science: Modelling of Structure and Mechanics of Materials from Microscale to products.*, pp. 149–168.

THYSSENKRUPP STEEL EUROPE AG (2022). *MHZ - Produktinformation für mikrolegierte Stähle*. URL: https://www.thyssenkrupp-steel.com/media/content_1/publikationen/produktinformationen/mhz/thyssenkrupp_mhz_produktinformation_steel_de.pdf (visited on 03/16/2023).

TOMOTA, Y., P. LUKAS, S. HARJO, J.-H. PARK, N. TSUCHIDA, and D. NEOV (2003). "In situ neutron diffraction study of IF and ultra low carbon steels upon tensile deformation". In: *Acta Materialia* 51, pp. 819–830.

TORGAL-PACHECO, F., M. V. DIAMANTI, A. NAZARI, C. G. GRANQVIST, A. PRUNA, and S. AMIRKHANIAN (2019). *Nanotechnology in eco-efficient construction: Materials, processes and applications*. Duxford, United Kingdom: Woodhead Publishing an imprint of Elsevier.

TOYODA, S., Y. KAWABATA, K. SUZUKI, K. SAKATA, S. YABUMOTO, M. GUNJI, and A. SATO (2004). "Effects of Microstructure and Aging Property on Formability in ERW Steel Tubes for Automobile Structural Parts". In: *SAE Technical Paper Series*. Warrendale, USA: SAE International.

TRAPHÖNER, H. (2020). "Erweiterung der Anwendungsgrenzen des ebenen Torsionsversuchs". Dissertation. Technische Universität Dortmund.

UNGÁR, T. (2008). "Dislocation model of strain anisotropy". In: *Powder Diffraction* 23, pp. 125–132.

UNGÁR, T., S. OTT, P.G SANDERS, A. BORBÉLY, and J.R WEERTMAN (1998). "Dislocations, grain size and planar faults in nanostructured copper determined by high resolution X-ray diffraction and a new procedure of peak profile analysis". In: *Acta Materialia* 46, pp. 3693–3699.

VAN PETEGEM, S., J. WAGNER, T. PANZNER, M. V. UPADHYAY, T. T. T. TRANG, and H. VAN SWYGENHOVEN (2016). "In-situ neutron diffraction during biaxial deformation". In: *Acta Materialia* 105, pp. 404–416.

VINCZE, G., M. C. BUTUC, F. BARLAT, A. B. LOPES, and T. F. V. SILVA (2019). "Strain path changes in aluminum". In: *Proceedings of the 22nd international ESAFORM conference on material forming: ESAFORM2019*. AIP Conference Proceedings. AIP Publishing.

VITZTHUM, S. (2023). *In-situ Analysis of Eleastic-Plastic Characteristics of Steel Sheets*.

VITZTHUM, S., C. HARTMANN, M. EDER, and W. VOLK (2019). "Temperature-based determination of the onset of yielding using a new clip-on device for tensile tests". In: *Procedia Manufacturing* 29, pp. 490–497.

VITZTHUM, S., J. REBELO KORNMEIER, M. HOFMANN, M. GRUBER, E. MAAWAD, A. C. BATISTA, C. HARTMANN, and W. VOLK (2022a). "In-situ analysis of the thermoelastic effect and its relation to the onset of yielding of low carbon steel". In: *Materials & Design* 219, p. 110753.

VITZTHUM, S., J. REBELO KORNMEIER, M. HOFMANN, M. GRUBER, R. NORZ, E. MAAWAD, J. MENDIGUREN, and W. VOLK (2022b). "In-situ analysis of the elastic-plastic characteristics of high strength dual-phase steel". In: *Materials Science and Engineering: A* 857.

VOLK, W. and C. GABER (2017). "Investigation and Compensation of Biaxial Pre-strain During the Standard Nakajima- and Marciniak-test Using Generalized Forming Limit Concept". In: *Procedia Engineering* 207, pp. 568–573.

VOLK, W., P. GROCHE, A. BROSIUS, A. GHIOTTI, B. L. KINSEY, M. LIEWALD, L. MADEJ, J. MIN, and J. YANAGIMOTO (2019). "Models and modelling for process limits in metal forming". In: *CIRP Annals* 68, pp. 775–798.

VOLK, W., M. GRUBER, and R. NORZ (2020b). "Prediction of limit strains during non-proportional load paths with a change in loading direction". In: *IOP Conference Series: Materials Science and Engineering* 967, p. 012069.

VOLK, W., H. HOFFMANN, J. SUH, and J. KIM (2012). "Failure prediction for nonlinear strain paths in sheet metal forming". In: *CIRP Annals* 61, pp. 259–262.

VOLK, W. and P. HORA (2011). "New algorithm for a robust user-independent evaluation of beginning instability for the experimental FLC determination". In: *International Journal of Material Forming* 4, pp. 339–346.

VOLK, W., R. NORZ, M. EDER, and H. HOFFMANN (2020a). "Influence of non-proportional load paths and change in loading direction on the failure mode of sheet metals". In: *CIRP Annals* 69, pp. 273–276.

VOLK, W. and J. SUH (2014). “Prediction of formability for non-linear deformation history using generalized forming limit concept (GFLC)”. In: *AIP Conference Proceedings*, pp. 556–561.

VRETTOU, A., H. KITAGUCHI, B. CAI, T. CONNOLLEY, and D. COLLINS (2022). “Mechanisms controlling ductility loss from abrupt Strain Path Changes in a low carbon steel”. In: *Materials Science and Engineering: A* 843.

WANG, H., P. D. WU, C. N. TOMÉ, and J. WANG (2012). “Study of lattice strains in magnesium alloy AZ31 based on a large strain elastic-viscoplastic self-consistent polycrystal model”. In: *International Journal of Solids and Structures* 49, pp. 2155–2167.

WEINSCHENK, A. and W. VOLK (2017). “FEA-based development of a new tool for systematic experimental validation of nonlinear strain paths and design of test specimens”. In: *AIP Conference Proceedings* 1896.

WEISSBACH, W., M. DAHMS, and C. JAROSCHEK (2015). *Werkstoffkunde: Strukturen, Eigenschaften, Prüfung*. Wiesbaden: Springer Vieweg.

WEJDEMANN, C., H. F. POULSEN, U. LIENERT, and W. PANTLEON (2013). “In Situ Observation of the Dislocation Structure Evolution During a Strain Path Change in Copper”. In: *JOM* 65, pp. 35–43.

WERBER, A., M. LIEWALD, W. NESTER, M. GRÜNBAUM, K. WIEGAND, J. SIMON, J. TIMM, C. BASSI, and W. HOTZ (2012). “Influence of Different Pre-Stretching Modes on the Forming Limit Diagram of AA6014”. In: *Key Engineering Materials* 504-506, pp. 71–76.

WERBER, A., M. LIEWALD, W. NESTER, M. GRÜNBAUM, K. WIEGAND, J. SIMON, J. TIMM, and W. HOTZ (2013). “Assessment of forming limit stress curves as failure criterion for non-proportional forming processes”. In: *Production Engineering* 7, pp. 213–221.

– (2014). “Development of a new failure prediction criterion in sheet metal forming”. In: *International Journal of Material Forming* 7, pp. 395–403.

WILLIAMSON, G.K. and W.H HALL (1953). “X-ray line broadening from filed aluminium and wolfram”. In: *Acta Metallurgica* 1, pp. 22–31.

WILLIAMSON, G.K. and R. E. SMALLMAN (1956). “III. Dislocation densities in some annealed and cold-worked metals from measurements on the X-ray debye-scherrer spectrum”. In: *Philosophical Magazine* 1, pp. 34–46.

WILSON, A.J.C. (1949). *X-ray Optics: The Diffraction of X-rays by Finite and Imperfect Crystals*. Methuen’s monographs on physical subjects. Methuen.

WILSON, D. and P. BATE (1994). “Influences of cell walls and grain boundaries on transient responses of an if steel to changes in strain path”. In: *Acta Metallurgica et Materialia* 42, pp. 1099–1111.

WU, M., W. FANG, R.-M. CHEN, B. JIANG, H.-B. WANG, Y.-Z. LIU, and H.-L. LIANG (2019). “Mechanical anisotropy and local ductility in transverse tensile deformation in hot rolled steels: The role of MnS inclusions”. In: *Materials Science and Engineering: A* 744, pp. 324–334.

YOSHIDA, K., T. ISHIZAKA, M. KURODA, and S. IKAWA (2007). “The effects of texture on formability of aluminum alloy sheets”. In: *Acta Materialia* 55, pp. 4499–4506.

ZHANG, H., X. LI, L. ZHAO, H. SONG, and G. HUANG (2022). “In Situ SEM Investigation of Local Deformation and Failure Behavior of Ti6Al4V under Tensile and Shear Loading”. In: *Journal of Materials Engineering and Performance* 31, pp. 4687–4696.

ZHANG, X. X., A. LUTZ, H. ANDRÄ, M. LAHRES, W. M. GAN, E. MAAWAD, and C. EMMELMANN (2021). “Evolution of microscopic strains, stresses, and dislocation density during in-situ tensile loading of additively manufactured AlSi10Mg alloy”. In: *International Journal of Plasticity* 139.

ZHUANG, Z., Z. LIU, and Y. CUI (2019). “Dislocation-Based Single-Crystal Plasticity Model”. In: *Dislocation Mechanism-Based Crystal Plasticity*. Elsevier, pp. 91–119.

ZISTL, M., S. GERKE, and M. BRÜNIG (2022). “Experiments on Damage and Failure Behavior of Biaxially Loaded Specimens under Non-Proportional Load Paths”. In: *The 19th International Conference on Experimental Mechanics*. Basel, Switzerland: MDPI.

D Appendix

D.1 Miller indices

Table D.1 shows the presented components of an *bcc* - crystal structure.

Table D.1: Miller indices of the presented components in Figure 2.10

Texture componen	Miller indices	Euler angles		
		φ_1	ϕ	φ_2
Cube	{001}<100>	0	0	0
Rotated Cube	{001}<110>	45	0	0
Goss	{011}<100>	0	45	0
Goss/Brass	{001}<115>	16	45	0
Brass	{001}<211>	35	45	0
A	{011}<111>	55	45	0
Rotated Goss	{011}<011>	90	45	0
Dillamore	{4411}<11118>	90	27	45
Copper	{112}<111>	90	35	45
Rotated Copper	{112}<011>	0	35	45
E	{111}<011>	60	55	45
Y	{111}<112>	90	55	45
S	{123}<634>	59	37	63
R	{124}<211>	53	36	60

D.2 Results - Onset of Yielding for the DP600 steel

Results of the determination of the onset of yielding for the DP600 steel and the three different applied methods.

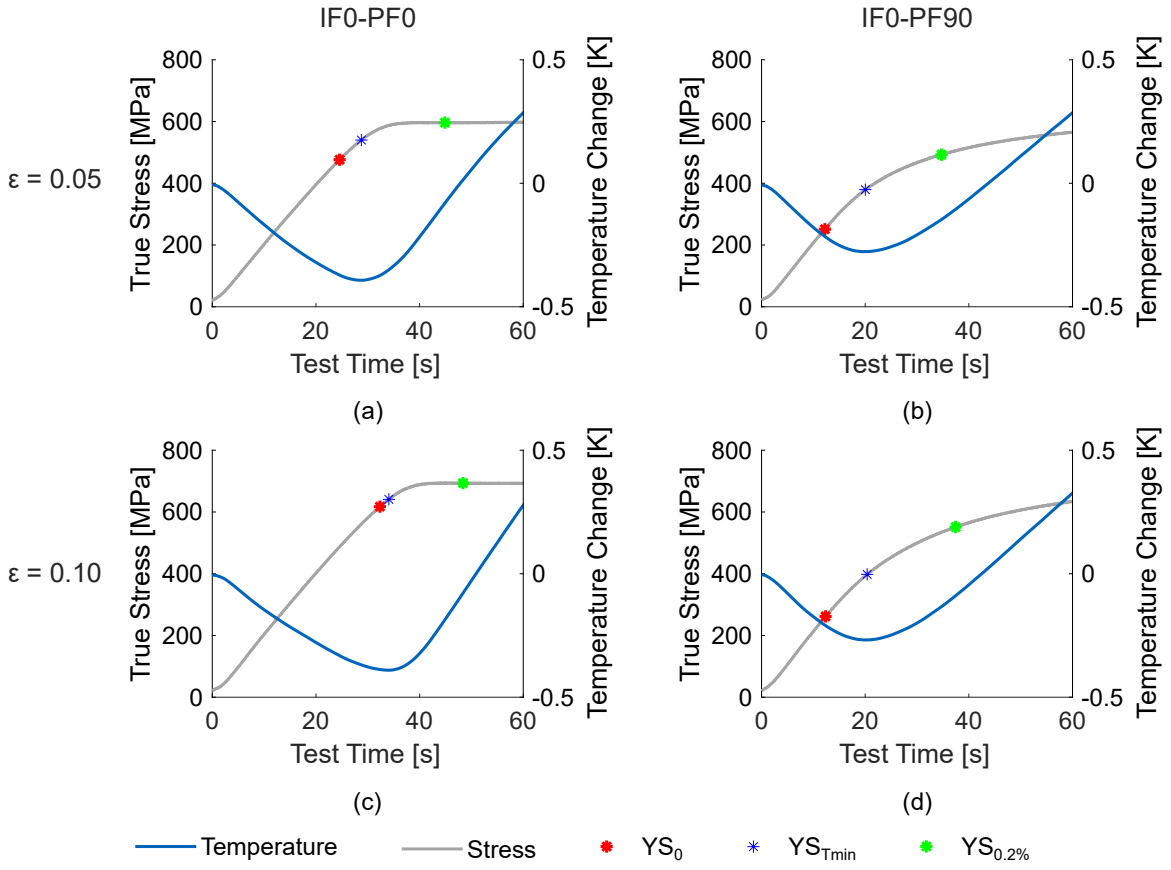

Figure D.1: Determination of the onset of yielding for the DP600 with the configurations IF0-PF0, $\varepsilon_{pre} = 0.05$ (a), IF0-PF90, $\varepsilon_{pre} = 0.05$ (b), IF0-PF0, $\varepsilon_{pre} = 0.10$ (c) and IF0-PF0, $\varepsilon_{pre} = 0.10$ (d).

D.3 Results - Lattice Strains for the DP600 steel

Results of the evaluation of the lattice strains for the DP600 steel for four individual specimen configurations.

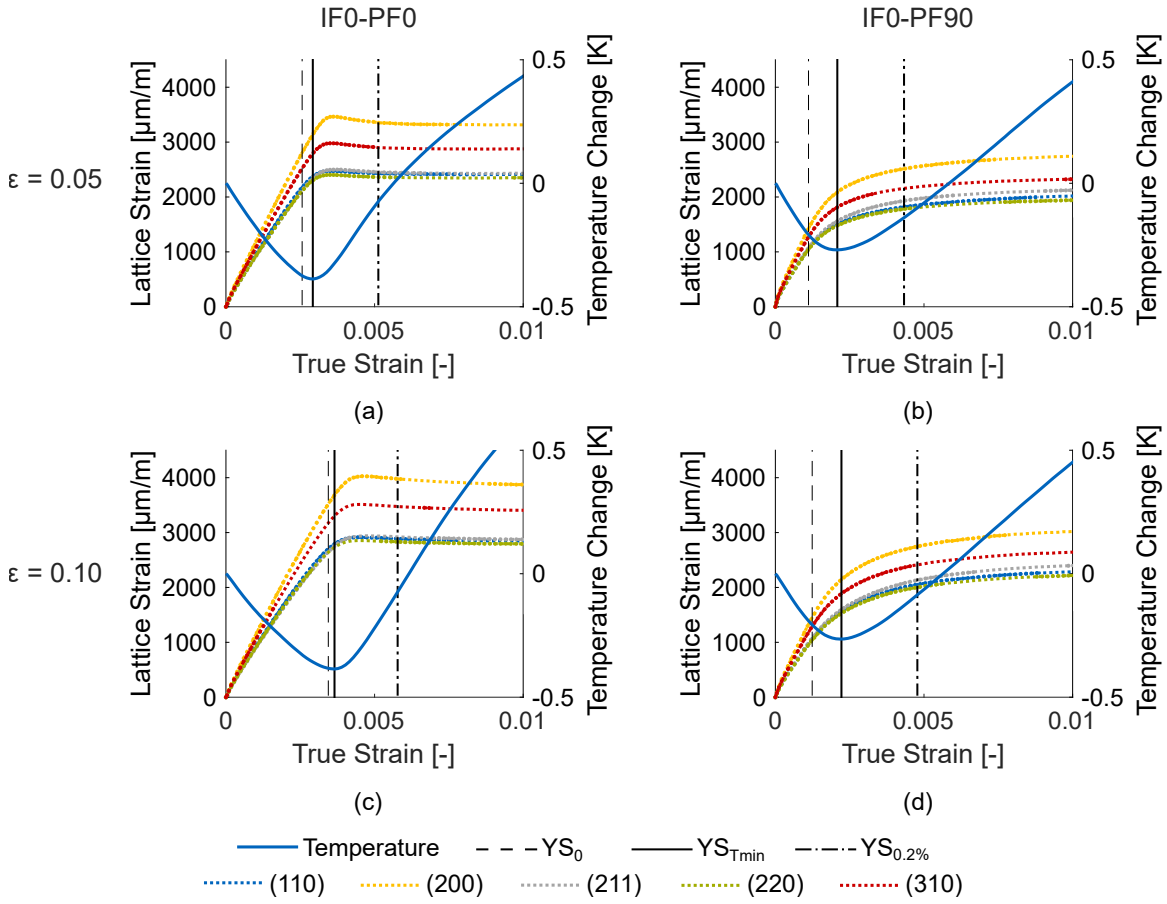

Figure D.2: Determination of the onset of yielding for the DP600 with the configurations IF0-PF0, $\varepsilon_{pre} = 0.05$ (a), IF0-PF90, $\varepsilon_{pre} = 0.05$ (b), IF0-PF0, $\varepsilon_{pre} = 0.10$ (c) and IF0-PF0, $\varepsilon_{pre} = 0.10$ (d).

D.4 Results - Dislocation Density for the DP600 steel in the Longitudinal direction

Results of the evaluation of the dislocation densities for the DP600 steel for four individual specimen configurations.

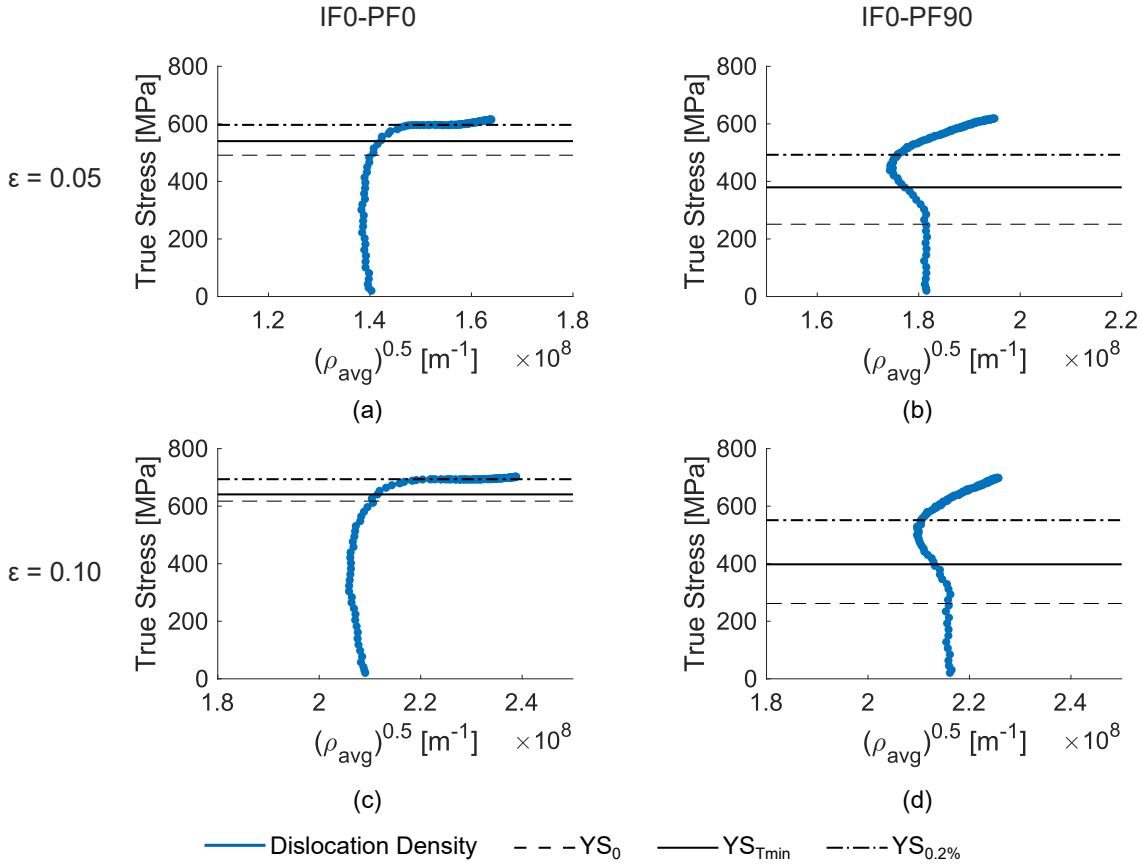

Figure D.3: Determination of the dislocation densities the DP600 with the configurations IF0-PF0, $\varepsilon_{pre} = 0.05$ (a), IF0-PF90, $\varepsilon_{pre} = 0.05$ (b), IF0-PF0, $\varepsilon_{pre} = 0.10$ (c) and IF0-PF0, $\varepsilon_{pre} = 0.10$ (d).

D.5 Results - Dislocation Density for the DP600 steel in the Transversal direction

Results of the evaluation of the dislocation densities for the DP600 steel in the transversal direction for the two specimens with a change in loading direction.

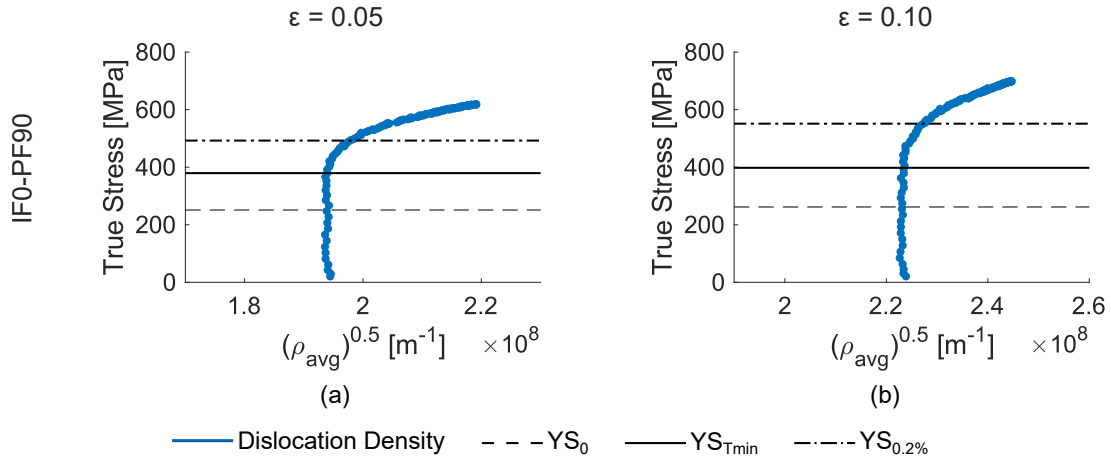

Figure D.4: Determination of the dislocation densities for the DP600 with the configurations IF0-PF90, $\varepsilon_{pre} = 0.05$ (a), IF0-PF90, $\varepsilon_{pre} = 0.10$ (b), in the transversal direction.

Dissertationen des Lehrstuhls für Umformtechnik und Gießereiwesen, Prof. Dr.-Ing. Wolfram Volk

01 *Felix Zimmermann*
Generierung von maßgeschneiderten Bauteileigenschaften in PHS-Bauteilen durch Anlassen mittels Flamme;
2014; ISBN: 978-3-95884-007-2

02 *Christopher Joseph Thoma*
Simulationsgestützte Optimierung der Maßhaltigkeit in der Prozesskette Druckguss;
2015; ISBN: 978-3-73699-009-8

03 *Joung Sik Suh*
Verbesserung der Kaltumformbarkeit von AZ31 Mg-Blech durch Equal Channel Angular Pressing (ECAP);
2015; URN: http://nbn-resolving.de/urn/resolver.pl?urn:nbn:de:bvb:91-diss-20151215-1271570-1-8

04 *Robert Ramakrishnan*
3-D-Drucken mit einem anorganischen Formstoffsystem;
2016; URN: http://nbn-resolving.de/urn/resolver.pl?urn:nbn:de:bvb:91-diss-20160129-1276474-1-5

05 *Patrick Saal*
Quantitative Phasenanalyse von ausferritischem Gusseisen mithilfe der Neutronendiffraktometrie;
2017; URN: http://nbn-resolving.de/urn/resolver.pl?urn:nbn:de:bvb:91-diss-20170125-1304161-1-8

06 *Peter Sachnik*
Methodik für gratfreie Schnittflächen beim Scherschneiden;
2017; URN: http://nbn-resolving.de/urn/resolver.pl?urn:nbn:de:bvb:91-diss-20160406-1304184-1-8

07 *Thomas Martin Kopp*
Einfluss der Werkzeugsteifigkeit auf Scherschneidprozess und Werkzeugverschleiß beim offenen Schnitt;
2017; URN: http://nbn-resolving.de/urn/resolver.pl?urn:nbn:de:bvb:91-diss-20170426-1327352-1-7

08 *Simon Josef Maier*
Inline-Qualitätsprüfung im Presswerk durch intelligente Nachfolgewerkzeuge
2018; ISBN: 978-3-95884-004-1

09 *David Jocham*
Bestimmung der lokalen Einschnürung nach linearer und nichtlinearer Umformhistorie sowie Ermittlung dehnungs- und geschwindigkeitsabhängiger Materialkennwerte;
2018; ISBN: 978-3-95884-012-6

10 *Christoph Kaiser*
Effiziente Produkt- und Prozessabsicherung für gefalzte Karosseriebauteile durch ein metamodellbasiertes Assistenzsystem;
2018; ISBN: 978-3-95884-018-8

11 *Daniel Marian Opritescu*
Risikominimale Überbrückung von Kapazitätsengpässen im Presswerksverbund der Automobilindustrie;
2018; ISBN: 978-3-95884-020-1

12 *Maria Anna Hiller*
Fügen durch Clinchen mit rotierender Werkzeugbewegung;
2019; ISBN: 978-3-95884-024-9

13 *Hannes Alois Weiss*
Fertigung effizienter Elektromotoren;
2019; ISBN: 978-3-95884-037-9

14 *Wan-Gi Cha*
Formability Consideration in Bead Optimization to stiffen Deep Drawn Parts;
2019; ISBN: 978-3-95884-036-2

15 *Sven Peter Jansen*
Methodik zur Auslegung konturnaher Temperiersysteme in Druckgusswerkzeugen;
2019; ISBN: 978-3-95884-035-5

16 *Georg Baumgartner*
Das mikromechanische Verhalten von binären Aluminium-Silizium-Legierungen unter Last;
2019; ISBN: 978-3-95884-032-4

17 *Simon Vogt*
Entwicklung eines Verfahrens zur Herstellung von verpressten Spulen für effizientere E-Traktionsantriebe;
2019; URN: http://nbn-resolving.de/urn/resolver.pl?urn:nbn:de:bvb:91-diss-20191001-1483133-1-0

18 *Patrick Thomas Helmut Woisetschläger*
Beitrag zur Optimierung der Schichtanbindung bei thermisch gespritzten Zylinderlaufflächen im Verbrennungsmotor;
2020; ISBN: 978-3-95884-042-3

19 *Michael Walter Krinninger*
Ansätze zur Reduzierung der prozessbedingten Flitterbildung beim Scherschneiden von Aluminiumblechen im offenen Schnitt;
2020; ISBN: 978-3-95884-045-4

20 *Tim Benkert*
Blechradkörper für Leichtbauzahnräder – Eine Machbarkeitsstudie zur Herstellung von tiefgezogenen und feingeschnittenen Innenteilen mehrteiliger Zahnräder;
2020; ISBN: 978-3-95884-046-1

21 *Benjamin Himmel*
Material Jetting of Aluminium – Analysis of a Novel Additive Manufacturing Process;
2020; ISBN: 978-3-95884-049-2

22 *Florian Martin Hofbauer*
Großserientaugliche Umsetzung von dünnwandigem Stahlguss für den Automobilbau;
2020; ISBN: 978-3-95884-050-8

23 *Annika Weinschenk*
Simulative und experimentelle Untersuchungen zur Detektion und Prävention von Einfallstellen in Außenhautbauteilen;
2020; ISBN: 978-3-95884-052-2

24 *Florian Heilmeier*
Ermittlung schwindungsbedingter Gussteilspannungen mit Hilfe eingegossener, faseroptischer Dehnungssensoren;
2020; ISBN: 978-3-95884-053-9

25 *Ferdinand Neumayer*
Ermittlung und Auswirkung der Durchbruchkraft beim Scherschneiden;
2020; URN: http://nbn-resolving.de/urn/resolver.pl?urn:nbn:de:bvb:91-diss-20200729-1530885-1-5

26 *Manuel Pintore*
Gießtechnische Herstellung und technologische Charakterisierung von Kupfer-Aluminium Schichtverbunden;
2021; ISBN: 978-3-95884-059-1

27 *Tim Mittler*
Verbundstranggießen von Kupferwerkstoffen;
2021; ISBN: 978-3-95884-058-4

28 *Christoph Hartmann*
Spatio-Temporal Optical Flow Methods for Process Analysis – Robust Strain, Strain Rate, and Crack Propagation Measurement in Shear Cutting;
2021; ISBN: 978-3-95884-066-9

29 *Marco Raupach*
Simulationsbasierte Konstruktionsmethodik zur Herstellung markanter Bauteilradien im Karosseriebau;
2021; ISBN: 978-3-95884-068-3

30 *Fabian Zgoll*
Methodik zur maschinenoptimalen Werkzeugeinarbeitung durch virtuelle Kompensation der Werkzeug- und Pressendurchbiegung;
2021; ISBN: 978-3-95884-067-6

31 *Phillipp Johnathan Lechner*
A Material Model for Foundry Cores – The Brittle Fracture Behaviour of Chemically-Bound Foundry Sands;
2021; ISBN: 978-3-95884-073-7

32 *Martin Feistle*
Edge-Fracture-Tensile-Test – Neues Kantenrissprüfverfahren für duktile metallische Werkstoffe;
2021; ISBN: 978-3-95884-079-9

33 *Thomas Greß*
Vertical Continuous Compound Casting of Copper Aluminium Semi-Finished Products – Design of a Resource-Efficient Production Technology for the Formation of Metallurgically Bonded Bilayer Parts;
2021; URN: http://nbn-resolving.de/urn/resolver.pl?urn:nbn:de:bvb:91-diss-20210721-1579499-1-7

34 *Jens-Michael Stahl*
Residual stresses induced by shear cutting – Targeted use for manufacturing functional surfaces with an improved fatigue behavior;
2021; URN: http://nbn-resolving.de/urn/resolver.pl?urn:nbn:de:bvb:91-diss-20210802-1593943-1-2

35 *Florian Ettemeyer*
Charakterisierung des Entkernverhaltens anorganisch gebundener Sand-Binder-Systeme;
2021; URN: http://nbn-resolving.de/urn/resolver.pl?urn:nbn:de:bvb:91-diss-20211011-1601398-1-3

36 *Lucas Schulte-Vorwick*
In-Line-Richten von Fahrzeugstrukturteilen aus Leichtmetalldruckguss;
2021; ISBN: 978-3-95884-075-1

37 *Martin Günther Landesberger*
Characterization and Design of Enhanced Ductile Irons;
2022; ISBN: 978-3-9820746-9-6

38 *Nikolas Viktor Beulich*
Entwicklung einer Methodik zur Auslegung und Absicherung des Freiformbiegens mit bewegter Matrize für dreidimensionale Biegegeometrien;
2022; URN: http://nbn-resolving.de/urn/resolver.pl?urn:nbn:de:bvb:91-diss-20221219-1652106-1-5

39 *Philipp Maximilian Tröber*
Adhäsionsentstehung beim Scherschneiden und Tiefziehen unter Berücksichtigung von Temperatur und thermoelektrischen Strömen;
2023; URN: http://nbn-resolving.de/urn/resolver.pl?urn:nbn:de:bvb:91-diss-20230130-1688200-1-4

40 *Matthias Eder*
Validierung von Materialmodellen – Der MUC-Test als Methodik zur Qualifizierung von Materialmodellen für Blechwerkstoffe;
2023; ISBN: 978-3-9820746-8-9

41 *Simon Josef Vitzthum*
In-situ Analysis of Elastic-Plastic Characteristics of Steel Sheets;
2023; ISBN: 978-3-9820746-7-2

42 *Patricia Erhard*
Slurry-based 3D printing of ceramic casting cores;
2023; ISBN 978-3-9820746-6-5

43 *Mario Claudio Senff*
Hybride Strukturbauteile für die Karosserie – Fügen von Aluminiumguss und Stahl durch Verbundgießen und Rührreibschweißen;
2024; ISBN 978-3-9820746-4-1

44 *Fabian Constantin Dobmeier*
Künstliche Intelligenz im Gießereiwesen – Stufenmodell und Einführungsmethode für Anwendungen in der Qualitätssicherung;
2024; ISBN 978-3-9820746-5-8

45 *Daniel Maier*
Eigenschaftsflexibles Freiformbiegen mit bewegter Matrize;
2024; ISBN 978-3-911206-00-6

46 *Christoph Hartmann*
Removing stair steps by the use of local variation of binder concentration to achieve Near Net Shape 3D printing;
2024; ISBN 978-3-911206-02-0

47 *Maximilian Gruber*
Equal-Channel Angular Pressing für industriell anwendbare Aluminiumblechwerkstoffe;
2024; ISBN 978-3-911206-01-3

48 *Roman Norz*
The Loading Direction and ist Effects on the Material Behaviour of Sheet Metals;
2024; ISBN 978-3-911206-03-7